Alternating-gradient focusing and deceleration of large molecules

im Fachbereich Physik der
Freien Universität Berlin
eingereichte Dissertation

entstanden am
Fritz-Haber-Institut
der Max-Planck-Gesellschaft

Kirstin Wohlfart
Berlin, Mai 2008

1. Gutachter: Prof. Dr. Gerard Meijer
Fritz-Haber-Institut der Max-Planck-Gesellschaft
Freie Universität Berlin

2. Gutachter: Prof. Dr. Ludger Wöste
Freie Universität Berlin

Disputation: 30.06.2008

Zusammenfassung

Neutrale polare Moleküle können unter Ausnutzung des Stark-Effekts in zeitlich veränderlichen inhomogenen elektrischen Feldern fokussiert und abgebremst werden. Unter Verwendung des Prinzips der alternierenden Gradienten (AG) wurde ein neues Experiment zur Fokussierung und Abbremsung von großen Molekülen aus einem Molekularstrahl aufgebaut. In der neuen Apparatur konnte mit Benzonitril ein Prototyp für ein großes Molekül mittels alternierender Gradienten fokussiert und abgebremst werden. Dies gelang für Benzonitril sowohl in seinem absoluten Grundzustand, der bei ausreichend tiefen Temperaturen stabil gegenüber inelastischen Stößen ist, als auch in angeregten Rotatitionszuständen. Aufgrund der Komplexität der Stark-Mannigfaltigkeit mit einer großen Zahl von echten und vermiedenen Kreuzungen war zu Beginn der Arbeit nicht bekannt, ob auch angeregte Rotationszustände von Benzonitril abgebremst werden können. Dieses konnte jedoch im Rahmen dieser Doktorarbeit gezeigt werden. Des Weiteren sind OH Radikale unter Verwendung desselben experimentellen Aufbaus sowohl in tieffeldsuchenden als auch in hochfeldsuchenden Zuständen fokussiert und abgebremst worden. Für die Abbremsung von Molekülen in tieffeldsuchenden Zuständen mit Hilfe von alternierenden Gradienten wurde ein neues Hochspannungs-Schaltschema verwendet, um die Phasenstabilität der abgebremsten Pakete zu gewährleisten. Darüber hinaus wurde die Kopplung der transversalen und longitudinalen Bewegung in dem verwendeten AG-Abbremser untersucht. Alle Fokussier- und Abbremsmessungen stimmen gut mit den Ergebnissen von Simulationen überein. Die durchgeführten Experimente demonstrieren, dass die Fokussierung und Abbremsung neutraler Moleküle mittels alternierender Gradienten eine allgemein anwendbare Methode ist: Sie erlaubt, polare Moleküle in sowohl tieffeldsuchenden wie auch hochfeldsuchenden Quantenzuständen als auch im Grundzustand und in angeregten Rotationszuständen abzubremsen. Weiterhin zeigt diese Doktorarbeit, dass die leistungsstarke Methode der Abbremsung mit Hilfe von zeitlich veränderlichen inhomogenen elektrischen Feldern auf große mehratomige Moleküle und in Zukunft sogar auf Biomoleküle angewendet werden kann.

Abstract

Exploiting the Stark effect, neutral polar molecules can be focused and decelerated in an array of time-varying inhomogeneous electric fields in alternating-gradient configuration. Using this principle, a new experiment for the focusing and deceleration of large molecules from a molecular beam has been set up. With the new setup, the alternating-gradient focusing and deceleration of benzonitrile, a prototypical large molecule, have been demonstrated. Benzonitrile has been decelerated in its absolute ground state, which is not susceptible to inelastic collisions at sufficiently low temperatures, as well as in rotationally excited states. Because of the complexity of the Stark manifold with a large number of real and avoided crossings, it was not *a priori* clear whether benzonitrile in excited rotational states could be decelerated. However, this has been successfully demonstrated in this thesis. Furthermore, using the same alternating-gradient setup, OH radicals in both low-field-seeking and high-field-seeking quantum states have been focused and decelerated. For the deceleration of molecules in a low-field-seeking quantum state using an alternating-gradient decelerator, a new high voltage switching scheme has to be applied in order to achieve phase stability for the decelerated packets. In addition, the coupling of transverse and longitudinal motion in the alternating-gradient decelerator has been studied. All focusing and deceleration measurements agree well with the outcome of trajectory simulations. The experiments performed in this thesis demonstrate that alternating-gradient focusing and deceleration is a general method: it allows to decelerate polar molecules in both low-field-seeking and high-field-seeking quantum states as well as in ground and rotationally excited states. Furthermore, it shows that large polyatomic molecules, eventually biomolecules, are amenable to the powerful method of Stark deceleration using time-varying inhomogeneous electric fields.

Contents

Abbreviations and constants

abbreviation	name
AC	alternating current
AG	alternating gradient
BBO	beta barium borate
CAESAR	coaxially aligned electrodes for Stark effect applied in resonators
COBRA	coaxially oriented beam-resonator arrangement
Elab	electronic laboratory
FHI	Fritz Haber Institute
FPI	Fabry-Pérot interferometer
FTMW	Fourier-transform microwave
FWHM	full width at half maximum
HeNe	helium neon
hfs	high-field seeking
HV	high voltage
lfs	low-field seeking
LIF	laser-induced fluorescence
LINAC	linear particle accelerator
PMT	photomultiplier tube
TOF	time of flight
UV	ultraviolet

unit	value	
Debye	1 D	$= 3.33564095 \cdot 10^{-30}$ Cm
wave number	1 cm^{-1}	$= 1.986448 \cdot 10^{-23}$ J
	1 cm^{-1}	$= 2.99792458 \cdot 10^{10}$ Hz
unified atomic mass unit	1 u	$= 1.660538782 \cdot 10^{-27}$ kg
Ångström	1 Å	$= 1 \cdot 10^{-10}$ m

List of Figures

List of Tables

Chapter 1

Introduction

1.1 Motivation

Scientists are innately curious to study nature in ever more detail in order to better understand its underlying fundamental properties and processes. Such investigations require the continuous development and optimization of dedicated experimental techniques. The advances in experimental methods over the past decade have enabled research on cold molecules [1–3]. Cold molecules are advantageous for many different applications, for instance, they can be employed for metrology and fundamental physics studies. Measurements of the electric dipole moment (EDM) test the standard model and theories beyond [4]. Using the polar molecules PbO [5, 6] and YbF [7] an increased sensitivity for measurements on the electric dipole moment compared to the measurements using atoms [8] is predicted. For this purpose, first experiments to produce slow, cold beams of YbF have been performed [9]. Cold OH radicals can be used to study the time variation of the fine structure constant α in laboratory experiments [10]. In addition, there are many prospects for cold chemistry [3], and most recently, the imaging of a chemical reaction under well defined conditions has been shown [11].

In this thesis, the alternating-gradient (AG) focusing [12] and deceleration [13] technique (see section 1.3) – a method thus far only applied for the production of cold small molecules – is extended to large molecules, and eventually biomolecules. Over the last decades, research on biomolecules in the gas phase has made tremendous progress, and details of the structural and dynamical properties of biomolecules have been unravelled [14–16]. Decelerating the molecules allows for increased observation times and, in principle, a higher spectral resolution [17]. In particular, this would enable novel studies on the "molecular building blocks of life". In a molecular beam, biomolecules occur in multiple

conformational structures [18–20]. For tryptophan, for example, six conformers have been observed with calculated dipole moments ranging from 1 D to 8 D [19–22]. The state selection intrinsic to the AG decelerator naturally provides packets of slow, selected conformers [1]. These state- and conformer-selected packets of molecules can be aligned or oriented, which would be highly beneficial for, for instance, electron or X-ray diffraction imaging studies [24, 25], where disentangling the overlaying contributions from different species is an onerous task. The tunable velocity and the narrow velocity distribution of the AG-decelerated beams is also of great advantage for matter wave interferometry experiments [26]. Fundamental physics studies would also benefit from improved sources for cold large molecules. This would have a possible application in the search for parity violation in chiral molecules [27, 28], where the most sensitive measurements so far have been performed on the hyperfine components of vibration-rotation transitions of CHFClBr [29].

1.2 Production of cold molecules

Owing to the increased spectral complexity of molecules compared to atoms, a closed cooling cycle does not exist for molecules, and thus the laser cooling methods, as used for the production of cold atoms [30–32], cannot be applied to molecules [33]. Generally, there are two groups of methods for the production of cold molecules: either by association of ultracold atoms, or by direct cooling of the pre-existing molecules. The first method is only suitable for small molecules built from atoms which can be cooled to ultracold temperatures, and the produced molecules are, at least initially, in highly excited, weakly bound states. The second method, direct cooling of molecules, can cool molecules in strongly bound states, including their absolute ground states. In addition, the direct cooling method is much more general, as it is applicable to practically all molecular species for which a stable molecular beam can be generated.

Bose-Einstein condensation of atoms has been observed, for the first time in 1995 [34, 35]. Eight years later, three groups managed to produce molecular Bose-Einstein condenstates of ^{40}K dimers [36] or of ^{6}Li dimers [37, 38]. They achieved this feat using Feshbach resonances, scattering resonances where the atoms are transferred from an atomic state to a weakly bound highly vibrationally excited molecular state in an external magnetic field [39]. Two atoms can be associated to a molecule in a vibrationally excited state by resonant absorption of a photon (photoassociation) [40], and, using another laser, the

[1] Recently, the *cis* and *trans* conformers of 3-aminophenol have been separated in a quadrupole selector using AG focusing [23].

molecules can be transferred from this highly excited state to a bound molecular state. With this technique, homonuclear [41, 42] and heteronuclear ultracold molecules [43–46] have been produced. Recently, it has been shown that RbCs molecules can be transferred from a vibrationally excited state to the vibrational ground state using a stimulated transfer process [47]. It was proposed that a more efficient way of producing stably bound molecules will be achieved using shaped laser pulses [48]. To date, the ionization process of cold rubidium dimers has been optimized using shaped laser pulses [49].

Instead of the association of ultracold atoms, molecules can be directly cooled, for instance, using a helium buffer gas. Paramagnetic species could then be confined in a magnetic trap in anti-Helmholtz configuration. This was first demonstrated for the trapping of europium atoms [50] and extended to the paramagnetic molecules CaH, NH, ND, CrH, and MnH [51–53]. Typically, with temperatures of a few hundred mK and a trap lifetime of a few hundred ms, molecular densities of about $10^8/\mathrm{cm}^3$ have been achieved.

For many direct cooling methods, molecular beams are employed. However, in molecular beams, the molecules are moving fast with respect to the laboratory frame. Therefore, different techniques have been developed to reduce their velocity. For instance, the slowest molecules from thermal molecular beams can be filtered using a bent quadrupole guide. This velocity filtering has been employed for H_2CO [54] and D_2O molecules [55] in low-field-seeking states, as well as ND_3 molecules in both low-field-seeking and high-field-seeking states [56]. Similarly, thermal beams can be slowed down by gravity in a vertical fountain configuration, which has been demonstrated for perfluoroalkylated carbon spheres with masses of up to 6000 u [57]. However, these samples are internally hot and the population is distributed over a large number of quantum states and over different conformers.

An advantage of using supersonic jets instead of thermal beams is that the molecules are internally cooled to rotational and translational temperatures on the order of 1 K due to the adiabatic cooling in the expansion region [58]. However, they also move fast in the laboratory frame with velocities between 300 m/s and 2000 m/s, depending on the seed gas. There are different approaches for bringing molecules from a supersonic jet to rest in the laboratory frame: molecules can be slowed and cooled by billiard-like collisions [59], using counter-rotating nozzles, by which slow molecular beams of O_2, C_3HF, and SF_6 have been achieved [60, 61], or, alternatively, exploiting electric or magnetic fields.

Pioneering experiments, where not the longitudinal but the transverse motion of an atomic beam was manipulated by application of external magnetic fields, were already performed in 1922: In the Stern-Gerlach experiment, the direction quantization was demonstrated by deflecting a beam of silver atoms with an inhomogeneous magnetic field [62]. In 1926, similar experiments were performed using molecules in inhomogeneous electric fields [63]. About twenty-five years later, atomic beams were focused onto a detector by exploiting the Zeeman effect in magnetic [64, 65] or the Stark effect in electric fields [66]. A quadrupole focuser with a static electric field was used to focus ammonia molecules in the upper state of the inversion doublet, which is low-field seeking in an electric field, while defocusing the molecules in the lower component, which is high-field seeking [67]. In this way, the inverted population needed for the demonstration of the maser [68], could be produced.

While previously only the transverse motion of atomic and molecular beams had been manipulated, in 1999 the successful deceleration of a beam of metastable CO molecules using an array of time-varying inhomogeneous electric fields was demonstrated [69]. Since the Stark effect of the molecules in the electric field is exploited for the slowing of molecules, the new device was called "Stark decelerator". Molecules in low-field-seeking states are confined to a minimum of an electric field, which can readily be created on the molecular beam axis. A molecule in a low-field-seeking state gains potential energy and therefore loses kinetic energy when entering a region of high electric field. Once this molecule in its low-field-seeking state leaves the field, it gains its kinetic energy back, and thus its velocity stays constant. But, if the electric field is switched off rapidly while the molecule is in the electrode stage, it cannot gain back the kinetic energy and is therefore decelerated. This process is phase stable [70, 71]; typically about 100 electrode stages are used in order to decelerate molecules to a standstill. In the past decade, tremendous advances have been made in the Stark deceleration of small, polar molecules in low-field-seeking states. Different isotopologues of ammonia [71, 72], OH radicals [73, 74], metastable NH radicals [75], H_2CO [76], and SO_2 [77] have been decelerated. Furthermore, decelerated ND_3 has been trapped in electrostatic [72] and alternating-current electric traps [78], and OH radicals have been trapped in electrostatic [73] and magnetoelectrostatic [79] traps. For instance, OH radicals in their low-field-seeking state have been trapped in an electrostatic trap at a temperature of about 100 mK with a density of $10^7/\mathrm{cm}^3$ [73]. ND_3 molecules in low-field-seeking states have also been confined in a hexapole ring [80, 81] and a "molecular synchrotron", where the molecular packet is focused both transversely and longitudinally ("bunched") in the ring [82]. Recently, the guiding of metastable CO molecules on a micro chip has been realized [83].

For the deceleration of atoms and molecules in Rydberg states, schemes that employ phase stability have also been proposed [84], and recently, decelerated Rydberg hydrogen atoms have been trapped using electrostatic fields [85]. Furthermore, the magnetic analog of the Stark decelerator, the Zeeman decelerator, has been used to experimentally demonstrate the deceleration of hydrogen [86, 87] and neon atoms [88], and, most recently, of oxygen molecules [89]. An optical analog of the Stark decelerator utilizes a high-intensity pulsed optical lattice [90], which has been used for the deceleration for NO [91] and benzene [92].

1.3 Production of cold large molecules

Most methods presented thus far are limited to small molecules in low-field-seeking quantum states (e. g. Stark deceleration), or do not internally cool the molecules (e. g. velocity filtering). For large molecules with a dense manifold of rotational states all states are high-field seeking at the relevant electric field strengths. Furthermore, the ground state of any molecule, which is not susceptible to inelastic collisions at low enough temperatures, is high-field seeking. However, for molecules in high-field-seeking quantum states, normal Stark deceleration does not work. To confine such molecules, a maximum of the electric field on the molecular beam axis would be required. Since Maxwell's equations do not allow to create such a maximum using static electric fields [93, 94], dynamic focusing, also referred to as alternating-gradient focusing, has to be used. AG focusing was first proposed for charged particles in linear particle accelerators (LINAC) [95]; this is now a well established technique [96]. In 1966, the application of AG focusing to neutral molecular beams, where the forces are about eight orders of magnitude smaller than for a molecular ion, was proposed by Auerbach *et al.* [12]. In a single AG lens, the molecules experience a focusing force in one transverse direction and a defocusing force in the perpendicular direction. In an array of AG lenses that alternately focus and defocus in the transverse directions, the molecules can be dynamically focused and phase-stably transported along the molecular beam axis. In the following decade, AG focusing was experimentally demonstrated for molecules by Kakati and Lainé [97–99] as well as by Günther *et al.* [100–102], and, more recently, for metastable argon atoms [103] and caesium atoms [104]. However, attempts to manipulate the longitudinal velocity remained unsuccessful for a long time [105]. For the deceleration of molecules, the longitudinal electric field gradients at the entrance and exit of the AG lens can be exploited. In practice, for molecules in high-field-seeking states, this is done by switching the high voltage on when the molecules are already inside the AG lens, and by keeping the voltages on

when the molecules exit the lens. This was first demonstrated in 2002, when CO in its metastable $a^3\Pi$ state was decelerated from 275 m/s to 260 m/s [13] and in successive experiments on the AG focusing and deceleration of diatomic molecules in high-field-seeking states: the transverse distribution of metastable CO exiting the decelerator has been experimentally observed using an imaging system [106], and YbF in its $X^2\Sigma^+$ground state has been decelerated from 287 m/s to 277 m/s [9].

It is important to experimentally demonstrate AG focusing and deceleration also for large molecules, as this would enable the production of cold, slow samples thereof. This would vastly extend the range of species whose motion and orientation can be precisely controlled, and would allow for a variety of new experiments, as mentioned above. Once the molecules in high-field-seeking quantum states are decelerated, three-dimensional confinement would be possible. For instance, the molecules in high-field-seeking states could be confined in alternating-current electric traps, the analog of Paul traps for ions [107], where the same principles of dynamic focusing as in the AG decelerator are employed [78, 108, 109].

In this thesis, the AG focusing and deceleration of benzonitrile (C_7H_5N) molecules in their ground state and rotationally excited states have been demonstrated. Benzonitrile is prototypical for large asymmetric top molecules that exhibit rich rotational structure and a high density of states. As this is the case for every large or heavy molecule, all states are high-field-seeking at the relevant electric field strengths, such that these molecules cannot be decelerated in a normal Stark decelerator, and the concept of AG focusing has to be applied. Benzonitrile has a relatively large dipole moment of 4.5 D, resulting in a sufficiently large Stark-energy-to-mass ratio for AG deceleration. In addition, benzonitrile was suggested to be abundant in space, based on similar molecular species, such as benzene (C_6H_6), diacetylene (C_4H_2), and triacetylene (C_6H_2) [110], which already have been detected in the proto-planetary nebula CRL 618 [111]. Furthermore, in this thesis, the AG focusing and deceleration of the OH radical in both low-field-seeking and high-field-seeking quantum states using a single experimental setup is presented. The experiments on benzonitrile and OH radicals demonstrate that, in principle, any polar molecule can be decelerated using AG focusing and deceleration.

This thesis is organized as follows: in chapter 2, the molecular properties of benzonitrile and OH and their Stark effects are discussed. Chapter 3 explains the theoretical principles of AG focusing and deceleration. The experimental apparatus, which has been newly set up in the framework of this thesis, is discussed in chapter 4. Chapter 5 describes the precise measurement of the dipole moment of benzonitrile using Fourier-transform microwave spectroscopy. In chapter 6, the results on the AG focusing and deceleration of benzonitrile in different quantum states are presented. The results on the AG focusing and deceleration of OH in both low-field-seeking and high-field-seeking quantum states are discussed in chapter 7. Finally, a short summary and an outlook are given in chapter 8.

Chapter 2

Molecular properties

The Stark shifts of the molecules in electric fields are needed for the simulation of the molecular motion in an alternating-gradient decelerator. Hence, in this chapter, the calculations of the energy levels for benzonitrile and OH without and with electric fields are summarized.

The internal eigenstates of a molecule are determined from the Schrödinger equation

$$\hat{H}\Psi = W\Psi\,, \tag{2.1}$$

where $\hat{H}$ is the Hamiltonian, W the internal energy, and Ψ the wave function of the molecule. In the Born-Oppenheimer approximation, the couplings between the motion of the nuclei and the motion of the electrons of the molecule are neglected [112]. In this approximation, the molecular wave function separates into the wave function for the motion of the electrons and the wave function of the nuclei with two components: vibration and rotation. The internal energy W of a molecule is given by the sum

$$W = W_{\mathrm{el}} + W_{\mathrm{vib}} + W_{\mathrm{rot}}\,, \tag{2.2}$$

where W_{el} is the electronic energy, W_{vib} the vibrational energy, and W_{rot} the rotational energy of the molecule.

2.1 Molecular properties of benzonitrile

2.1.1 The rigid asymmetric rotor

Benzonitrile (C_7H_5N) is an asymmetric top molecule, characterized by three non-equal and non-zero principal moments of inertia I_a, I_b, and I_c. Because benzonitrile is studied in a supersonic jet at low temperatures, practically the

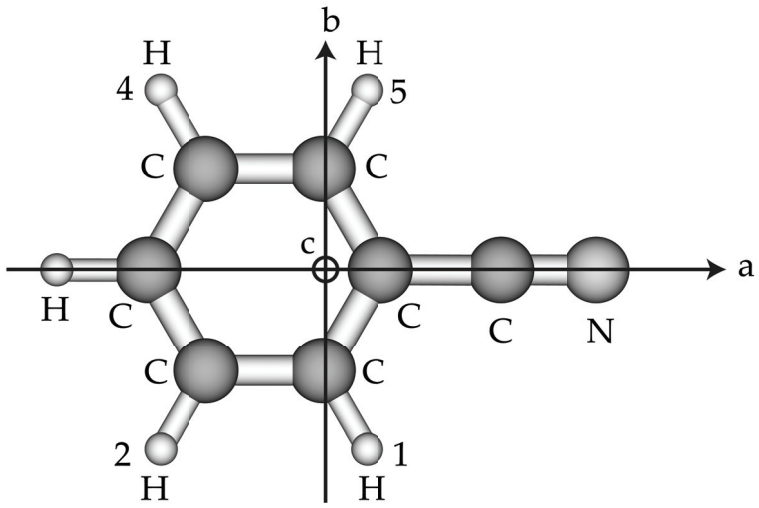

Figure 2.1: Sketch of the molecular structure of benzonitrile (C_7H_5N) and the principal axes of inertia a, b, and c.

whole population is in its electronic and vibronic ground state, but many different rotational states are occupied. Therefore, in this section, the rotational properties of rigid asymmetric tops are detailed [113, 114].

The molecular structure and the principal axes of inertia of benzonitrile are illustrated in figure 2.1. The principal axes are conventionally labelled such that for the corresponding moments of inertia it is $I_a < I_b < I_c$. The rotational Hamiltonian of a rigid asymmetric rotor is [113]

$$\hat{H}_{rot} = A\frac{\hat{J}_a^2}{\hbar^2} + B\frac{\hat{J}_b^2}{\hbar^2} + C\frac{\hat{J}_c^2}{\hbar^2}\,, \tag{2.3}$$

where $\hat{J}_a$, $\hat{J}_b$, and $\hat{J}_c$ are the quantum mechanical operators of the components of the angular momentum about the principal axes. The rotational constants A, B, and C are defined in terms of the moments of inertia as

$$A = h^2/(8\pi^2 I_a) \tag{2.4}$$
$$B = h^2/(8\pi^2 I_b) \tag{2.5}$$
$$C = h^2/(8\pi^2 I_c)\,. \tag{2.6}$$

The rotational constants of benzonitrile are $A = 5655$ MHz, $B = 1547$ MHz, and $C = 1214$ MHz [115] (see chapter 5.3). The asymmetry of a molecule can be characterized by Ray's asymmetry parameter κ [113]

$$\kappa = \frac{2B - A - C}{A - C}\,, \tag{2.7}$$

symmetry	E	C_2^a	C_2^b	C_2^c
A	1	1	1	1
B_a	1	1	-1	-1
B_b	1	-1	1	-1
B_c	1	-1	-1	1

Table 2.1: Character table of the Four-group [113].

where $\kappa = -1$ for a prolate ($I_b = I_c$) and $\kappa = +1$ for an oblate ($I_b = I_a$) symmetric top; for benzonitrile $\kappa = -0.85$. J is the quantum number for the total angular momentum, M the projection of the angular momentum on a space-fixed quantization axis (here the z-axis), and K the projection of the angular momentum on the figure axis of the symmetric rotor. The quantum number K_a describes the projection in the limit of a prolate symmetric top and K_c for an oblate symmetric top, respectively. For an asymmetric rotor, every J-level is $(2J+1)$-fold degenerate in K and $(2J+1)$-fold degenerate in M.

The eigenvalues of asymmetric rotor molecules can be calculated as follows. The Hamiltonian H_{rot} for the asymmetric rotor is set up in the basis of symmetric top wave functions $|JKM\rangle$. Then the Hamiltonian is numerically diagonalized and the eigenvalues and eigenfunctions are determined. The symmetric top wave functions are [116]

$$|JKM\rangle = \left(\frac{2J+1}{8\pi^2}\right)^{1/2} \mathcal{D}^{J*}_{K,M}(\phi,\theta,\chi)\,, \tag{2.8}$$

where $\mathcal{D}^{J*}_{\Omega,M}(\phi,\theta,\chi)$ are Wigner rotation matrices, which describe the molecular rotation in the laboratory frame in terms of the Euler angles ϕ, θ, and χ [113]. There are six different possibilities to assign the principal axes of inertia a, b, and c with the Cartesian body-fixed axes x, y, and z. In this work, the representation I^l is used, where x corresponds to c, y corresponds to b, and z corresponds to a [113], as it is one of the most suitable representations for benzonitrile. The Hamiltonian belongs to the symmetry group V, the Four-group, which is isomorphous to the group D_2. The ellipsoid of inertia is symmetric with respect to the identity operation E and with respect to rotations of 180° about any of the principal axis of inertia [113]. The character table for the Four-group is given in table 2.1.

K_aK_c	character
ee	A
eo	B_a
oo	B_b
oe	B_c

Table 2.2: Symmetry of the wave function, which depends only on K_a and K_c for the asymmetric rotor; *e*: even, *o*: odd [113].

In the symmetric top basis, the non-zero matrix elements of $\hat{H}_{\mathrm{rot}}$ are [113]

$$\langle JKM|\hat{H}_{\mathrm{rot}}|JKM\rangle = \frac{B+C}{2}\left(J(J+1)-K^2\right)+AK^2 \tag{2.9}$$

$$\langle JKM|\hat{H}_{\mathrm{rot}}|JK\pm 2M\rangle = \frac{C-B}{4}\sqrt{J(J+1)-(K\pm 1)(K\pm 2)} \times \sqrt{J(J+1)-K(K\pm 1)}\,. \tag{2.10}$$

The matrix is block diagonal in J and M. Symmetrized wave functions can be constructed as a linear combination of the wave functions by applying the Wang transformation [117]. This yields a factorization of the matrix for any value of J and M into four submatrices according to the four symmetry species of the Four-group. These submatrices are diagonalized independently, and the resulting states are labelled as $J_{K_aK_c}$. The symmetry of the wave function of the rigid asymmetric rotor depends only on the evenness or oddness of K_a and K_c and is directly determined from the representations of the Four-group A, B_a, B_b, and B_c, as given in table 2.2.

2.1.2 Selection rules and nuclear spin statistics

The ΔJ selection rules for electric dipole transitions of an asymmetric rotor are [113]

$$\Delta J = 0, \pm 1\,. \tag{2.11}$$

The $\Delta J = -1$ transitions are designated as P-branch, $\Delta J = 0$ as Q-branch, and $\Delta J = 1$ as R-branch. The dipole moment of benzonitrile is $\mu = \mu_a = 4.515$ D [115] and $\mu_b = \mu_c = 0$. Transitions with the transition dipole moment parallel to the a inertial axis are referred to as a-type transitions. The $\Delta K_a, \Delta K_c$ selection rules are given in table 2.3 [113].

For the calculation of the population, the nuclear spin statistical weights have to be considered. Benzonitrile has C_{2v} symmetry and two pairs of identical

dipole component	permitted transitions	ΔK_a	ΔK_c
$\mu_a \neq 0$	$ee \leftrightarrow eo$, $oe \leftrightarrow oo$	$\Delta K_a = 0, \pm 2, \ldots$	$\Delta K_c = \pm 1, \pm 3, \ldots$
$\mu_b \neq 0$	$ee \leftrightarrow oo$, $oe \leftrightarrow eo$	$\Delta K_a = \pm 1, \pm 3, \ldots$	$\Delta K_c = \pm 1, \pm 3, \ldots$
$\mu_c \neq 0$	$ee \leftrightarrow eo$, $eo \leftrightarrow oo$	$\Delta K_a = \pm 1, \pm 3, \ldots$	$\Delta K_c = 0 \pm 2, \ldots$

Table 2.3: Selection rules for the asymmetric rotor for different transition dipole components [113].

$K_a K_c$	weight
ee	5
eo	5
oe	3
oo	3

Table 2.4: Nuclear spin statistical weights for benzonitrile.

protons. Using the numbering shown in figure 2.1, the protons with number 1 and 2 are identical to the protons with number 5 and 4, respectively. Because protons have the nuclear spin $I = 1/2$, they are fermions and the total wave function must be antisymmetric with respect to the exchange of two identical protons. Whether the rotational wave function is symmetric or antisymmetric, depends only on the evenness and oddness of K_a and K_c. Therefore, to obtain the asymmetry of the total wave function, the wave functions with different evenness and oddness in K_a and K_c contribute to the population with a different weight [118]. In this way, the nuclear spin statistical weights for benzonitrile are calculated and given in table 2.4.

2.1.3 Stark effect of benzonitrile

The interaction of a molecule with a non-zero electric dipole moment with an external electric field is known as the Stark effect. The Stark effect of large asymmetric rotor molecules is due to the coupling of the closely spaced rotational states with $J = J'$, $J = J' \pm 1$, and $M = M'$ by the electric field. M is the only good quantum number in the electric field. The M components of the states which are degenerate in the field-free case will split into $(J + 1)$ sublevels in the electric field. Levels with $M \neq 0$ ($M = 0$) are two-fold degenerate (not degenerate). The Hamiltonian of an asymmetric rotor in an electric field is composed of the field-free Hamiltonian $\hat{H}_{\mathrm{rot}}$, as given by equation (2.3) and the

Stark contribution $\hat{H}_{\text{Stark}}$

$$\hat{H} = \hat{H}_{\text{rot}} + \hat{H}_{\text{Stark}} \,. \tag{2.12}$$

For an electric field $\vec{E} = E\vec{e_z}$ directed along the z axis, it is

$$\hat{H}_{\text{Stark}} = -\vec{\mu}\vec{E} = -E \sum_{g=a,b,c} \mu_g \Phi_{zg} \,. \tag{2.13}$$

Φ_{zg} are the direction cosine matrices which are tabulated [113], and connect the laboratory frame components of the electric field with the components of the dipole moment in the rotating molecular frame. The non-zero matrix elements of $\hat{H}_{\text{Stark}}$ in the basis of the eigenvectors of the prolate symmetric rotor $|JKM\rangle$ corresponding to the μ_a component of the dipole moment are [119]

$$\langle JKM|\hat{H}_{\text{Stark}}|JKM\rangle = -\frac{MK}{J(J+1)}\mu_a E \tag{2.14}$$

$$\langle J+1KM|\hat{H}_{\text{Stark}}|JKM\rangle = -\frac{\sqrt{(J+1)^2-K^2}\sqrt{(J+1)^2-M^2}}{(J+1)\sqrt{(2J+1)(2J+3)}}\mu_a E \,. \tag{2.15}$$

The energies W of different states are obtained by numerical calculation of the eigenvalues of the Hamiltonian $\hat{H}$. Our basis set includes all states up to $J = 25$. The energy calculations are performed with the home-built program package libcoldmol [120].

The energies W of all M levels of the $J_{K_aK_c} = 0_{00}$ and 4_{04} states of benzonitrile as a function of the electric field strength are presented in figure 2.2(a). Their corresponding effective dipole moments μ_{eff}, defined as

$$\mu_{\text{eff}}(E) = -\frac{\partial W}{\partial E} \,, \tag{2.16}$$

are shown in figure 2.2(b). The energies are given in units of wave numbers. In the limit of an infinitely strong electric field, the Stark effect is linear and the effective dipole moment approaches the permanent dipole moment, which is indicated by a horizontal line in the graph. The maximum electric field strength on the molecular beam axis in our experiment is 142.5 kV/cm. The rotational ground state 0_{00} has only a single M level, whereas the 4_{04} state splits into five M levels. It is clearly seen that all energies decrease with an increasing electric field strength. Therefore, the states are high-field-seeking (hfs) at the relevant electric field strength.

In figure 2.3, the energies of the lowest levels $J_{K_aK_c}M = 0_{00}M, \ldots, 4_{23}M$ for small electric fields are plotted. It can be seen that all levels which are low-field seeking (lfs) at low electric field strengths, become hfs at higher electric

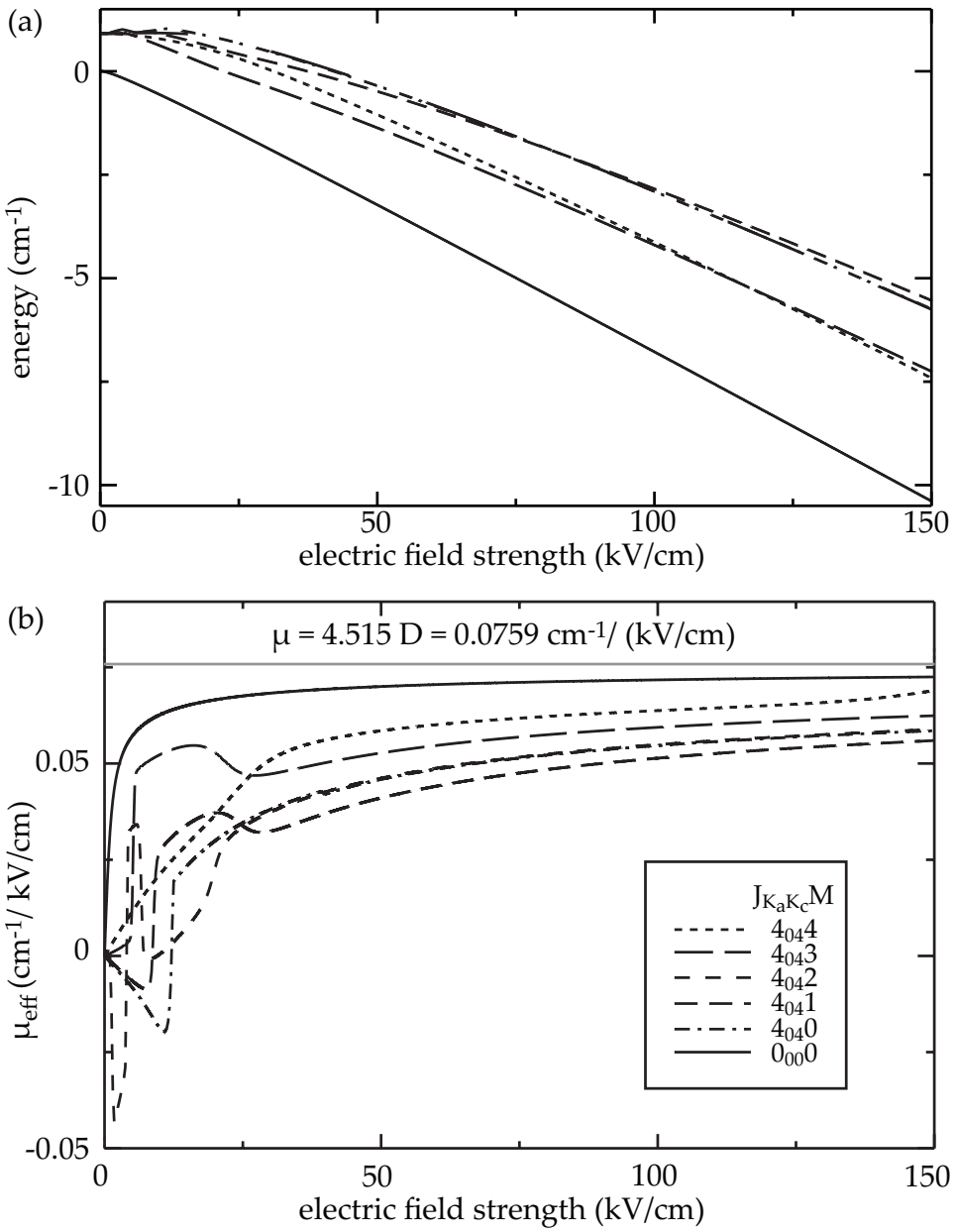

Figure 2.2: (a) Energies and (b) effective dipole moments μ_{eff} of all M levels of benzonitrile in its $J_{K_a K_c} M = 0_{00}0$ and $4_{04}M$ ($M = 0, \ldots, 4$) state as function of the electric field strength. The horizontal line in (b) indicates the value of the permanent electric dipole moment. The bends in the energy and the rapid changes of the effective dipole moment as a function of the electric field strength are due to avoided crossings.

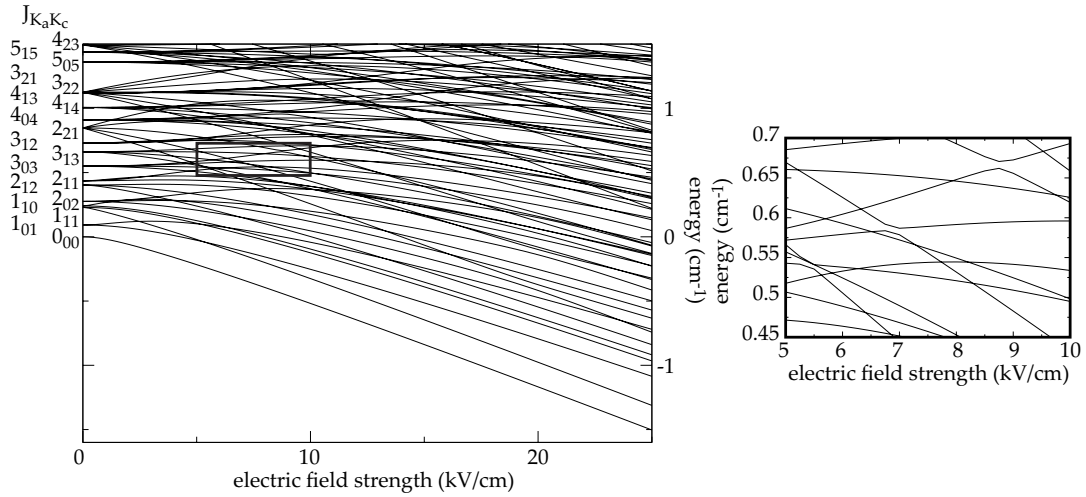

Figure 2.3: Energies of the lowest levels $J_{K_aK_c}M$ as function of the electric field strength for small electric fields. The right-hand graph shows an expanded view, where real and avoided crossings are visible.

field strengths due to the high density of states. For instance, the lowest energy eigenstate with lfs behavior at small electric fields, the $J_{K_aK_c}M = 1_{01}0$ level, has its turning point at 3.0 kV/cm, above which it is hfs. Furthermore, the high density of states and the different effective dipole moments of the $J_{K_aK_c}M$ levels cause real and avoided level crossings at low electric field strengths. Whether a level crossing is real or avoided, depends on the symmetries of the states which are defined by K_aK_c (see table 2.2). If two states have the same symmetry, the crossings are avoided, otherwise they are real. Avoided crossings result in bends of the Stark energy and rapid changes of the effective dipole moment as shown in figure 2.2 for the 4_{04} state.

2.2 Centrifugal distortion and hyperfine effects

So far, in the treatment of the asymmetric rotor, the nuclear framework has been regarded as rigid. This simplified model does not include centrifugal distortion and nuclear quadrupole coupling. However, for the relevant low states of benzonitrile, these contributions are small compared to the rigid rotor contributions, and can be neglected in the description of alternating-gradient deceleration (see chapter 6). If a higher precision is desired, i. e. , for the description of spectroscopic experiments, these effects need to be considered. For a rotating molecule, the centrifugal force distorts the molecule and the rotational constants depend on the moments of inertia. In order to describe this effect, the rotational Hamil-

tonian is expanded in a power series in $\hat{J}_a$, $\hat{J}_b$, and $\hat{J}_c$. The quartic centrifugal distortion effects lead to the correction terms Δ_J, Δ_{JK}, Δ_K, δ_J, and δ_K in Watson's a-reduction [121].

If the nuclei of a molecule have a nuclear spin I, a hyperfine structure will occur as a result of the interaction of the molecular fields with the quadrupole moments of the nuclei [113]. The nuclear spin of the ^{14}N atom is $I = 1$, and the resulting magnetic quadrupole moment couples with the molecular rotational angular momentum J to the quantum number F with values $J + I, J + I - 1 \ldots, |J - I|$. If the hyperfine structure is considered, the F quantum number replaces the J quantum number. Accordingly, F splits into $(F + 1)$ distinct M_F sublevels, with $M_F = 0, 1, \ldots, F$ in an electric field. Levels with $\pm M_F$ are two-fold degenerate, and $M_F = 0$ is not degenerate. The influence of the nuclear spin quadrupole interaction on the undisturbed energy levels can be described by the nuclear coupling constants χ_{aa}, χ_{bb}, and χ_{cc} [113]. The influence of the nuclear spin of the hydrogen atoms is small and can here be neglected.

2.3 Molecular properties of the OH radical

2.3.1 Field-free energy levels of OH

The OH radical is a diatomic open shell molecule, because one electron is missing to fill the outer $2p\pi$ shell completely. OH can be treated as a symmetric top. Due to the open-shell structure, OH has a non-zero total electronic orbital angular momentum $\vec{L}$ and a spin angular momentum $\vec{S}$, and the spin-orbit coupling must be included in the determination of the energy levels. The projections of $\vec{L}$ and $\vec{S}$ on the intermolecular axis are $\Lambda = 1$ and $\Sigma = 1/2$, respectively. For low rotational states, OH is described best by the Hund's case (a) coupling scheme [122]: Λ and Σ couple to the total angular momentum along the internuclear axis Ω, with $\Omega = 1/2$ or $\Omega = 3/2$. The electronic ground state $^{2S+1}\Lambda_\Omega = {}^2\Pi_\Omega$ has two spin-orbit manifolds $^2\Pi_{3/2}$ and $^2\Pi_{1/2}$.

The Hamiltonian consists of the rigid rotational Hamiltonian $\hat{H}_{\mathrm{rot}}$ and the spin-orbit coupling Hamiltonian $\hat{H}_{\mathrm{SO}}$ [116]

$$\hat{H} = \hat{H}_{\mathrm{rot}} + \hat{H}_{\mathrm{SO}} = B(\vec{J} - \vec{L} - \vec{S})^2 + A\vec{L} \cdot \vec{S}\,, \tag{2.17}$$

where B is the rotational constant and A the spin-orbit coupling constant. The rigid rotor wave functions $|J\Omega M\rangle$ (see equation (2.8) with $K = \Omega$, which is the conventional notation for diatomic molecules) are symmetrized by applying the

Wang transformation. The symmetrized wave function is [116]

$$|J\Omega M\epsilon\rangle = \frac{1}{\sqrt{2}}\left(|J\Omega M\rangle + \epsilon|J-\Omega M\rangle\right) , \tag{2.18}$$

where $\epsilon = \pm 1$. States with $\epsilon = +1$ are labelled with e and states with $\epsilon = -1$ are labelled with f, respectively. The parity p of the wave function is [116]

$$p = \epsilon(-1)^{J-S} . \tag{2.19}$$

The eigenfunctions of the Hamiltonian $\hat{H}$ are [123]

$$|^2\Pi_{3/2}\, J\, M\, \epsilon\rangle = C_1(J)\,|J\,\Omega = 1/2\, M\,\epsilon\rangle + C_2(J)\,|J\,\Omega = 3/2\, M\,\epsilon\rangle \tag{2.20}$$

$$|^2\Pi_{1/2}\, J\, M\, \epsilon\rangle = -C_2(J)\,|J\,\Omega = 1/2\, M\,\epsilon\rangle + C_1(J)\,|J\,\Omega = 3/2\, M\,\epsilon\rangle . \tag{2.21}$$

$C_1(J)$ and $C_2(J)$ are mixing coefficients given by

$$C_1(J) = \sqrt{\frac{X+Y-2}{2X}} \tag{2.22}$$

$$C_2(J) = \sqrt{\frac{X-Y+2}{2X}} \tag{2.23}$$

with

$$X = \sqrt{4(J+1/2)^2 + Y(Y-4)} \tag{2.24}$$

$$Y = \frac{A}{B} . \tag{2.25}$$

The eigenenergies W are obtained as

$$W(^2\Pi_{3/2}JM\epsilon) = B\left(\left(J+\frac{1}{2}\right)^2 - 1 - \frac{1}{2}X\right) \tag{2.26}$$

$$W(^2\Pi_{1/2}JM\epsilon) = B\left(\left(J+\frac{1}{2}\right)^2 - 1 + \frac{1}{2}X\right) . \tag{2.27}$$

Because A is negative for the vibrational ground state [124], the $^2\Pi_{3/2}$ state is lower in energy than the $^2\Pi_{1/2}$ state. In this calculation, the rotational levels with $\epsilon = +1$ and $\epsilon = -1$ are degenerate. By including the gyroscopic effect of $\vec{J}$ on $\vec{S}$ and $\vec{L}$, these states split into two components [125], which are named Λ-doublet. The components with $\epsilon = 1$ are lower in energy than the components with $\epsilon = -1$ for low values of J [126]. States with $\epsilon = -1$ and $\epsilon = +1$ are labelled with e and f, respectively. Based on equation (2.19) the parity of the $X^2\Pi_{3/2}, v = 0, J = 3/2\, e$ state is negative, while the $X^2\Pi_{3/2}, v = 0, J = 3/2\, f$ state is of positive parity.

2.3.2 Hyperfine structure of OH

In the $J = 3/2$ ground state level, a magnetic hyperfine structure in OH occurs as a result of the coupling of the spin of the hydrogen nucleus $I = 1/2$ with the overall angular momentum J. As shown in figure 2.4(b) each Λ-doublet component splits in two hyperfine levels with $F = 1$ and $F = 2$. In an electric field, the hyperfine components themselves split into distinct M_F levels. The matrix elements for the hyperfine splittings are given elsewhere [127]. In this thesis, the hyperfine splitting is observed in the measured field-free spectra (see section 7.2).

2.3.3 Stark effect of OH

Based on the symmetric rotor wave functions (see equation (2.8)), the matrix elements $\langle J\Omega M|H_{\text{Stark}}|J'\Omega'M'\rangle$ for the Stark Hamiltonian (equation (2.13)) are evaluated using Wigner $3J$ symbols [128]. The Stark Hamiltonian can be simplified for diatomic molecules as OH, because the dipole moment $\mu = 1.67$ D is directed along the internuclear axis [127]. From the selection rules for dipole coupling, it follows that only states with $\Omega = \Omega'$, $M = M'$, and $J = J'$ or $J = J' \pm 1$ couple. To first order, the energies of the two Λ-doublet components of the $^2\Pi_{3/2}$, $J = 3/2$ rotational state of OH are given by the eigenvalues of [128]

$$\begin{pmatrix} W_\Lambda & Q \\ Q & 0 \end{pmatrix}, \tag{2.28}$$

where W_Λ is the zero-field Λ-doublet splitting and the off-diagonal elements are

$$\begin{aligned} Q &= \langle {}^2\Pi_{3/2} JMf|H_{\text{Stark}}|{}^2\Pi_{3/2} JMe\rangle & (2.29)\\ &= -\mu E \frac{M\Omega_{\text{eff}}}{J(J+1)}, & (2.30) \end{aligned}$$

with

$$\Omega_{\text{eff}} = \left(\frac{1}{2}C_1(J)^2 + \frac{3}{2}C_2(J)^2\right). \tag{2.31}$$

The eigenvalues of the matrix (2.28) are

$$W_{\text{Stark}} = \frac{W_\Lambda}{2} \pm \sqrt{\left(\frac{W_\Lambda}{2}\right)^2 + Q^2}. \tag{2.32}$$

The plus sign represents the lfs upper Λ-doublet component f and the minus sign the hfs lower Λ-doublet component e. The Stark shift of the $^2\Pi_{3/2}$ state of OH as a function of the electric field strength is shown in figure 2.4(a). The Λ-doublet f component splits in two levels with $M\Omega = -9/4$ and $M\Omega = -3/4$, and the e components splits in two levels with $M\Omega = 9/4$ and $M\Omega = 3/4$.

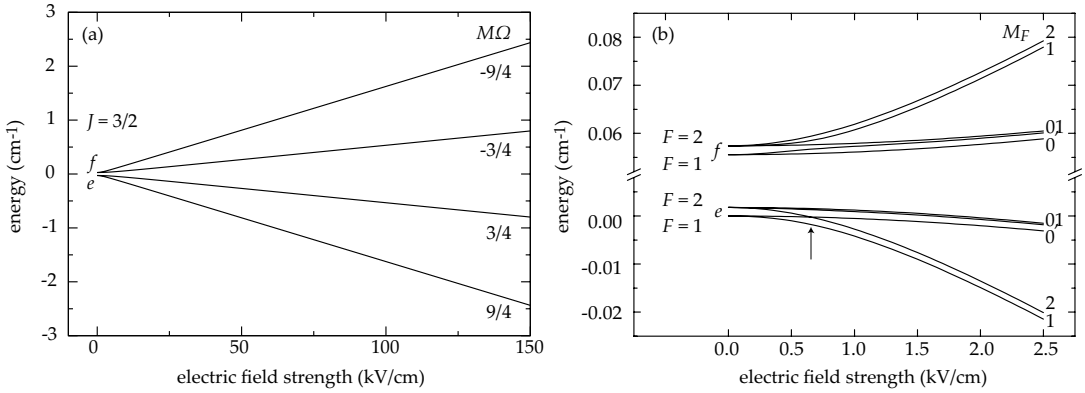

Figure 2.4: Energies of the $^2\Pi_{3/2}$ state of OH as function of the electric field strength without (a) and with (b) hyperfine structure. The real crossing of two hyperfine levels at 0.65 kV is indicated by an arrow.

2.4 Molecules suitable for alternating-gradient focusing and deceleration

The technique of alternating-gradient deceleration is in general suitable for polar molecules in lfs and hfs states. Whereas molecules in lfs states can also be decelerated using a Stark decelerator [69], which is referred to as the "normal Stark decelerator" in the remainder, molecules in hfs states can only be decelerated in an alternating-gradient decelerator. For a good deceleration ability, a large effective dipole moment-to-mass ratio is needed. Some molecular candidates with hfs states, which already have been decelerated in an alternating-gradient decelerator or are interesting candidates for future experiments, are listed together with their relevant molecular properties in table 2.5. The Stark shifts at 100 kV/cm and the effective dipole moments are obtained from Stark effect calculations for the known rotational constants and dipole moments of these molecules (see sections 2.1.3 and 2.3.3).

Metastable CO [13, 106], YbF [9], and CaF [106] have been decelerated in an alternating-gradient decelerator previously. The alternating-gradient focusing and deceleration of benzonitrile in several rotational states (chapter 6) and OH radicals in both lfs and hfs states (chaper 7) is demonstrated in this thesis. Many other molecules are interesting candidates and some of them are discussed in the following: ND_3 has already been decelerated in a lfs state in a normal Stark decelerator. Using a microwave transition, it has been pumped from the lfs state to a hfs state and then trapped in the hfs state using an alternating-current (AC) electric trap [78]. However, this technique only works for molecules

with a suitable level structure. So far, ND_3 has not been directly decelerated in its hfs state. For many biological processes, the asymmetric top molecule water plays an important role. However, for alternating-gradient focusing and deceleration experiments, water and heavy water have a relatively small effective dipole moment. Since the effective dipole moment of D_2O is about a factor two larger than the dipole moment of H_2O, D_2O should be favored for alternating-gradient experiments. So far, D_2O in lfs states has been transversely focused in a quadrupole guide [55], but has not been decelerated yet. Another possible candidate is the symmetric top molecule CH_3F which has a reasonable effective dipole moment-to-mass ratio. Because of its only 20 % smaller dipole moment compared to benzonitrile, but only half its mass, HCCCN is a promising candidate for future experiments and could be decelerated in an alternating-gradient decelerator with about 60 % of the stages, as needed for benzonitrile. Pyridazine has been aligned in a strong laser field, where an enhancement of the resonantly enhanced multiphoton intensity of 40 % has been observed [129]. It has a slightly higher effective dipole moment-to-mass ratio than benzonitrile, and a supersonic jet can be easily produced by co-expansion in a carrier gas. Hence, it is a promising candidate for deceleration experiments.

One of the aims of the work of this thesis is to explore the capability of the AG decelerator for the deceleration and trapping of biomolecules. This would allow precise studies of the intrinsic properties of these species, for example, dynamical processes on timescales ranging from femto-seconds to fractions of a second, i. e. , interconversion between conformational structures. A suitable biomolecule is the nucleic acid base guanine, which has four different tautomers with significantly different effective dipole moments. The effective dipole moment-to-mass ratio for the largest tautomer is comparable with the one of benzonitrile. In a long AG decelerator, the different tautomers could be separated from each other and the individual tautomers may be decelerated. Similarly, the different conformers of the amino acid tryptophan may be separated from each other. However, because the effective dipole moments of some conformers of tryptophan are quite similar, the separation of all conformers will be more difficult.

	molecule	rotational state	Stark shift (cm^{-1}) at 100 kV/cm	effective dipole moment (cm^{-1}/(kV/cm)) at 100 kV/cm	rotational constants (MHz) $A/B/C$	mass (u)
$*$ [13, 106]	CO ($a^3\Pi_1$) [130, 131]	$\|J=1 M\Omega=-1\rangle$	-1.25	0.0135	-/50414/-	28
$*$ [106]	CaF [132, 133]	$\|J=1/2\, M\Omega=1/4\rangle$	-3.43	0.0420	-/10268/-	59
$*$ [9]	YbF [134]	$\|J=1/2\, M\Omega=1/4\rangle$	-4.91	0.0569	-/7234/-	193
	ND_3[135, 136]	$\|J=1\, MK=-1\rangle$	-1.27	0.0134	-/154000/94650	20
$*$ [137]	OH [123, 124]	$\|J=3/2\, M\Omega=9/4\rangle$	-1.62	0.0162	-/555070/-	17
	H_2O [135, 138]	$\|J_{K_aK_c}M\rangle=\|0_{00}0\rangle$	-0.0871	0.00174	833100/434900/278500	18
	D_2O [138, 139]	$\|J_{K_aK_c}M\rangle=\|0_{00}0\rangle$	-0.159	0.00316	461470/217740/145460	20
	CH_3F [135, 140, 141]	$\|J=0\, MK=0\rangle$	-1.26	0.0193	153000/25536/-	34
	HCCCN [141, 142]	$\|J=0\, MK=0\rangle$	-4.95	0.0556	-/4549/-	51
	pyridazine (C_4H_5N) [129]	$\|J_{K_aK_c}M\rangle=\|0_{00}0\rangle$	-5.59	0.0624	6240/5970/3060	80
$*$ [143]	benzonitrile (C_7H_5N) [115]	$\|J_{K_aK_c}M\rangle=\|0_{00}0\rangle$	-6.78	0.0717	5655/1547/1214	103
	guanine					
	($C_5H_5N_5O$) [144, 145]	$\|J_{K_aK_c}M\rangle=\|0_{00}0\rangle$				151
	tautomer I		-9.62	0.101	1910/1114/704	
	tautomer II		-2.67	0.0290	1909/1119/707	
	tautomer III		-4.58	0.0489	1909/1128/710	
	tautomer IV		-6.47	0.0684	1900/1131/709	
	tryptophan					
	($C_{11}H_{12}N_2O_2$) [21]	$\|J_{K_aK_c}M\rangle=\|0_{00}0\rangle$				216
	conformer I		-6.25	0.0646	1230/402/354	
	conformer II		-4.72	0.0494	1170/423/366	
	conformer III		-1.71	0.0183	998/495/390	
	conformer IV		-11.68	0.120	971/486/378	
	conformer V		-12.28	0.126	1290/366/288	
	conformer VI		-11.37	0.116	1360/336/285	

Table 2.5: Relevant properties of molecules that are suitable for alternating-gradient focusing and deceleration. Molecules labelled with $*$ have already been decelerated in a high-field-seeking state. OH has also been decelerated in a low-field-seeking state using an alternating-gradient decelerator.

Chapter 3

Theory of alternating-gradient focusing and deceleration

3.1 Introduction

For large molecules with a dense manifold of rotational states, all states are hfs at the relevant electric field strengths, which means that their dipole moment is oriented parallel to the electric field. To confine such molecules, a maximum of the electric field on the molecular beam axis would be needed. Since such a maximum cannot be created using static electric fields, dynamic focusing, also referred to as alternating-gradient focusing, has to be used. In a single AG focusing lens, the molecules experience a focusing force in one transverse direction and a defocusing force in the perpendicular direction. In an array of AG lenses that alternately focus and defocus in the transverse directions, the

Figure 3.1: Sketch of the electrode arrangement in our alternating-gradient decelerator setup. The orientation of the electrode pairs is changed after the first electrode stage, and then after every three electrode stages.

molecules can be dynamically focused and transported along the molecular beam axis [12]. In figure 3.1 such an array of AG lenses, as it is used in our decelerator setup, is shown. For the deceleration, the longitudinal electric field gradients at the entrance and exit of the AG lenses are used. In practice, for molecules in hfs states, this is done by switching the high voltage on when the molecules are inside the AG lens, and keeping the voltages on when the molecules exit the lens. So far, only a few proof-of-principle experiments on the AG focusing and deceleration of diatomic molecules (metastable CO and YbF (see section 2.4)) in hfs states have been performed [9, 13, 106, 146]. A detailed discussion of the design criteria and motion in an AG decelerator, based on reference 106, is given in the following.

3.2 General principles

In order to keep a particle in static equilibrium in three spatial directions around the position $\vec{r} = 0$, two conditions must be fulfilled for the force field $\vec{F}(\vec{r})$: The applied force must vanish at $\vec{r} = 0$ and for small displacements the force field should tend to restore the particle towards the position $\vec{r} = 0$. Therefore, it is necessary that $\vec{\nabla} \cdot \vec{F}(\vec{r}) < 0$. The properties of the force field for molecules experiencing a linear Stark shift are summarized here and are discussed in detail by Auerbach *et al.* [12]. Using the approximation of a linear Stark shift, analytical solutions can be found and the principle of AG focusing can be understood. However, the real Stark shifts, especially for rotationally excited states of benzonitrile, are more complicated. For detailed simulations, the real Stark shifts discussed in chapter 2 are needed.

The force $\vec{F}(\vec{r})$ acting on a molecule in an inhomogeneous electric field is given by

$$\vec{F}(\vec{r}) = -\vec{\nabla} W_{\mathrm{Stark}}(E)\,, \tag{3.1}$$

where $W_{\mathrm{Stark}}(E)$ is the Stark shift of the polar molecule in an electric field of magnitude $E = |\vec{E}|$. For molecules with a linear Stark shift, it is

$$W_{\mathrm{Stark}}(E) = -\mu_{\mathrm{eff}} E\,, \tag{3.2}$$

where μ_{eff} is the effective dipole moment (see section 2.1.3). Equation (3.1) written in components is

$$F_j = \frac{\mu_{\mathrm{eff}}}{E} \sum_{i=1}^{3} \left(\frac{\partial \Phi}{\partial x_i}\right) \left(\frac{\partial^2 \Phi}{\partial x_i \partial x_j}\right)\,, \tag{3.3}$$

where Φ is the electrostatic potential. The divergence of the force for a molecule with a linear Stark shift then becomes

$$\vec{\nabla}\cdot\vec{F} = \frac{\mu_{\text{eff}}}{E^3}\times \sum_{i,j,k=1}^{3}\left[\left(\frac{\partial\Phi}{\partial x_k}\right)^2\left(\frac{\partial^2\Phi}{\partial x_i\partial x_j}\right)^2 - \left(\frac{\partial\Phi}{\partial x_i}\right)\left(\frac{\partial\Phi}{\partial x_k}\right)\left(\frac{\partial^2\Phi}{\partial x_i\partial x_j}\right)\left(\frac{\partial^2\Phi}{\partial x_k\partial x_j}\right)\right] . \quad (3.4)$$

Schwarz's inequality shows that the left-hand term of the sum is larger than or equal to the right-hand term and thus the sum is positive or zero. Therefore, the sign of $\vec{\nabla}\cdot\vec{F}$ depends solely on the sign of μ_{eff}. Molecules in lfs states have a negative μ_{eff}, which results in $\vec{\nabla}\cdot\vec{F} \leq 0$, and so focusing is readily achieved. However, molecules in hfs states have a positive μ_{eff} resulting in $\vec{\nabla}\cdot\vec{F} \geq 0$. The corresponding difficulties in the focusing of molecules in hfs states are comparable to the fact that ions with the charge q cannot be confined in a stable equilibrium by using electrostatic forces only, because for an electrostatic force field $\vec{F}$ it is $\vec{\nabla}\cdot\vec{F} = q\vec{\nabla}\vec{E} = 0$. However, for trapping $\vec{\nabla}\cdot\vec{F} < 0$ is needed. This is known as Earnshaw's theorem [147]. Analogue techniques as used for ions, for instance, in Paul traps [107] or charged particle accelerators [95, 96], can be exploited for the focusing of neutral polar molecules.

3.3 Electrode geometry

In this section, the influence of the geometry of the electrodes of an AG decelerator is discussed. An electrode geometry for which abberation effects are minimized, is important for a maximum acceptance and optimum performance of the decelerator.

3.3.1 Two-dimensional model

For simplicity, first a two-dimensional model of infinitely long electrodes is considered. This is a good approximation for the fields in the center of an AG lens of a decelerator. The effects at the ends of the electrodes which are needed to decelerate the molecules, are neglected in this two-dimensional model, but will be discussed in the next section.

For an AG lens without any abberation effects, molecules would experience a harmonic interaction potential in the transverse plane which is focusing in one direction and defocusing in the perpendicular direction. For molecules that experience a linear Stark shift (limit of high electric field strengths), the ideal electric field strength is also harmonic, that is $E(x,y) = E_0 + \eta(x^2 - y^2)$. In the

following, it is explained how an approximate harmonic field can be produced (see also references 106, 148). The electric field is the negative gradient of a scalar potential $\vec{E} = -\vec{\nabla}\Phi$, which can in two dimensions be represented as a multipole expansion in polar coordinates $r = \sqrt{x^2+y^2}$, $\theta = \tan^{-1}\left(\frac{y}{x}\right)$ as

$$\Phi(r,\theta) = \Phi_0 \left[\sum_{n=1}^{\infty} \frac{a_n}{n} \left(\frac{r}{r_0}\right)^n \cos(n\theta) + \sum_{n=1}^{\infty} \frac{b_n}{n} \left(\frac{r}{r_0}\right)^n \sin(n\theta) \right] . \tag{3.5}$$

Here, r_0, Φ_0 are scaling factors for the electrode size and the applied voltages, respectively. a_n, b_n are dimensionless constants. The magnitude of the electric field in the center is given by $E_0 = (\Phi_0/r_0)\sqrt{a_1^2+b_1^2}$.

Some restrictions to the general solution (equation (3.5)) of Laplace's equation are made, such that the potential is suitable for an AG lens: In the origin, the electric field strength should be non-zero and symmetric under reflection in the x- and y-axis. Therefore, Φ should be, for instance, symmetric under reflection in the x-axis and anti-symmetric under reflection in the y-axis. This is achieved by setting $b_n = 0$ and using only odd terms of n. Keeping only the coefficients a_1, a_3, and a_5 and converting to Cartesian coordinates, equation (3.5) is simplified to

$$\Phi(x,y) = \Phi_0 \left(a_1 \frac{x}{r_0} + a_3 \frac{x^3 - 3xy^2}{3r_0^3} + a_5 \frac{x^5 - 10x^3y^2 + 5xy^4}{5r_0^5} \right) . \tag{3.6}$$

From this potential, the electric field magnitude can be calculated using

$$E(x,y) = \sqrt{\left(\frac{\partial\Phi}{\partial x}\right)^2 + \left(\frac{\partial\Phi}{\partial y}\right)^2} . \tag{3.7}$$

For $r < r_0$ this can be expanded in a power series in a_3/a_1 and a_5/a_1. For $a_5 \ll a_3 \ll a_1$ one obtains

$$E(x,y) = \\ E_0 \left(1 + \frac{a_3}{a_1}\frac{(x^2-y^2)}{r_0^2} + 2\left(\left(\frac{a_3}{a_1}\right)^2 - 3\frac{a_5}{a_1} \right) \frac{x^2y^2}{r_0^4} + \frac{a_5}{a_1}\frac{(x^4+y^4)}{r_0^4} + \dots \right) . \tag{3.8}$$

The first two terms have a harmonic form and are dominating. The successive terms represent the abberations of the AG lens. In order to produce these fields, hyperbolically shaped electrodes need to be chosen which surfaces map onto the equipotentials. For ease of machining, the electrodes of the AG decelerator used in this thesis are circular in the x-y plane, with which the electric field in

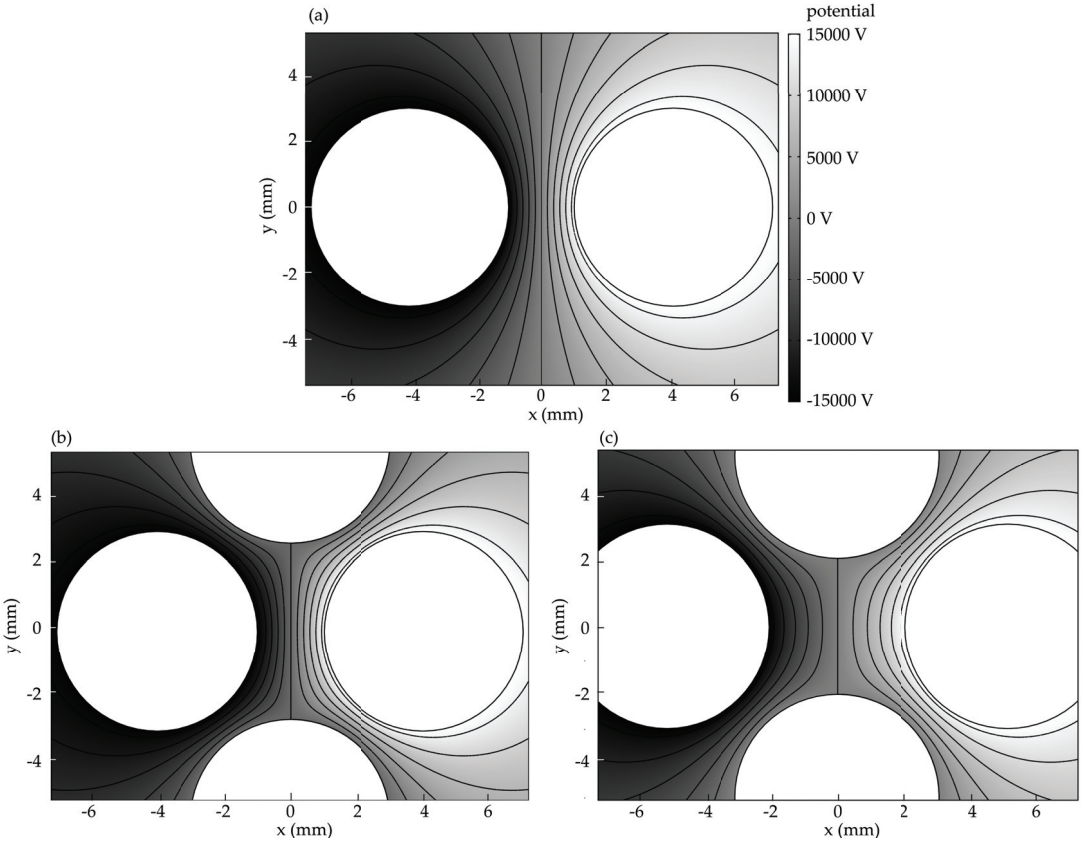

Figure 3.2: Electric potentials for different electrode configurations. The white circles represent the electrodes which have a diameter of 6 mm. A high voltage of ± 15000 V is applied between the two opposing electrodes positioned along the x-axis. For the four-electrode configuration the other two electrodes are grounded. (a) Two-electrode geometry, which is used in this thesis, where the distance of two opposing electrodes is 2 mm. (b) Potential for the asymmetric four-electrode configuration, where the distance between the two opposing electrodes positioned along the x-axis (y-axis) is 2 mm (5.3 mm). (c) Potential for a symmetric four-electrode configuration, where the distance between all opposing electrodes is 4 mm.

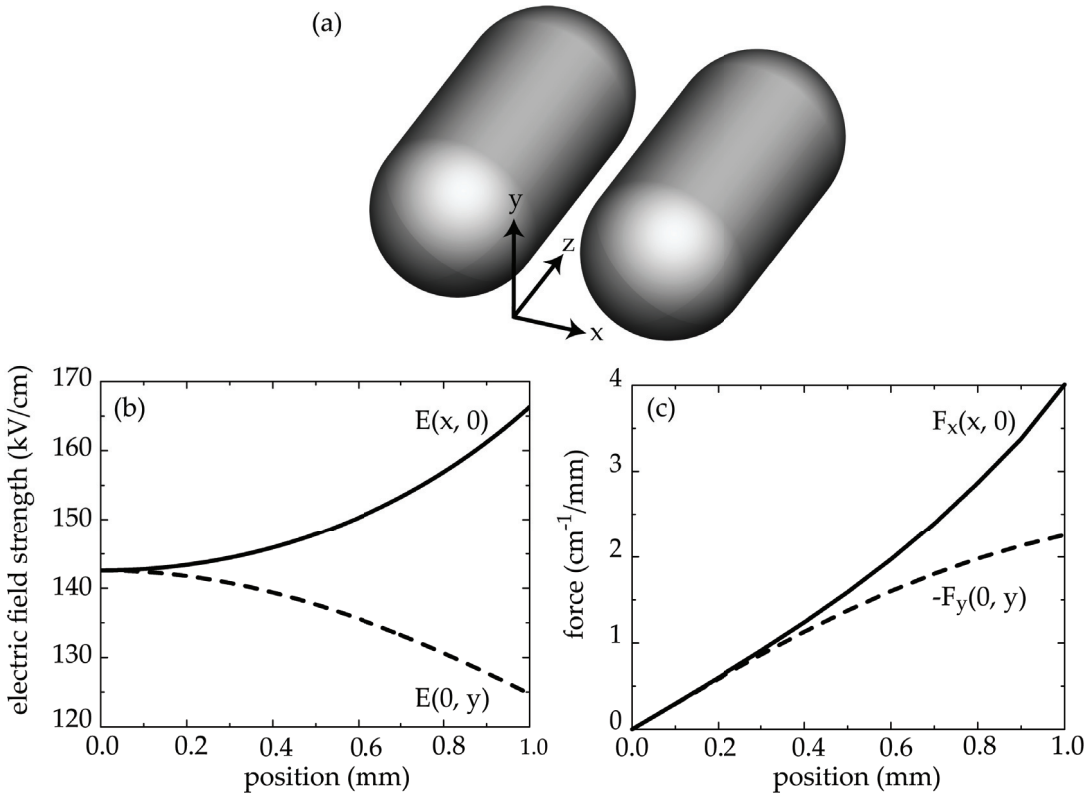

Figure 3.3: (a) Sketch of an electrode stage for the two-electrode configuration. (b) Electric field in the two transverse directions for the center of the AG lens. (c) The transverse forces of the ground state of benzonitrile, where $F_y(0, y)$ represents the focusing and $F_x(x, 0)$, the defocusing force. For direct comparison, $-F_y(0, y)$ is plotted.

equation (3.8) can be approximated to a certain extent. The electrodes in our experimental setup have a radius of 3 mm and a surface-to-surface distance of 2 mm. In the following, it is $r_0 = 1$ mm. The corresponding two-dimensional electrostatic potential, when a high voltage of ± 15000 V is applied to the electrodes, is shown in figure 3.2(a). From the fit of the numerically calculated potential using the program package Comsol [149] to the multipole expansion in equation (3.6), the coefficients are calculated. For $\Phi_0 = 14256$ V one obtains $a_1 = 1.0000$, $a_3 = 0.1415$, and $a_5 = 0.0194$. Especially the relatively large a_5 term results in an anharmonic electric field and, therefore, in an abberation of the AG lens.

Figure 3.3(a) shows a sketch of an electrode stage for the two-electrode configuration. Figure 3.3(b) shows the electric field along the two principal axes.

In figure 3.3(c), the forces for benzonitrile molecules in their ground state are depicted. It is shown that close to the axis the absolute value of the focusing and defocusing force are equal for small displacements from the molecular beam axis. For larger displacements, however, the absolute value of the defocusing force increases compared to the focusing force. This is due to the abberation of the AG lens for this electrode geometry, and results in a smaller acceptance of the AG decelerator than in the ideal case, where focusing and defocusing forces have the same absolute value. For molecules with a linear Stark effect, a good choice for the electrodes would be one that yields $a_5 = 0$ [148]. This can be approximated using two circular electrodes with a diameter of 6 mm centered at $(x, y) = (\pm 4$ mm, $0)$, on which the high voltage is applied, and two additional grounded electrodes centered around $(x, y) = (0, \pm 5.65)$ mm. The electric potential is shown in figure 3.2(b). For $\Phi_0 = 14211$ V and $r_0 = 1$ mm the multipole coefficients are $a_1 = 0.9932$, $a_3 = 0.13623$, and $a_5 = -0.0008$, resulting in a considerably smaller a_5 and, hence, a smaller abberation. The maximum electric field strength between neighboring electrodes for this configuration is only a few percent higher than in the two-electrode configuration, such that no electric flashovers should occur if a high voltage of ± 15000 V is applied to the electrodes. A disadvantage of this asymmetric four-electrode configuration is that one needs two times more electrodes, which have to be aligned precisely.

Another possibility is to arrange four circular electrodes on a square, where two opposing electrodes are addressed with a high voltage and the other two electrodes are grounded. The advantage of this symmetric four-electrode configuration is that the focusing and defocusing direction of the electrode pattern (see section 3.4) can be changed by applying the high voltage to the perpendicular electrode pair. When the molecules are decelerated to lower velocities, it is also possible to adapt the focusing and defocusing pattern to these lower velocities. The potential for a possible symmetric four-electrode configuration, where the electrodes are centered at the positions $(x, y) = (\pm 5$ mm, $0)$ and $(x, y) = (0, \pm 5$ mm$)$ and a high voltage of ± 15000 V is applied for the electrode pair oriented along the x-axis, is shown in figure 3.2(c). For $\Phi_0 = 6048$ V and $r_0 = 1$ mm it follows $a_1 = 0.9999$, $a_3 = 0.19676$, and $a_5 = -0.0094$. The negative a_5 coefficient has an absolute value about half as large as for the two-electrode case. The disadvantage of this asymmetric four-electrode configuration is a decrease of the electric field strength in the center by a factor 2.4, when the same voltages are applied. If in this configuration the high voltage is only increased by about 10 %, the same maximum electric field strength between neighboring electrodes is achieved as in the two-electrode configuration. Therefore, the electric high voltage cannot be increased considerably without risking electric flashovers. An even smaller a_5 value is achieved when the electrodes are placed at a square

with $(x, y) = (\pm 6 \text{ mm}, 0)$ and $(x, y) = (0, \pm 6 \text{ mm})$, but then the electric field is decreased by a factor of 3.5 compared to the two-electrode configuration.

For the AG deceleration, not only an electric field with small abberation, but also a high electric field strength on the molecular beam axis is needed in order to decelerate the molecules within a suitable number of electrode stages. Therefore, the two-electrode configuration or the asymmetric four-electrode configuration with less abberation should be preferred. The configuration with four electrodes arranged in a square, can be used for the transverse focusing of molecules as has been demonstrated for deuterated ammonia [56, 97], deuterated water molecules [55], and aminophenol [23]. The dynamics inside a quadrupole guide using AG focusing has recently been studied analytically [150].

3.3.2 End effects

In the following, the finite length of the electrodes is considered, and the consequences of the fields at the ends of the electrodes on the forces on the molecules are studied. Equation (3.4) describes the divergence of the force for a molecule with a linear Stark shift. Now, we restrict ourselves to small displacements from the molecular axis in order to simplify this equation. For the electrode pair shown in figure 3.3(a), the electrostatic potential is symmetric with respect to the x-z plane and antisymmetric in the y-z plane with $\phi = 0$ everywhere on this plane. Therefore, on the molecular beam axis, all terms of equation (3.4) vanish except for $\partial\Phi/\partial x$ and $\partial^2\Phi/\partial z\partial x$. Because $-\partial\Phi/\partial x$ is the only non-zero component of the electric field, it is $-\partial\Phi/\partial x = E$. On the axis, this leads to

$$\vec{\nabla} \cdot \vec{F} = \frac{\mu_{\text{eff}}}{E} \left(\frac{\partial E}{\partial z} \right)^2 . \tag{3.9}$$

Close to the center of the AG lens, it is $\partial E/\partial z = 0$ and $\partial F_z/\partial z = 0$. It follows, as shown in figure 3.3(c), that for the spring constants in the two transverse directions $k_x = -\partial F_x/\partial x$ and $k_y = -\partial F_y/\partial y$, it is $k_x = -k_y$ such that they are equal in magnitude but with opposite sign. This means that the focusing and defocusing forces close to the center of the lens are equal. However, in the fringe field at the end of the AG lens, it is $\partial E/\partial z \neq 0$ and $\partial F_z/\partial z \neq 0$. For a linear Stark shift, it is $k_z = -\partial F_z/\partial z = -\mu_{\text{eff}}\partial^2 E/\partial z^2$, and equation (3.9) results in

$$k_x + k_y = -\mu_{\text{eff}} \left(\frac{1}{E} \left(\frac{\partial E}{\partial z} \right)^2 - \frac{\partial^2 E}{\partial z^2} \right) \tag{3.10}$$

$$= \mu_{\text{eff}} E \frac{\partial}{\partial z} \left(\frac{1}{E} \frac{\partial E}{\partial z} \right) . \tag{3.11}$$

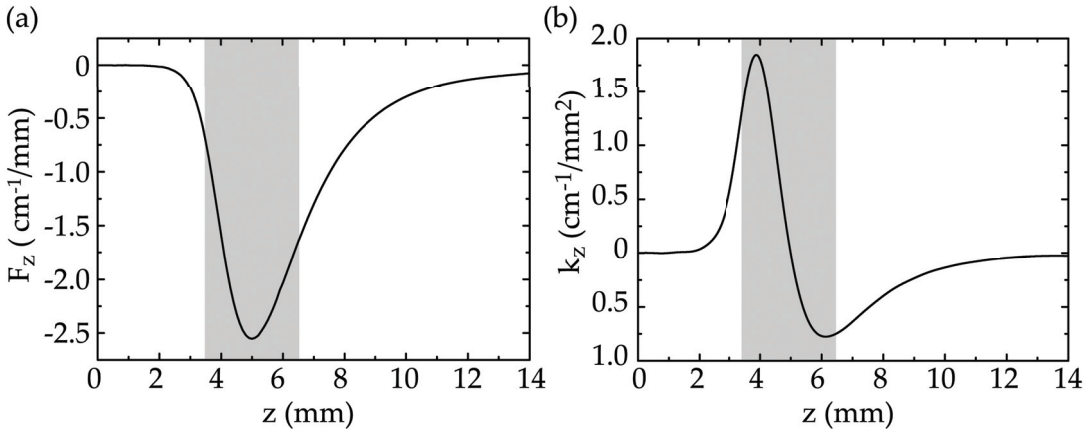

Figure 3.4: (a) Force F_z and (b) spring constant k_z for benzonitrile in its ground state plotted along the molecular beam axis as a function of z. The shaded areas highlight the region of the hemispherical end cap of the electrodes.

In figure 3.4(a), the force F_z and (b) the spring constant k_z for benzonitrile in its ground state along the molecular beam axis are given as a function of z for electrodes with hemispherical end caps, as shown in figure 3.3(a). The forces and spring constants are calculated for the case that the next electrode pair at a center-to-center distance of 20 mm to the previous electrode pair is arranged perpendicular and grounded. The shaded area represents the region of the hemispherical end cap, and $z = 0$ defines the center of the electrode pair, where $k_z = 0$. Molecules moving along the beam axis towards the end of the AG lens, experience a deceleration force, as F_z is negative. In the region between $z = 2$ mm and $z = 5$ mm the hfs molecules are bunched, which means that the molecular packet is focused in longitudinal direction. Between $z = 5$ mm and $z = 10$ mm the molecules are still decelerated, because F_z is negative, but are not bunched anymore, resulting in a broadening of the decelerated molecular packet.

Figure 3.5 shows the transverse forces at a transverse displacement of 0.1 mm from the molecular beam axis as a function of z. As already shown in figure 3.3(b), the transverse forces F_x(0.1 mm, 0, 0) = -F_y(0, 0.1 mm, 0) = 0.30 cm^{-1} are of equal strength close to the center of the electrodes. In the fringe field of the electrodes, i. e. , between the rounded end caps, the absolute value of the defocusing force $|F_x|$ strongly increases (by about 60 %) for $z = 3.9$ mm compared to its value inside the lens ($z = 0$ mm), while the absolute value of the focusing force F_y steadily decreases. In the deceleration process of molecules in hfs states, the area of the fringe fields where the defocusing force is larger than the focusing force, has to be exploited in order to longitudinally

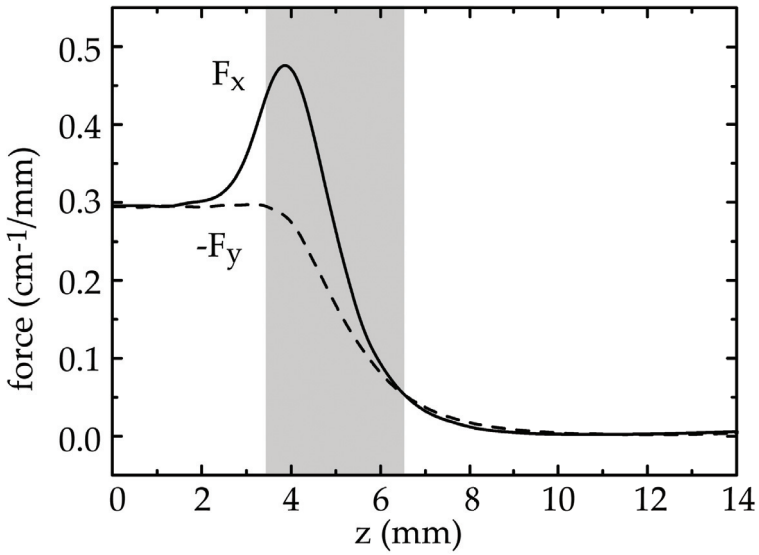

Figure 3.5: Transverse defocusing force F_x and focusing force with opposite sign $-F_y$ for the ground state of benzonitrile at a transverse displacement of 0.1 mm from the molecular beam axis as a function of z. The shaded area highlights the region of the hemispherical end cap of the electrodes.

bunch the molecules (see section 3.5 for details). This results in a decreased transverse acceptance for the deceleration of molecules in hfs states.

3.4 Analytical description of the equations of motion

In this section, the motion of molecules in the AG decelerator is analyzed. In a first approach, the transverse and longitudinal motion are treated independently. This is a good approximation for small velocity changes of the molecules. Later, the coupling of the transverse and longitudinal motion will be discussed.

3.4.1 Transverse motion

We can catch the essentials of the transverse motion by assuming that the molecule moves at a constant velocity v_z along the molecular beam axis. Furthermore, close to the beam axis, the molecule experiences a linear force that is focusing in one direction and defocusing in the other direction. The orientations of the lenses alternate. Inside a lens, the equation of motion along the molecular

beam axis can be written as

$$\frac{\partial^2 x}{\partial t^2} \pm \kappa^2 v_z^2 x = 0 \ , \tag{3.12}$$

which leads as function of z to

$$\frac{\partial^2 x}{\partial z^2} \pm \kappa^2 x = 0 \ . \tag{3.13}$$

The plus sign corresponds to a focusing force and the minus sign to a defocusing force, respectively. $\kappa/2\pi$ describes the number of oscillations per unit length and depends on the spring constant k_x by $\kappa = \sqrt{|k_x|/mv_z^2}$. The angular oscillation frequency Ω is

$$\Omega = \sqrt{\frac{|k|}{m}} = \sqrt{\frac{\mu_{\text{eff}}}{m}\frac{2E_0 a_3}{r_0^2 a_1}} \tag{3.14}$$

for a linear Stark effect and using the first order term of equation (3.8). Equation (3.13) is a Hill's equation, a linear differential equation of second order, and, therefore, its solution is uniquely determined by its initial values $x(z)$ and $v_x(z)$ and can be written as

$$\begin{pmatrix} x(z) \\ v_x(z) \end{pmatrix} = M(z|z_0) \begin{pmatrix} x(z_0) \\ v_x(z_0) \end{pmatrix} \ , \tag{3.15}$$

where $M(z|z_0)$ is the transfer matrix given by

$$M(z|z_0) = \begin{cases} \begin{pmatrix} \cos\kappa l & \frac{1}{\Omega}\sin\kappa l \\ -\Omega\sin\kappa l & \cos\kappa l \end{pmatrix} & F: \text{ focusing lens} \\ \begin{pmatrix} 1 & \frac{l}{v_z} \\ 0 & 1 \end{pmatrix} & O: \text{ drift space} \\ \begin{pmatrix} \cosh\kappa l & \frac{1}{\Omega}\sinh\kappa l \\ \Omega\sinh\kappa l & \cosh\kappa l \end{pmatrix} & D: \text{ defocusing lens} \end{cases} \tag{3.16}$$

and $l = z - z_0$. Depending on the case, the transfer matrix F and the transfer matrix D for a defocusing lens are used for the length L and the transfer matrix O in the drift regions S in between the lenses. The transfer matrices for different subintervals can be combined to

$$M(z_2|z_0) = M(z_2|z_1)M(z_1|z_0) \, . \tag{3.17}$$

Thus, an AG array can be written as $F(L) \cdot O(S) \cdot D(L) \cdot O(S)$, leading to the transfer matrix of a whole AG device with n such units $M = (FODO)^n$. For

the AG decelerator described in this thesis, the single lenses are combined to longer elements such that $M = (FO)\left((DO)^3(FO)^3\right)^4(DO)^2$. The advantage of combining short AG lenses to longer focusing or defocusing elements is that the molecules can be decelerated in every single electrode. At the entrance of the decelerator, only a single focusing element is used in order to achieve a good acceptance in both transverse directions. The trajectories are stable, when all elements of the transfer matrix remain bounded if n increases indefinitely. This is fulfilled for $-1 < \frac{1}{2}\mathrm{Tr}(M) < 1$ (see, for instance, reference 95).

As described in reference 95, the transfer matrix can be parameterized for a unit cell with length l_{cell} as

$$M(z + l_{\mathrm{cell}}|z) = \begin{pmatrix} \cos\phi + \alpha\sin\phi & \beta\sin\phi \\ -\gamma\sin\phi & \cos\phi - \alpha\sin\phi \end{pmatrix}, \tag{3.18}$$

where $\alpha(z)$, $\beta(z)$, and $\gamma(z)$ are the Courant-Snyder parameters, which have the same periodicity as the AG lens lattice. ϕ is the phase advance per unit cell. In our parametrization $\beta(z)$ and $\gamma(z)$ are given in the units s (second) and s^{-1}, in contrast to the particle accelerator literature, where the units are m (meter) and m^{-1}. The phase advance and Courant-Snyder parameters are related to one another such that

$$\alpha(z) = -\frac{v_z}{2}\frac{d\beta(z)}{dz}, \tag{3.19}$$

$$\gamma(z) = \frac{1 + \alpha^2(z)}{\beta(z)}, \tag{3.20}$$

$$\phi = \frac{1}{v_z}\int_z^{z+l_{\mathrm{cell}}} \frac{1}{\beta(z')}dz' . \tag{3.21}$$

In this parametrization, the transfer matrix that describes a single lattice unit is identical to the matrix for n units if ϕ is substituted for $n\phi$. The trajectories of the molecules are stable for $-1 < \cos\phi < 1$, which means that ϕ is real.

The solution of the differential equation (3.13) gives the trajectory of a molecule moving through the AG lattice, which is

$$x(z) = \sqrt{\beta(z)\epsilon_i}\cos\left(\phi(z) + \delta_i\right), \tag{3.22}$$

where ϵ_i and δ_i define the initial conditions of the particular molecule. The z-dependent phase $\phi(z)$ is given by $\phi(z) = 1/v_z\int_0^z 1/\beta(z')dz'$. The motion of a molecule is a product of two periodic functions. The wavelength of the first function is l_{cell} and of the second function is $2\pi l_{\mathrm{cell}}/\phi$. For $\phi \ll 2\pi$ the first

motion has a shorter period than the second motion and is called micromotion. The second motion is named macromotion. Similar trajectories are found for ions in Paul traps [107]. Furthermore, using equations (3.21) and (3.22) and it can be shown that

$$\gamma(z)x^2 + 2\alpha(z)xv_x + \beta(z)v_x^2 = \epsilon_i \,. \tag{3.23}$$

This describes an ellipse in the phase space of coordinates x and v_x. The shape of the phase space ellipse evolves periodically with z, but the phase space area $\pi\epsilon_i$ remains constant in accordance with Liouville's theorem. Molecules with the same value of ϵ_i lie all on the same ellipse, even if they differ in δ_i. All molecules with $0 < \epsilon_i < \epsilon$ are inside the ellipse defined by ϵ. The value ϵ defines the size of the beam in phase space and is called the emittance of the beam. Equation (3.22) shows that the transverse displacements of a set of molecules lie within a beam envelope given by the periodic function $\pm\sqrt{\beta(z)\epsilon}$. Analogously, the velocity spread of a set of molecules lies within a beam envelope defined by $\pm\sqrt{\gamma(z)\epsilon}$.

For an AG array with an aperture d_0, only trajectories with $\sqrt{\beta(z)\epsilon} < d_0/2$ are transmitted without loss. The transverse acceptance is defined as the phase space area occupied by the beam of the largest emittance consistent with this criterion and is $\pi d_0^2/(4\beta_{\max})$. The transverse acceptance of the AG decelerator obtained from numerical trajectory simulations is discussed in section 3.8.

3.4.2 Longitudinal motion

So far, only the transverse motion, which determines the focusing and transport of the molecules through the decelerator, has been discussed. For the deceleration of molecules, the longitudinal electric field gradients at the entrance and exit of the AG lenses are exploited. Therefore, the longitudinal motion has to be considered.

The electric field strength for the case that two successive electrode pairs are oriented parallel to each other and are both put on high voltage is shown in figure 3.6(a). The Stark energy for the ground state of benzonitrile along the molecular beam axis is shown in figure 3.6(b). The potential energy W can be expanded around the point of inflection defined by $\partial^2 W/\partial z^2 = 0$ at $z = z_i = 5.0$ mm in a Taylor series.

$$W(z + z_i) = W(z_i) + W'(z_i)z + \frac{1}{6}W'''(z_i)z^3 + \dots \,, \tag{3.24}$$

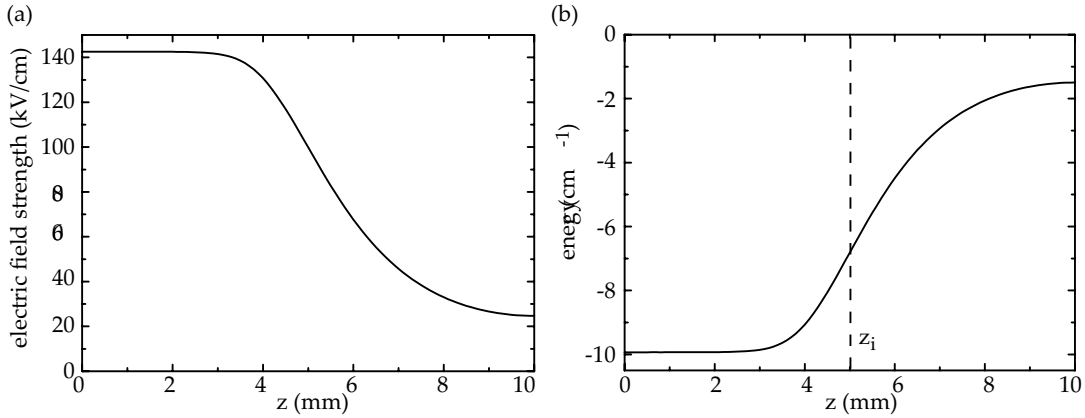

Figure 3.6: (a) Electric field strength and (b) energy of the ground state of benzonitrile in an electric field along the molecular beam axis. The dotted line marks the point of inflection.

where $W'(z_i) = \frac{\partial W}{\partial z}|_{z=z_i}$ and $W'''(z_i) = \frac{\partial^3 W}{\partial z^3}|_{z=z_i}$. Close to $z = z_i$, the potential energy is well approximated using the first two terms. By definition, the synchronous molecule is always at the same position within an AG lens when the high voltages are switched on and off. The position d at the relevant lens denotes the position of the synchronous molecule where the high voltage is switched off. Therefore, the change of kinetic energy $(W_{\text{lens}} - W(d))$ is for the synchronous molecule the same in every lens, where W_{lens} is the Stark shift of the molecule inside the lens. If the energy reduction per stage is small compared to the total kinetic energy, the change in energy on a distance scale larger than the size of an electrode stage can be described as originating from a constant average force [70]

$$F_d = \frac{W_{\text{lens}} - W(d)}{D}\,, \tag{3.25}$$

where D is the distance between to successive AG lenses. For a non-synchronous molecule being at position z when the high voltages are switched off, the difference between its force and the force on the synchronous molecule at d is expressed as

$$F - F_d = \frac{-W(z) + W(d)}{D} \approx -\frac{W'}{D}(z - d). \tag{3.26}$$

This is a harmonic oscillator, and the angular frequency with which the non-synchronous molecules oscillate around the synchronous molecule, is determined as

$$\omega_z = \sqrt{\frac{W'}{mD}}\,, \tag{3.27}$$

where m is the mass of the molecule. For benzonitrile in its ground state and the decelerator geometry used in this thesis, it is $D = 20$ mm and $W'(z_i) =$

5.07710^{-20} J/m from which the longitudinal frequency is calculated to $\omega_z/2\pi =$ 610 Hz, which means that molecules moving with 320 m/s experience about one oscillation period for the length of the decelerator.

The potential energy in an AG lens can also be analytically approximated by [151]

$$W(x,y,z) = W_0 \left(1 + \beta((y/r_0)^2 - (x/r_0)^2)\right) f(z)\,, \tag{3.28}$$

where

$$f(z) = \frac{\tanh(z'/l + L/2l) - \tanh(z'/l - L/2l)}{2\tanh(L/2l)} \tag{3.29}$$

gives a phenomenological approximation of the behavior along the molecular beam axis. W_0 is the potential at $z = 0$, r_0 determines the transverse aperture of the decelerator, β describes the transverse curvature of the potential, and l describes the curvature of the lens along the molecular beam axis. It is $z' = \mathrm{mod}(z - D, 2D) - D$, where $\mathrm{mod}(a, b)$ is the remainder on the division of a by b. For the parameters $W_0 = -9.9$ cm^{-1}, $r_0 = 0.001$ m, $L = 0.013$ m, $D = 0.020$ m used in this thesis, suitable parameters of the potential energy of benzonitrile in the ground state are $l = 0.002$ m and $\beta = 0.15$. However, the approximation of the potential along the molecular beam axis is not very good. Especially, the electric field in between two lenses is not described properly. Using the approximation, it is $W = 0$ in between two lenses, but in the case of two successive electrodes arranged parallel to each other, it is $W = 25$ kV/cm and for a perpendicular arrangement of two successive electrodes it is $W = 13$ kV/cm. Because of the curvature of the electrode at the end caps, the parameter L should not be the real length of the lens. An effective length about 10 % smaller gives a better representation of the real potential along the molecular beam axis. Furthermore, in the approximation, the parameter β has the same value for the focusing and defocusing direction. This is a good approximation for molecules close to the molecular beam axis. However, for molecules in hfs states the absolute value for the defocusing force is larger than for the focusing force further away from the molecular beam axis (see figure 3.3(c)). For a better description, two individual parameters, one for the focusing and one for the defocusing direction, would be needed. The fringe fields at the ends of the AG lens and the coupling between longitudinal and transverse motion are also not included in the analytical potential. In summary, the analytical potential can be helpful as a first approximation, but in order to achieve a quantitative description of all relevant effects in the AG decelerator, numerically calculated potentials are needed.

3.4.3 Coupling between transverse and longitudinal motion

The transverse and longitudinal motion are coupled in the AG decelerator. This is immediately clear from equation (3.12), where the transverse motion also depends on v_z, which is not constant during the deceleration process. If the molecules are decelerated too much without changing the focusing parameters, the molecules will not be accepted. Therefore, the focusing length f has to be reduced during the deceleration process. This is experimentally shown for the deceleration of OH in its lfs state in chapter 7. When the molecules are decelerated to low velocities, it is useful to reduce the length of the electrodes or, alternatively, to change the $(FO)^m(DO)^m$ pattern such that the value of m is reduced over the length of the decelerator. For the deceleration to very low velocities, advanced electrode geometries with smaller abberation effects are desirable (see section 3.3).

3.5 High voltage switching schemes

For the description of the time sequence, at which the high voltages applied to the AG decelerator are switched on and off, we use the concept of a synchronous molecule (see section 3.4). As discussed above, a molecule in its hfs state will gain kinetic energy when it enters the AG lens and will lose kinetic energy when it leaves the lens. In figure 3.7, the high voltage switching scheme for the synchronous molecule in a hfs state is depicted. Figure 3.7(a) shows transverse focusing, as discussed above. The high voltages for the synchronous molecule are switched on and off symmetric around the center of the AG lens ($z = 0$ mm) and, therefore, no change in velocity occurs. Additionally, the molecular packet is bunched in longitudinal direction. The time interval during which the high voltages are applied to an AG lens, in combination with the velocity of the synchronous molecule, determine the focusing length f. Figure 3.7(b) shows the switching scheme for the deceleration of molecules in their hfs states. The voltages are switched on when the synchronous molecule is inside the AG lens and off when the molecule is at the falling flank of the electric field. The amount of kinetic energy that is removed per AG lens depends on the position of the synchronous molecule on the molecular beam axis at the time when the high voltages are switched off. This position, relative to the center of the AG lens, is denoted by d. The high voltage is not switched off at the minimum of the electric field, but at different positions up to $z = 5$ mm at the falling flank. This allows to bunch a molecular packet: faster molecules are already closer to the electric field minimum and are decelerated more strongly, while slower molecules

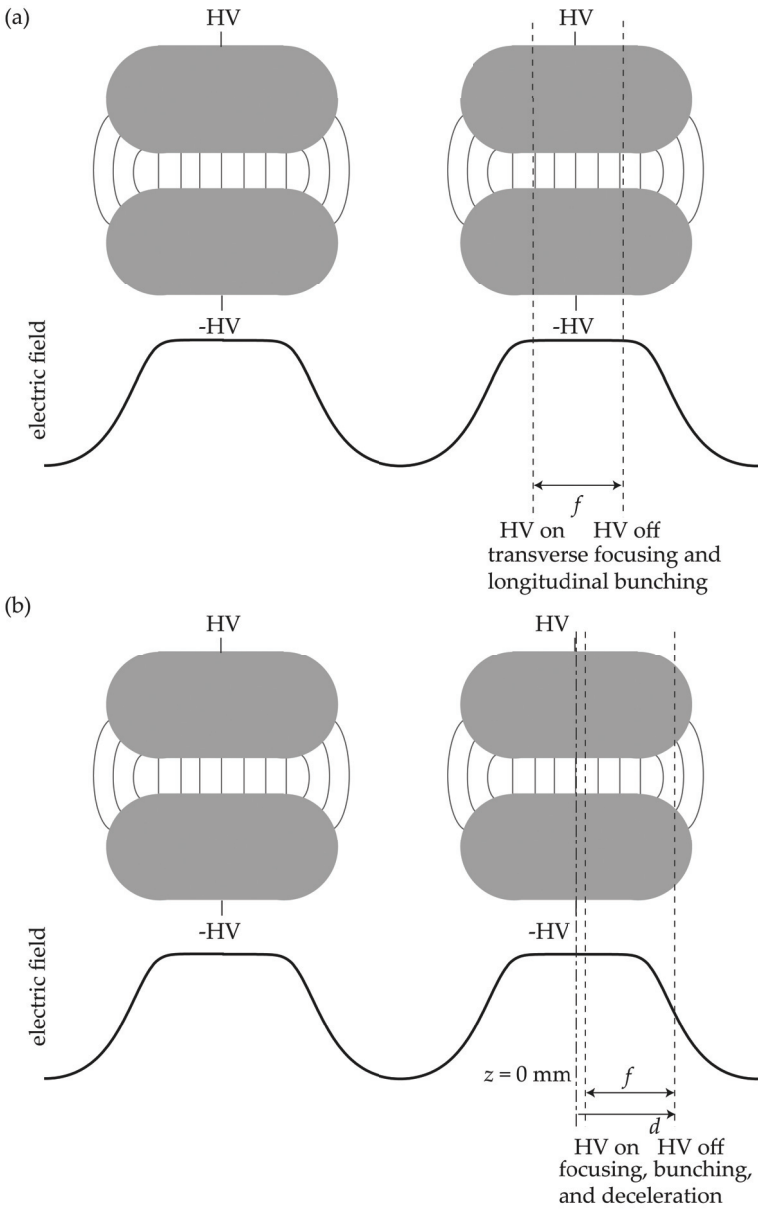

Figure 3.7: Sketch of two electrode pairs and the corresponding electric field along the molecular beam axis. The high voltage (HV) switching procedures for (a) focusing and (b) deceleration of molecules in high-field-seeking states are indicated. f is the focusing length and d the deceleration position relative to the center of the electrode pair.

that lag behind are decelerated less. In this way, a narrow spread of longitudinal position and velocity is achieved throughout the decelerator. This is known as longitudinal phase stability and has been studied previously for the normal Stark decelerator for the deceleration of molecules in lfs states [70]. Alternatively, a molecule in a hfs state could also be accelerated by switching the high voltage on at the rising flank of the electric field and off when the molecule is inside the AG lens.

The AG decelerator can also be used to focus and decelerate molecules in lfs states. This is demonstrated experimentally in this thesis for OH in its lfs $X^2\Pi_{3/2}, v = 0, J = 3/2f$ state (see chapter 7). In order to achieve phase stability in this case, the field must be switched on and off a second time, when the synchronous molecule is in between two electrode pairs. Figure 3.8(a) shows the switching scheme for transverse focusing and longitudinal bunching of molecules in a lfs state. The parameter b determines the amount of longitudinal bunching and describes how long the high voltage is switched on, while the synchronous molecule is in between two electrode pairs. In figure 3.8(a), the bunching parameter b is applied symmetrically around the minimum of the electric field ($z = -10$ mm). That way, faster molecules as the synchronous molecule are decelerated and slower ones accelerated. This results also in an oscillation of the molecules in the packet around the synchronous molecule, and the packet is effectively kept together. To achieve transverse focusing, the fields are then switched on and off once more per stage when the molecules are inside the electrode pair, and the parameter f describes the transverse focusing length.

Figure 3.8(b) illustrates the switching scheme for the deceleration of molecules in lfs states. The position d is defined relative to the minimum of the electric field strength, and its value on the rising flank of the electric field determines the amount of kinetic energy removed per stage. The deceleration of molecules in lfs states is more efficient than for molecules in hfs states, which is due to the better transverse focusing and longitudinal bunching properties of the fields for molecules in lfs states. For molecules in lfs states, the focusing force is larger then the defocusing force, which results in a larger acceptance of the decelerator. The electric field along the molecular beam axis allows to longitudinally bunch molecules in lfs states in a larger region than molecules in hfs states. This is discussed in more detail in combination with experimental results in chapter 7.

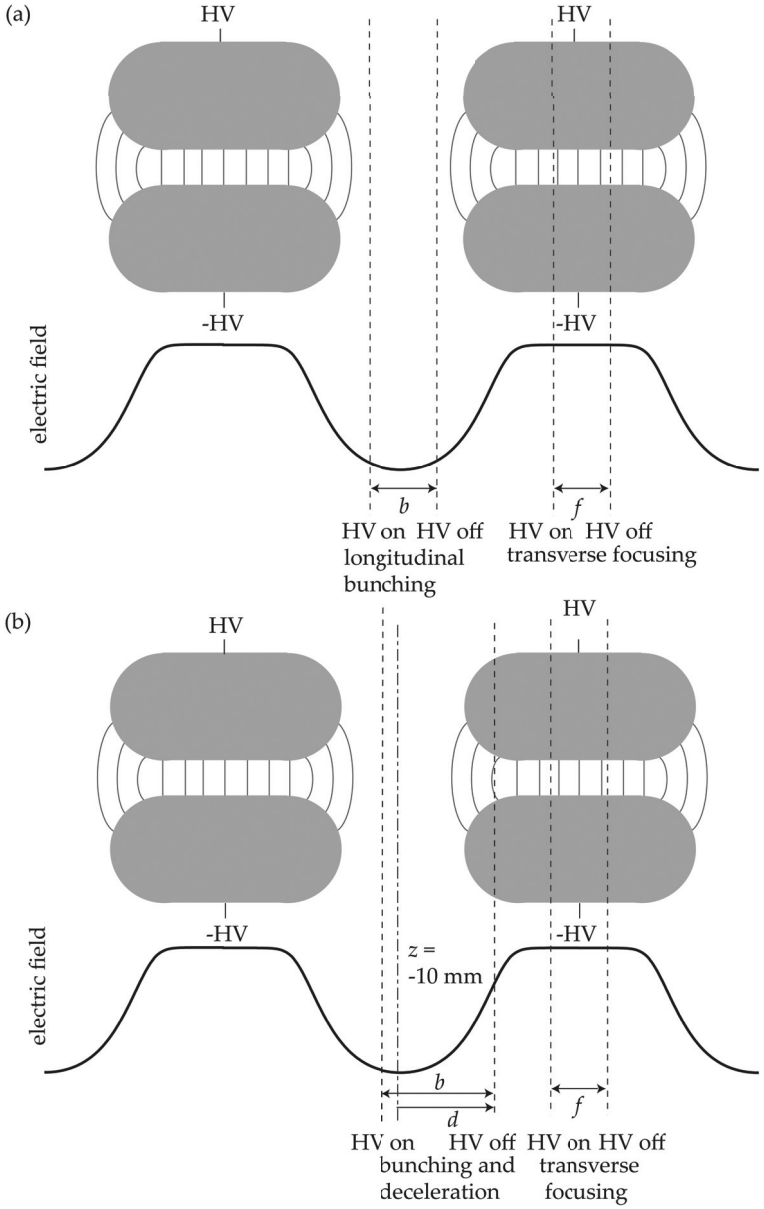

Figure 3.8: Sketch of two electrode pairs and the corresponding electric field along the molecular beam axis for an electrode pair. The high voltage (HV) switching procedures for (a) focusing and (b) deceleration of molecules in low-field-seeking states are indicated. f is the focusing length, b the bunching length and d the deceleration position relative to the minimum of the electric field. For molecules in low-field-seeking states, the voltages are switched on and off twice as often as for molecules in high-field-seeking states.

3.6 Numerical electric field calculations

A precise simulation of the electric field in the decelerator is needed to determine the force on a molecule in this field accurately. The three-dimensional electric field and its gradient in the electrode stages of the AG decelerator are calculated by finite element methods using the program package Comsol Multiphysics [149]. A sketch of an electrode pair as used in our setup is shown in figure 3.3(a). The electrodes of an electrode stage are 13.0 mm long, have a diameter of 6.0 mm, spherical end caps with a radius of 3.0 mm, and are 2.0 mm apart. The drift space between two successive electrode pairs along the molecular beam axis is $S = 7.0$ mm. To calculate the electric field inside an electrode pair, the two opposing electrodes with high voltages of $+15$ kV and -15 kV are placed in the center of a grounded cylinder with an outer diameter of 100 mm. The electric field is calculated for the two different configurations of successive electrode stages, which occur in the AG decelerator (see figure 3.1). In both cases, the center of the first electrode pair is at $x = y = z = 0$ mm. In one case, the two successive electrode stages are both oriented along the same transverse direction, for instance, both along the x-direction and both set on high voltage. In the other case, the two successive electrodes are oriented in different directions, for example, the first electrode stage, which is the one set on high voltage in the calculations, is oriented along the x-direction and the second electrode stage, which is grounded, along the y-direction. For this geometry, the following symmetry planes are present: The x-y plane at $z = 0$ mm and $z = 10$ mm ($z = 20$ mm for the second case), the x-z plane for $y = 0$. The y-z plane in between the electrode pair with opposing high voltages is for $x = 0$ an antisymmetry plane. In electrostatics, antisymmetry correspondences to the ground boundary condition. Because the mesh generation in Comsol Multiphysics is problematic at stiff edges, here only the x-y symmetry plane is used for the electric field calculations. Hence, the electric field is calculated for half an electrode pair (cut in the x-y plane at $z = 0$ mm) inside the surrounding cylinder with end caps at $z = 0$ mm and $z = 10$ mm (or $z = 20$ mm), which have symmetry boundary conditions. For an efficient electric field calculation, a fine mesh with a maximum element size of 0.0002 mm^3 is generated inside a cuboid centered about the molecular beam axis with the dimensions $x \times y \times z = 4$ mm $\times$ 4 mm $\times$ 10 mm. Outside this cuboid a relatively course mesh is generated. The norm of the electric field is calculated and both the norm and its derivatives in all three directions are exported from Comsol on a $x \times y \times z = 3$ mm $\times$ 3 mm $\times$ 10 mm grid with a step size of 0.1 mm. The electric field of the whole decelerator is described by rotations and combinations of the electric fields for the two cases of single electrode stages. In the following section, the trajectory simulations using the numerically calculated electric fields are discussed.

3.7 Numerical trajectory simulations

For an exact description of the motion of molecules in an AG decelerator, three-dimensional electric field calculations (see section 3.6), the Stark shifts of the molecular levels (see sections 2.1.3 and 2.3.3), and three-dimensional trajectory simulations are necessary. These trajectory simulations also allow to study effects due to coupling between longitudinal and transverse motion (see chapter 7). The trajectories are obtained from numerical integration of the three-dimensional equations of motion for the molecules in the electric field of the AG decelerator using Runge-Kutta methods. These calculations are performed with the home-built software package libcoldmol [120].

For the simulations, a molecule in a specific quantum state and a certain electrode pattern of the AG decelerator are used. The initial six-dimensional phase space distribution of the molecular packet is described by the mean values of the initial positions and velocities. Their spatial widths in the transverse plane Δx and Δy are defined by the diameter of a uniform circular distribution. The widths of the spatial longitudinal direction Δz and of the velocities Δv_x, Δv_y, and Δv_z are defined by the full widths at half maximum (FWHM) of Gaussian distributions. In this range, the initial phase space position of a certain molecule is randomly chosen. Furthermore, the initial time t_0 and the initial time width Δt (FWHM of Gaussian distribution) of the molecular packet are defined. Using the parameters f, d, and b for the switching schemes, a switching time sequence is calculated from the longitudinal (one-dimensional) motion of the synchronous molecule. This switching sequence is then used in the three-dimensional trajectory simulation of the whole molecular packet. A delay time, which is related to the time of flight (TOF) of the synchronous molecules from the nozzle to the beginning of the decelerator, determines the delay between the initial time and the beginning of the switching sequence. Furthermore, the position and size of the skimmer are included in the simulations. For molecules with stable trajectories through the decelerator, TOF profiles are determined. The properties of the laser detection are included in the simulations. For the TOF profiles, only molecules are considered which are in the centered rectangle with the size $x \times y = 1$ mm $\times$ 20 mm. The rectangle represents the relevant size of the detection laser beam. Furthermore, the laser line width and Doppler broadening effects are considered. For the calculation of TOF profiles, typically 20 million molecular trajectories are simulated. The calculation time is about 120 min for 20 million trajectories on one CPU of our Opteron cluster. From the simulations, also the phase space distributions at different positions of the decelerator are obtained. The exact parameters and results of the trajectory calculations are discussed in combination with the experimental data in chap-

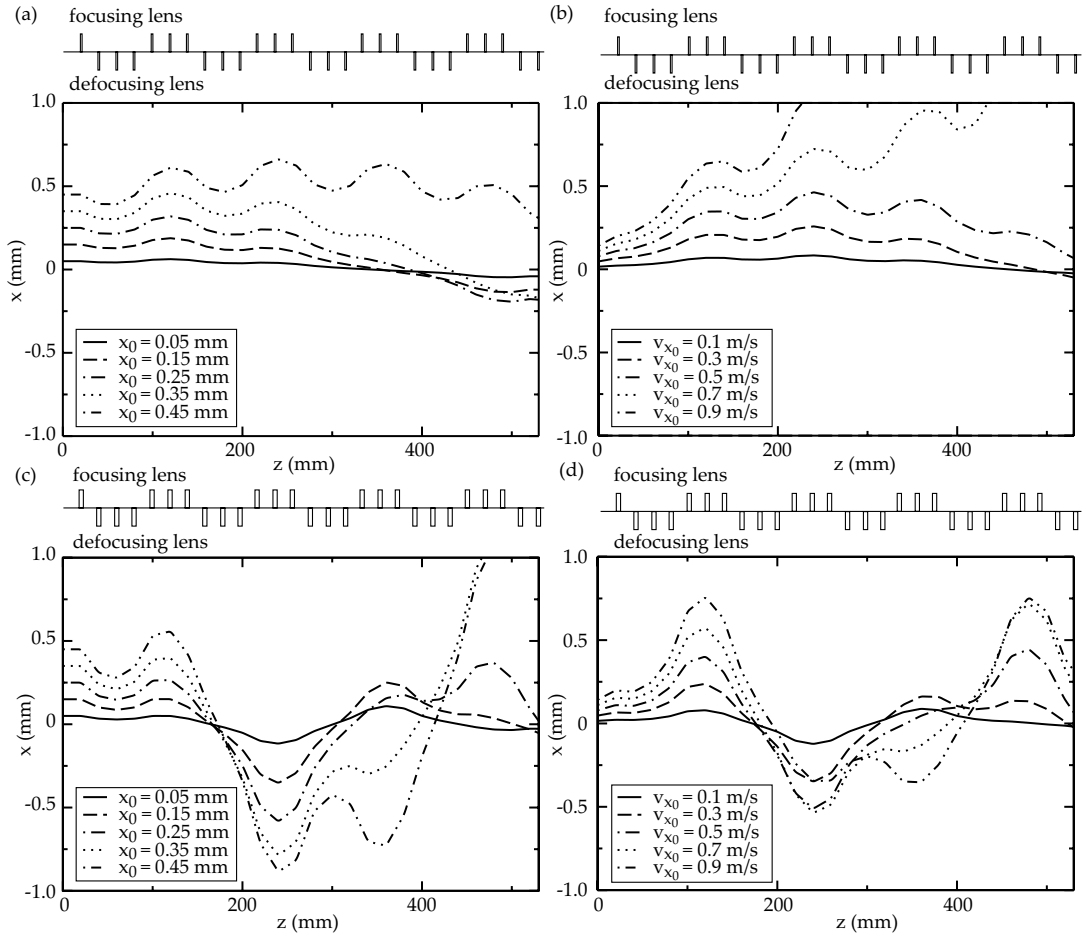

Figure 3.9: Trajectories of some benzonitrile molecules in their ground state in the alternating-gradient decelerator. (a) and (b) show trajectories for weak focusing with a focusing length of $f = 2$ mm and (c) and (d) for strong focusing with $f = 5$ mm. The arrangement of the focusing and defocusing AG lenses for the x-direction is indicated above the plots. The molecules move at a constant velocity of $v_z = 320$ m/s. Simulations for different initial transverse positions x_0 as indicated and for $v_{x_0} = 0$ are given in (a) and (c). Panels (b) and (d) show the results for different transverse velocities v_{x_0} as indicated and for $x_0 = 0$. Further initial conditions are $y_0 = z_0 = 0$ mm and $v_{y_0} = 0$ m/s.

ter 6 for benzonitrile and in chapter 7 for OH, respectively.

Figure 3.9 shows some typical trajectories for benzonitrile molecules in their ground state. The focusing or defocusing behavior of the AG lenses is indicated. All trajectories have the same initial conditions for the longitudinal velocity of $v_{z_0} = 320$ m/s, which corresponds to the experimental mean velocity of benzonitrile seeded in xenon, the transverse velocity $v_{y_0} = 0$ m/s, and the initial positions $y_0 = z_0 = 0$ mm. The trajectories in figures 3.9(a) and (c) differ in their transverse starting position x_0, but have the same initial conditions for $v_{x_0} = 0$ m/s. For weak focusing (figure 3.9(a)), the displayed trajectories are stable throughout the length of the decelerator, whereas for stronger focusing (figure 3.9(c)), the trajectories with a larger displacement of $x_0 = 0.35$ mm and $x_0 = 0.45$ mm are not stable and leave the decelerator. In contrast, the trajectories in figures 3.9(b) and (d) differ in their transverse initial velocity v_{x_0}, but have the same initial position $x_0 = 0$ mm. In this case, for strong focusing all displayed trajectories are stable, but for weak focusing the trajectories with $v_{x_0} = 0.7$ m/s and $v_{x_0} = 0.9$ m/s are unstable. This shows that for stronger focusing the transverse spatial acceptance is decreased, while the transverse velocity acceptance is increased and vice versa.

In the plots, the superposition of the micromotion and macromotion is clearly seen, as analytically predicted by equation (3.22). The amplitude of the micromotion with the wavelength 120 mm will increase if the focusing strength or the transverse displacement increases. The wavelength of the macromotion is larger in the case of weak focusing and smaller for strong focusing, as expected from the discussions above. The analysis of trajectories with different initial conditions shows that the transverse size of the molecular beam has a minimum at the center of the defocusing triplet and a maximum at the center of the focusing triplet. This behavior is at the basis of the dynamic stability of the AG decelerator [106].

3.8 Transverse acceptance and misalignment

In order to obtain the transverse acceptance of the decelerator, one million trajectories of benzonitrile molecules in a 96 stages long decelerator with a $((FO)^3(DO)^3)^{16}$ grid have been calculated. From the trajectory simulations, the ratio of molecules which are detected behind the decelerator compared to the total number of molecules is determined. This ratio is multiplied by the initial four-dimensional phase space volume to obtain the transverse acceptance. The transverse acceptance of the AG decelerator for benzonitrile molecules in

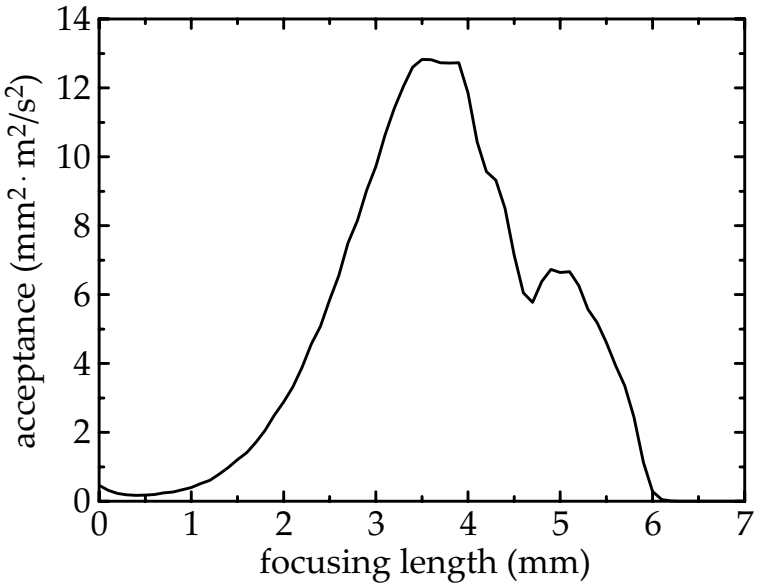

Figure 3.10: Transverse acceptance of a AG decelerator with a $((FO)^3(DO)^3)^{16}$ grid for benzonitrile molecules in the ground state at a velocity of 320 m/s.

their ground state as a function of the focusing length f is given in figure 3.10. A maximum acceptance is obtained at $f = 3.6$ mm, and a smaller side maximum occurs around $f = 5.0$ mm. For $f > 6.2$ mm all molecules are defocused and not accepted. For such a long decelerator, contributions from molecules on metastable trajectories are negligible. The molecules travel with a constant velocity of $v_z = 320$ m/s throughout the decelerator, and no longitudinal velocity spread is assumed. The initial molecular packet is uniformly spread in a phase space region with $\Delta x \times \Delta y \times \Delta v_x \times \Delta v_y = 2$ mm $\times 2$ mm $\times 10$ m/s $\times 10$ m/s. It should be noted that if the acceptance is obtained from three-dimensional trajectory simulations and the longitudinal spread of the packet as well as bunching effects are considered, the optimum acceptance will be achieved for $f = 5$ mm in agreement with experimental measurements (see chapter 6.5).

Misalignments of the electrodes cannot be avoided completely in a real decelerator, which has consequences for the transverse acceptance. In order to discuss this issue in more detail, the transverse acceptance is determined from trajectory calculations of benzonitrile molecules in their ground state in a $((FO)^3(DO)^3)^{16}$ configuration with 96 electrode stages for $v_z = 320$ m/s and $f = 3.6$ mm. The decrease of the transverse acceptance as a function of the misalignment of the electrodes is shown in figure 3.11. In the simulations, two different cases of misalignment in the two transverse directions are considered. For alternating

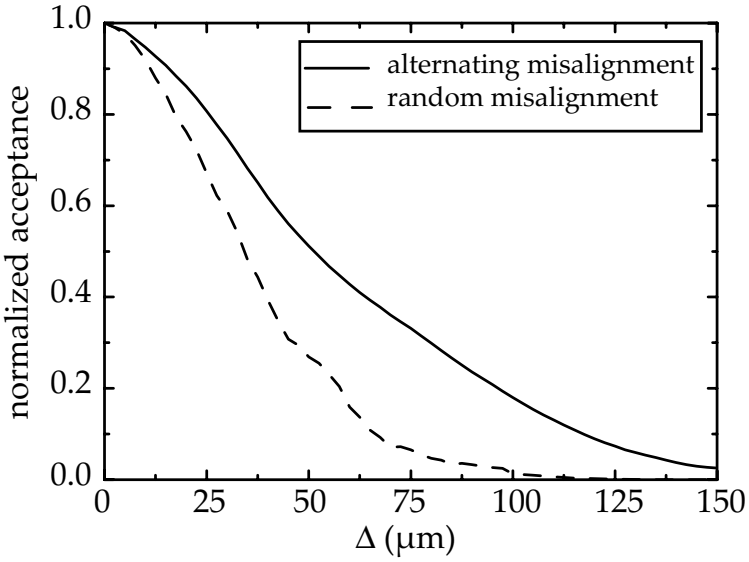

Figure 3.11: Decrease of the transverse acceptance for a $((FO)^3(DO)^3)^{16}$ grid as a function of the degree of misalignment Δ for alternating (solid line) and random (dashed line) misalignment. See text for details.

misalignment, it is assumed that the centers of successive AG lenses are alternately displaced by $+\Delta$, $-\Delta$, $+\Delta \ldots$. In the second case, the values for the displacements of the lenses in both transverse directions are chosen randomly from a Gaussian distribution with a standard deviation of Δ. The normalized acceptance given for random misalignment is obtained from the average of the acceptances of ten randomly chosen electrode stage displacements for the decelerator with the same standard deviation. In our AG decelerator setup, the real transverse misalignment is about $\Delta \approx 50\,\mu$m (see chapter 4.4). This means that in the case of alternating misalignment the normalized acceptance is reduced to 51 % and in the case of random misalignment to 27 %. Because the exact misalignment of single electrode pairs of the decelerator is difficult to determine, the random misalignment may be regarded as a good approximation. However, misalignment effects due to the displacements of the individual electrodes in single AG lenses, which also occur in our setup, are not considered, because new electric field calculations for every misalignment value would be necessary. This means that the real decrease of the transported molecules throughout the decelerator may be worse than the effects shown in figure 3.11. A further discussion of the misalignment effects including the displacements in longitudinal direction is given in chapters 6.3 and 7.4, when the agreement between measurements and simulations is discussed.

Chapter 4

Experimental setup

4.1 Overview

A new alternating-gradient decelerator apparatus for the focusing and deceleration of large molecules has been set up. All focusing and deceleration experiments presented in chapters 6 and 7 are performed in the newly designed and built molecular beam machine. The overall setup has a modular design to allow for an easy extension.

Figure 4.1 shows an overview of the experimental setup. Benzonitrile is co-expanded in xenon through a pulsed nozzle. 27 mm downstream from the nozzle, the molecules pass a skimmer and then enter the AG decelerator. The decelerator, in which the molecules are focused and decelerated, consists of 27 AG lenses arranged along the molecular beam axis, and has a total length of 533 mm. For all pairs of electrodes, voltages are switched between ±15 kV and ground. Alternatively, a bias voltage of up to ±300 V can be applied. The applied high voltages create a maximum electric field strength of 142.5 kV/cm on the molecular beam axis. Behind the decelerator benzonitrile molecules are detected by laser-induced fluorescence (LIF) on the $S_1, v' = 0 \leftarrow S_0, v'' = 0$ transition at 274 nm using time-resolved photon counting. A frequency-doubled and frequency-stabilized, narrow-linewidth, continuous ring dye laser is used for rotational-state-specific detection.

The measurements for the deceleration of OH are performed in the same setup, with some modifications to the source and the detection. HNO_3 is co-expanded in xenon. OH is produced from HNO_3 via photodissociation at 193 nm. Downstream from the nozzle, the molecules are skimmed and then enter the decelerator chamber. OH molecules exiting the AG decelerator are also detected

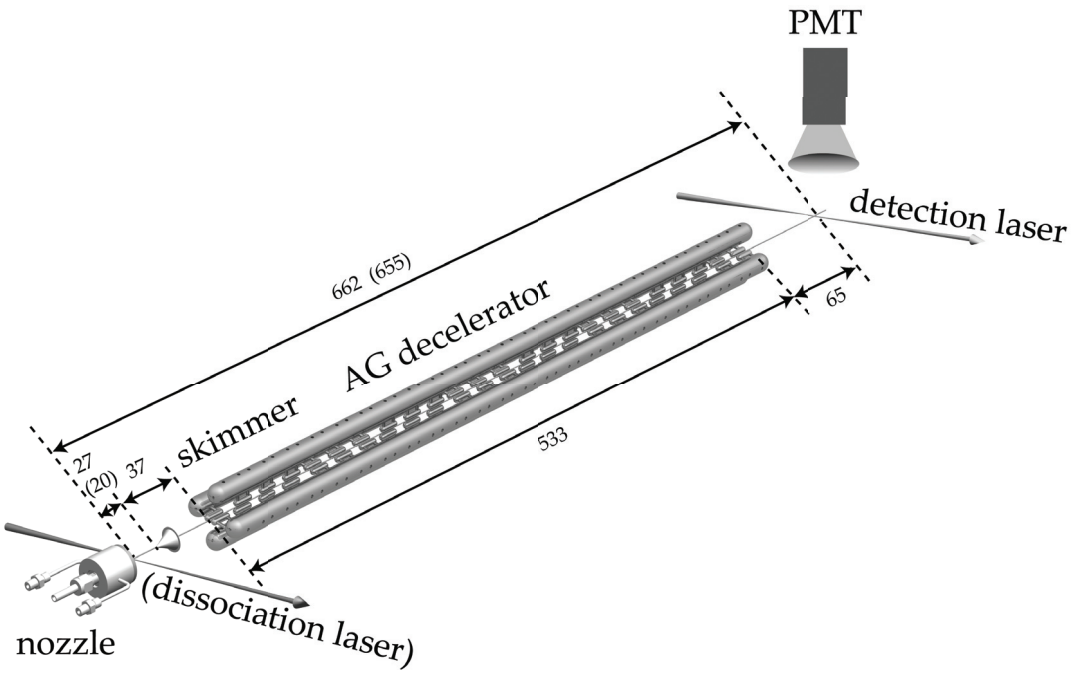

Figure 4.1: Sketch of the experimental setup for the focusing and deceleration of benzonitrile and OH. Benzonitrile is co-expanded in xenon. For OH experiments HNO_3 is co-expanded in xenon and OH is produced via photodissociation at 193 nm. After the supersonic expansion the molecular beam is skimmed. The molecules are focused and decelerated using the alternating-gradient (AG) decelerator and finally detected by laser-induced fluorescence with a photomultiplier tube (PMT). All distances are given in mm. The distances for the experiments with OH, which differ from the one for benzonitrile, are given in brackets.

by LIF via time-resolved photon counting after excitation on the $A^2\Sigma^+_{1/2}, v = 1 \leftarrow X^2\Pi_{3/2}, v = 0$ transition at 282 nm.

4.2 Vacuum system

The experiment is performed under high vacuum conditions. A sketch of the vacuum system is shown in figure 4.2(a) and a photo in figure 4.2(b). It is composed of three stainless steel vacuum chambers, namely the source chamber, the deceleration chamber, and the detection chamber. Each chamber consists of a tube with an inner diameter of 235 mm, two CF 250 flanges at the ends, and other flanges for various purposes, like detection, mounting of pressure gauges, and mounting of electric feedthroughs. A 1.5 mm diameter skimmer (Beam Dynamics, model 1) separates the source chamber from the differentially pumped deceleration and detection chamber. The skimmer is mounted directly on a home-built gate valve [152], which is integrated in a CF 250 flange. An explosion drawing of the gate valve is shown in figure 4.3. The skimmer mount and the gate valve are optimized for a small distance of 10 mm between the base of the skimmer and the beginning of the deceleration chamber. This short distance allows for a small molecular packet and a high molecular density at the beginning of the AG decelerator. Free space on both sides of the skimmer is provided to not disturb the supersonic expansion. The skimmer is fixed on a sledge which is moved using a linear motion feedthrough mounted on the CF 16 flanges. The vacuum seal is provided by a Viton O-ring. Two levers, moved by two linear motion feedthroughs, are used to fix the sledge in the skimming or sealing position. The CF 100 flanges at the sides and CF 63 flange at the top allow for optical access between the nozzle and the skimmer.

The vacuum fore pressure of $7 \cdot 10^{-2}$ mbar is provided by two oil-free piston pumps (Pfeiffer Vacuum, XtraDry 150-2), which are connected to a fore-vacuum line. The fore-vacuum regions for the source chamber and the remaining chambers are separated by a valve. Because of the gas load of the molecular beam, a 1380 l/s turbo molecular drag pump (Pfeiffer Vacuum, TMU1601 P) mounted on a CF 250 flange is used to pump the source chamber. Under normal operation conditions and at a repetition rate of 40 Hz, a pressure of about $2 \cdot 10^{-5}$ mbar is achieved. In the deceleration and detection chamber the pressure is $8 \cdot 10^{-8}$ mbar. Without the molecular beam the pressure in the deceleration chamber is about 10^{-9} mbar. A 230 l/s turbo molecular drag pump (Pfeiffer Vacuum, TMU 261 P) mounted on a CF 100 flange pumps the deceleration chamber, and a 920 l/s turbo molecular pump (Pfeiffer Vacuum, TMU 1001 P) mounted on a CF 200 flange pumps the detection chamber. In both high vacuum chambers the pres-

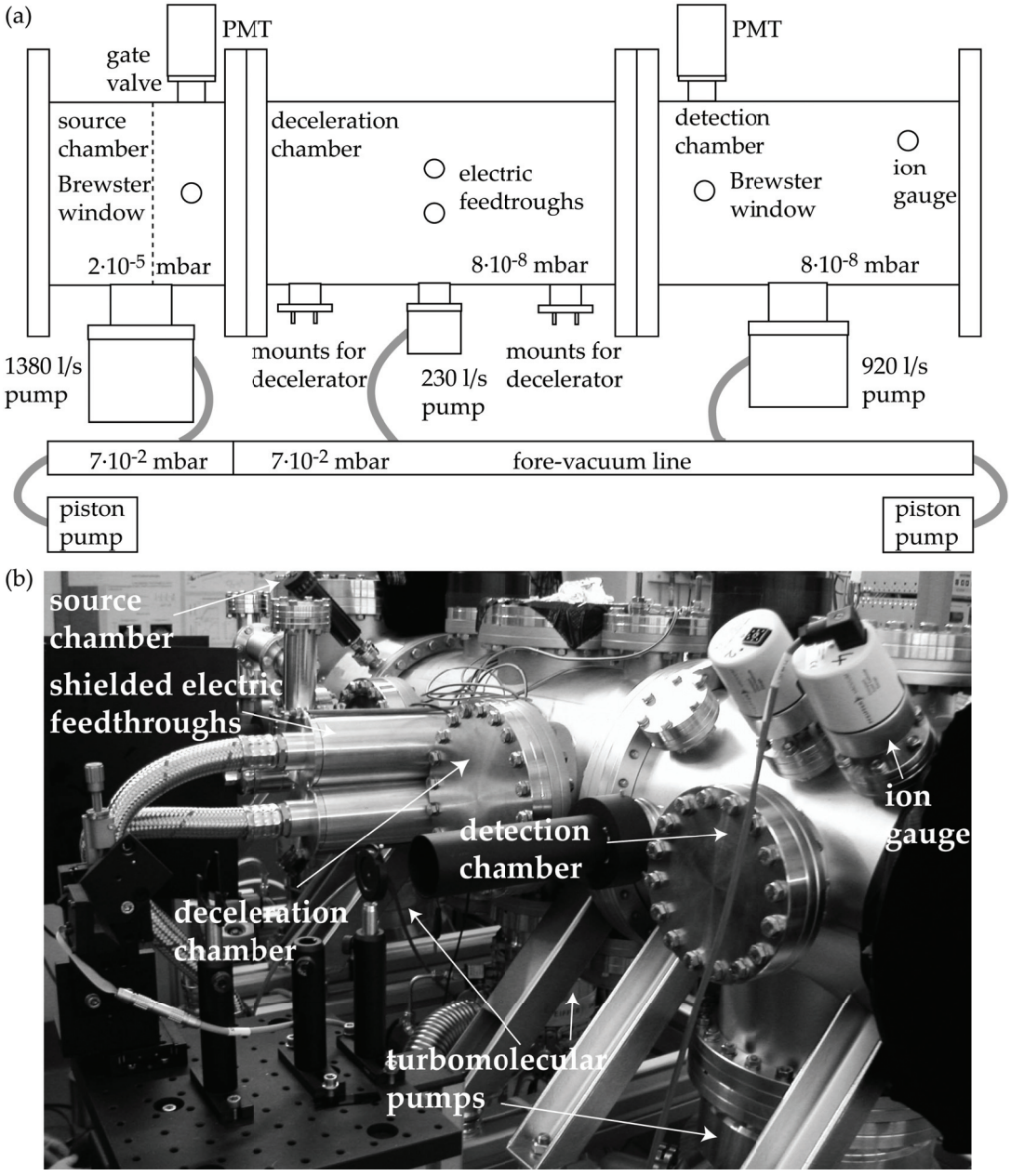

Figure 4.2: (a) Sketch of the vacuum system. (b) Photo of the vacuum chambers of the alternating-gradient decelerator setup. The source chamber, deceleration chamber, and detection chamber with its molecular drag pumps are visible. The electric shielding of the feedthroughs and the ion gauge are labelled.

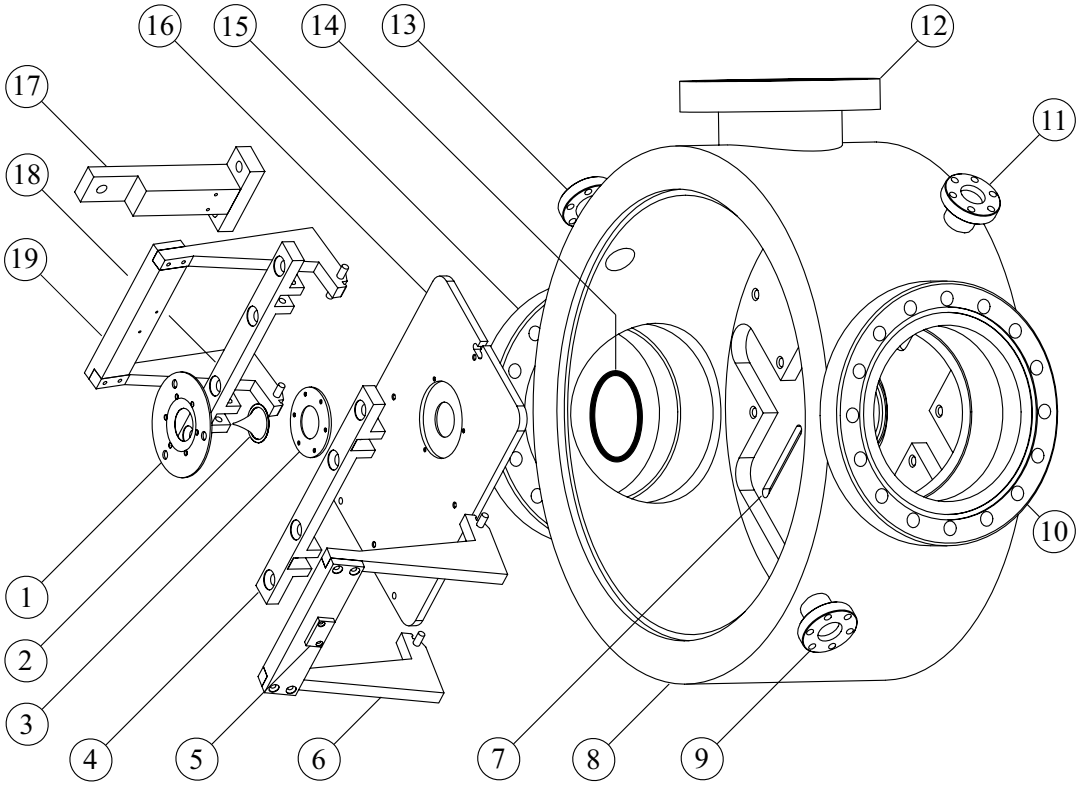

Figure 4.3: Explosion drawing of the home-built gate valve integrated in a CF 250 flange. The individual parts are: (1) upper skimmer mount, (2) skimmer, (3) lower skimmer mount, (4, 18) shaft holders, (5) hardened steel plate, (6, 19) lever arms, (7) slots for alignment pins, (8) chamber flange (CF 250), (9, 11, 13) CF 16 flanges, (10, 15) CF 100 flanges, (12) CF 63 flange, (14) Viton O-ring, (16) sledge, and (17) linear motion feedthrough guide.

sure is measured using a compact cold cathode gauge (Pfeiffer Vacuum, IKR 270).

4.3 Source

4.3.1 Benzonitrile

The molecular beam of benzonitrile (C_7H_5N) is produced using a pulsed solenoid nozzle (General Valve, Series 99) with a 0.8 mm orifice, which is operated at 27° C. A gas system allows for quick changes of the seed gases. For instance, for first measurements it is convenient to seed benzonitrile in argon. This yields, due to the smaller mass of argon compared to xenon, a higher beam velocity, and therefore the free-flight intensity is increased. For deceleration measurements, benzonitrile is seeded in xenon because of the lower initial velocity of the molecular beam for the heavier seed gas. In most measurements presented in this thesis, benzonitrile is seeded in xenon at a stagnation pressure of 0.7 bar. The gas flows through a bubbler with some milliliters of benzonitrile (Fluka, $\geq$ 99 % purity), which is a clear liquid and has a vapor pressure of 1.33 mbar at room temperature. The connections between the bubbler and the nozzle are all stainless steel tubings with an inner diameter of 4 mm and a total length of about a meter. The nozzle is operated with a home-built pulsed nozzle driver (Fritz Haber Institute (FHI) electronic laboratory (Elab) 3076), which provides an electronic pulse for the nozzle with a voltage of 300 V. With potentiometer settings between 0 and 10, the time widths are adjusted between 60 μs and 300 μs. The opening time of the nozzle depends on this electronic trigger pulse and is typically between 140 μs and 200 μs (see figure 4.4). The nozzle is mounted on a translation feedthrough, which allows for an adjustment in all three spatial directions. The rotational temperature for benzonitrile seeded in xenon is typically 3.0 K (see chapter 6.2). The molecular packets in this supersonic jet have a mean velocity of approximately 320 m/s and a velocity spread at FWHM of about 10 %. 27 mm downstream from the nozzle, the molecules pass the skimmer and enter the differentially pumped decelerator chamber.

Figure 4.4 shows the time-of-flight distributions of benzonitrile molecules seeded in 0.7 bar of xenon, which are detected in the source chamber via laser-induced fluorescence (LIF) at 274 nm (see section 4.6). In order to perform the measurements in figure 4.4, the distance between the nozzle and the skimmer is increased to 42 mm, and the molecules are detected 24 mm behind the nozzle. The dependence of the signal intensity and signal width on the potentiometer setting of the pulse nozzle driver are studied, in order to obtain an intense signal

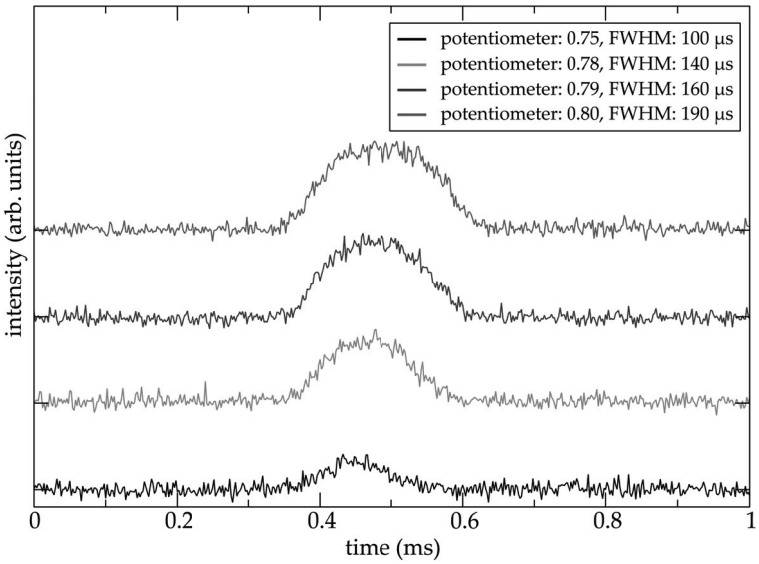

Figure 4.4: Laser-induced fluorescence signal of benzonitrile molecules measured in the source chamber using different potentiometer settings for the opening time of the nozzle. The time is given relative to the electronic trigger signal for the pulsed nozzle driver. From all curves the background is subtracted, and they are offset for clarity.

and a narrow width of the molecular packet. This is achieved here for a potentiometer setting of 0.78 or 0.79, where the FWHM at the detection position is 140 μs or 160 μs, respectively. It should be noted that the tensions of the springs inside the nozzle change during operation and therefore, the potentiometer setting has to be adjusted after some days. Typically, this adjustment is performed by optimizing the signal intensity and width of the TOF distributions detected behind the decelerator. The times are related to the electronic trigger time for the pulse nozzle driver. The delay between the electronic trigger pulse and the mechanical opening of the nozzle is about 0.40 ms, depending on the nozzle voltage and potentiometer setting.

Alternatively, the produced molecules can be detected in the source chamber, using a quadrupole mass spectrometer (Pfeiffer Vacuum, Prisma QME200). Via the mass spectrum, the quality of the molecular beam in the source chamber is monitored, because for most experiments the LIF detection is only performed in the deceleration chamber. A mass spectrum of benzonitrile seeded in xenon under normal operation conditions is given in figure 4.5. The features at about 132 u (66 u) correspond to the different isotopes of singly (doubly) ionized xenon. Benzonitrile is detected at 103 u, and some of its fragments occur around 50 u and 76 u.

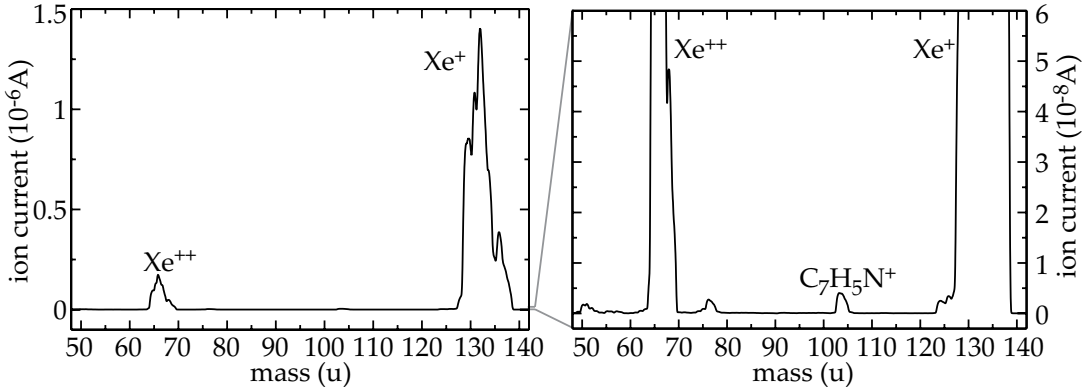

Figure 4.5: The graphs show the mass spectrum of benzonitrile seeded in xenon measured in the source chamber. The right-hand graph is an expanded view of the left-hand graph such that the mass signal of benzonitrile at 103 u is clearly visible. The peaks at 50 u and 76 u are due to fragments of benzonitrile.

4.3.2 OH

The production of a pulsed beam of OH radicals is described in detail elsewhere [128, 153]. The setup and geometry of the gas system is the same as described above. In brief, xenon at a pressure of 3 bar flows through a bubbler with liquid HNO_3. The pulsed nozzle is modified such that a 6 mm long quartz capillary (Suprasil 1) with an inner diameter of 1 mm is directly mounted to the orifice of the nozzle. OH radicals are produced by photodissociation of gaseous HNO_3. The output of an ArF excimer laser (Neweks, PSX-501-2), operated at 193 nm and providing a pulse energy of 4 mJ within 5 ns long pulses, is focused onto the end of the capillary using a cylindrical lens with a focal length of 50 cm. The molecular packets of OH radicals have mean velocities of about 360 m/s and a velocity spread of approximately 25 %. Due to the production process, the initial position is well defined to approximately 2 mm, which corresponds to an initial time spread of about 6 μs at a velocity of 360 m/s. 20 mm downstream from the nozzle, the OH molecules pass the skimmer and enter the differentially pumped decelerator chamber.

4.4 Alternating-gradient decelerator

In figure 4.6(a), a sketch of the electrode pattern and in figure 4.6(b) a photo of the AG decelerator are shown. The decelerator consists of 27 electrode stages arranged along the molecular beam axis. This axis is referred to as the longitudinal direction or the z-axis. The AG decelerator has a total length of 533 mm from the beginning of the first electrode stage to the end of the last electrode

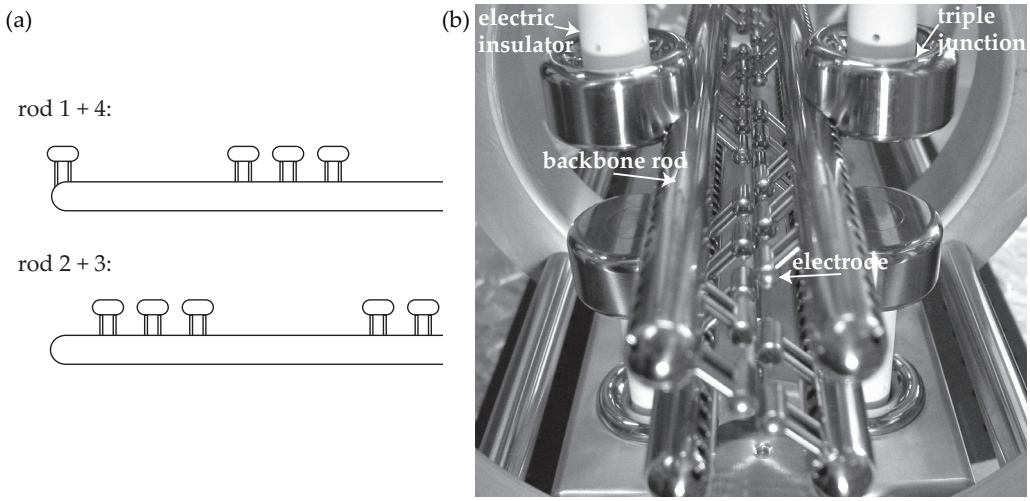

Figure 4.6: (a) Sketch of the electrode pattern at the beginning of the decelerator for the four backbone rods. (b) Photo of the rear end of the alternating-gradient decelerator with electrode pairs, electric insulators, backbone rods, and triple junctions.

stage. The first AG lens starts 37 mm behind the tip of the skimmer. The precise alignment of the electrodes is of great importance for the performance of the AG decelerator. Therefore, the alignment and mounting of the decelerator is done such that imperfections due to the machining process of all individual parts of the decelerator can in principle be compensated for.

Several steps are needed for the setup of the decelerator: First, the alignment pins which connect the electrodes with the backbone rods are pressed into the electrodes. Then, the electrodes with the alignment pins are pressed into the backbone rods and are aligned to the same height on a flat marble plate. The backbone rods with the electrodes are mounted on the electric insulators, and all parts are fixed and adjusted in an outer frame. Finally, the decelerator is mounted in the vacuum chamber on two aluminum feet, which are adjusted using micrometer screws. The alignment of the decelerator to the molecular beam axis is facilitated using a theodolite.

The stainless steel electrodes are 13.0 mm long, have a diameter of 6.0 mm, and spherical end caps with a radius of 3.0 mm. The highly-polished electrodes are produced by Schmidt & Lorentz with a measured root mean square surface roughness value of about 30 nm. The low roughness is needed to withstand the high electric fields. The electrodes have two blind holes with diameters of 2.99 mm at a center-to-center distance of 5 mm. Into these holes two slotted alignment pins with a diameter of 3.0 mm and a length of 24 mm are pressed

using a toggle press. Afterwards, the toggle press is used to press the electrodes with the alignment pins into the stainless steel backbone rods, which have a similar regular pattern of 2.99 mm diameter boreholes every 5 mm over the whole length of the backbone rod. The height of the electrode surfaces compared to the rods is controlled using polished spacers. The four backbone rods have a diameter of 14 mm, a length of 538 mm, and spherical end caps with a radius of 7 mm. Successive electrodes are placed at center-to-center distances of 20 mm along the backbone rod.

The $(FO)\left((DO)^3(FO)^3\right)^4(DO)^2$ grid for the focusing (and defocusing) of molecules discussed in chapter 3 is implemented by the arrangement of the electrodes in the rods, as sketched in figure 4.6(a). At the entrance of the decelerator, a single electrode is pressed in the first rod. This is followed by a 67 mm gap, leaving out three electrodes. Behind the gap, three successive electrodes are pressed in. For the second backbone rod, three successive electrodes are pressed in such that they fit in this gap. This pattern of three electrodes and a gap for the three rotated electrodes is repeated along the whole rod. The third and fourth backbone rod have the same electrode pattern as the second and first rod, respectively. The second rod is mounted rotated by 90° relative to the first rod, and every two opposing rods exhibit the same pattern. After the mounting of the rods, the two opposing surfaces of the electrodes of a stage are 2 mm apart. By starting the electrode pattern of three successive AG lenses with a single one, the transverse acceptance of the AG decelerator is increased.

After all electrodes are pressed in the rods, the alignment of the electrode top surfaces is controlled on a flat marble plate. Using stainless steel foils with different thicknesses between 10 μm and 100 μm, it can be checked whether all electrodes have the same height while lying on the marble plate. If one electrode is higher than a neighboring electrode, it will be pressed further in, using a smaller spacer at the toggle press. If one electrode is already pressed in too far, it will be taken out again and will be pressed into the rod using a larger spacer. This process is iterated until all electrodes are aligned relative to each other on the marble plate. The height of the electrodes relative to the rod varies, because the rod is slightly bent due to the machining process. Even if the height of the electrodes can be adjusted quite precisely, the electrodes may be tilted in the transverse direction, which is reduced as much as possible by tilting the electrodes back with a small screw clamp. After the alignment of the electrodes, two mounts are pressed in each rod from the side opposite to the electrodes. The stainless steel mounts have a special shape such that the alumina electric insulators are inserted into them. This highly reduces the local electric field strength at the triple junctions, which are the boundaries between

electric conducting materials (mounts of the electrodes), electric insulating materials (ceramics), and vacuum. This shielding of the triple junctions largely reduces the probability of electric surface flashovers [154]. The other side of the insulators is fixed on an aluminum plate using another stainless steel mount. The four subunits consisting of the electrodes, rods, insulators, mounts, and the plate are then fixed onto the outer frame. Using micrometer screws transverse to the molecular beam axis and special bronze alignment tools, these subunits are adjusted such that every two opposite top surfaces of the electrodes of one stage are 2 mm apart. For the two upper subunits, stainless steel foils with different thicknesses are put between the frame and the subunits to adjust the height properly. In the transverse direction, the gaps between the electrodes vary between 1.95 and 2.05 mm. Furthermore, parallel to the molecular beam axis, the gaps between two successive electrodes of different rods are adjusted to be 7 mm, using micrometer screws. After the alignment and fixing, the longitudinal distances between two successive electrodes vary between 6.95 and 7.15 mm. These deviations are mainly due to discrepancies of the distances of the boreholes in the backbone rods, into which the electrodes are pressed, and variations of the length of the single electrodes between 12.9 and 13.0 mm.

After the mounting and alignment of the AG decelerator module itself, it has to be positioned inside the vacuum chamber. For that purpose, two aluminum feet of the decelerator stand on two bronze baseplates. These are mounted onto the stainless steel tabs in the lower tubes of the CF 100 flanges of the deceleration chamber close to the 230 l/s turbo drag pump, as indicated in figure 4.2(a). Using alignment tools and micrometer screws, both feet are levelled and the AG decelerator is screwed onto the feet. Two plexiglas disks with a precisely centered 0.8 mm diameter borehole are fixed on the knife edge of the CF 250 flanges at both ends of the vacuum chamber to define the molecular beam axis. The theodolite is aligned to this axis, and the skimmer as well. Using two bronze alignment tools with a centered 0.8 mm borehole, which can directly be positioned on any electrode stage, the AG decelerator is also aligned to this axis. In the alignment process, the feet of the decelerator are adjusted using micrometer screws. Furthermore, the AG decelerator is aligned to be centered in the vacuum chamber in the longitudinal direction. After the alignment procedure, the feet of the AG decelerator are fixed with screws to the bronze baseplates, which are fixed to the tabs in the lower CF 100 tubes, and the micrometer screws are removed. The theodolite facilitates to also align the nozzle to this axis. Later, also the LIF detection zone and the light baffles are aligned to the molecular beam axis by means of helium neon (HeNe) lasers.

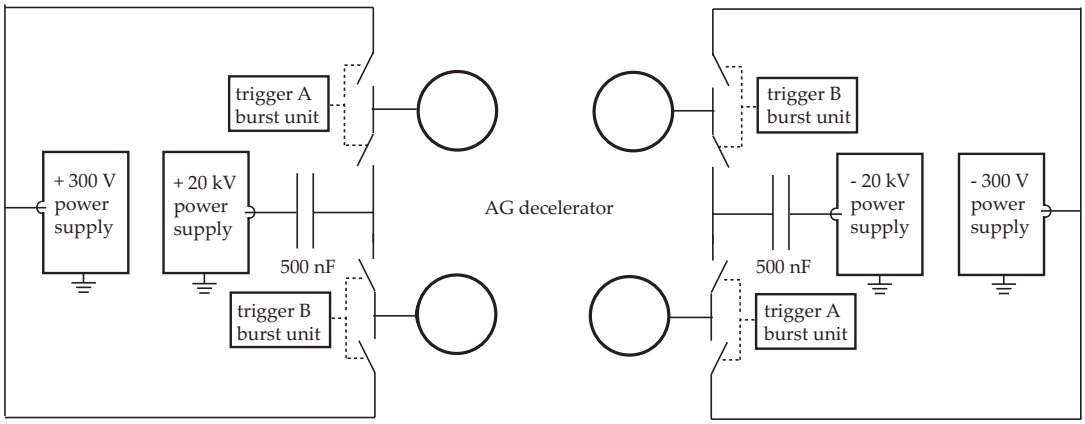

Figure 4.7: Sketch of the electronics setup that is used for the alternating-gradient (AG) decelerator. The left-hand side represents the positive high voltage assembly, the right-hand side the negative high voltage assembly. The four circles in the middle represent the four backbone rods of the AG decelerator. The switches are triggered by the burst unit and are switched between ± 15 kV and a bias voltage. All boxes are grounded.

4.5 Electronics

A sketch of the electronics setup is shown in figure 4.7. Each backbone rod of the AG decelerator is connected via 30 kV electric feedthroughs (Hositrad 16729-03-CF) to a fast 20 kV push-pull switch (Behlke Elektronik, HTS-201-03-GSM). Two of these switches operate at a positive high voltage, the other two operate at a negative high voltage. Two switches that operate at the same polarity are built together with accessory devices in a radiation shielded box (FHI Elab 3499.1, 3499.2). Two diagonally opposing rods share a trigger pulse, which is provided by a home-built burst unit (FHI Elab 3388) with a time resolution of 10 ns. The burst unit itself, as well as the nozzle, the excimer laser, and the data acquisition, are triggered by a home-built delay generator (FHI Elab 3294.1). Both units are controlled using the program package KouDA [155]. The high voltages for the switches are provided by two 20 kV power supplies (FuG, HCK 400-20000, 40mA), which each load a 500 nF capacitor (FHI Elab 3499). The capacitors minimize the voltage drop during the length of the applied time sequence to a few percent. For a single switching sequence, high voltages are typically switched on 13 or 14 times for about 3–20 μs each. Due to the different switching scheme for molecules in lfs states (see chapter 3.5 and 7), the high voltages are switched twice as often for the experiments on OH in its lfs state. The typical length of a burst is approximately 1.7 ms, and the exact parameters depend on the calculated switching sequence. The rise and drop time of the high

voltage is about 300 ns, which is defined by the accessory electronic devices of the switches, and is short enough that the motion of the molecules during the rise time can be neglected, but long enough to avoid damage of the switches. Time sequences are applied up to 40 times per second. The switches of same polarity share a single 20 kV high voltage power supply and 500 nF capacitor. Instead of switching between a high voltage and ground, the switches can alternatively be operated to switch between a high voltage and a bias voltage. This bias voltage of up to ±300 V has the same polarity as the high voltage and is provided by 300 V laboratory power supplies (Delta, ES0300-0.45). The bias voltage is applied for the suppression of transitions at low electric field strengths (see chapters 6 and 7). Because of the fast switching times, the high voltage switches as well as the electric feedthroughs and cables are radiation-shielded.

Before switched high voltages are applied to the AG decelerator, it is exposed to substantially higher DC voltages to reduce the risk of electric flashovers. In this procedure called "current conditioning" [154], first a relatively small DC high voltage of, for instance, ±5 kV is applied to the two diagonally opposing backbone rods of the AG decelerator. The two other rods are grounded. Meanwhile, for each polarity the currents, which are limited by two 100 MΩ resistors, are measured with digital multimeters (Fluke 87 V). If both currents are smaller than 50 nA for at least ten minutes, the high voltage will be increased by 0.5 or 1 kV. Otherwise, the high voltage is kept for another ten minutes. This procedure is iterated until DC high voltages of ±19 kV can be applied to the decelerator, corresponding to a maximum electric field of 180.5 kV/cm on the molecular beam axis and 210.0 kV/cm on the electrode surfaces. To avoid electric flashovers, the maximum DC voltage is chosen more than 25 % larger than the maximum switched high voltage used in the measurements [154]. This procedure has to be repeated for the other two backbone rods and, furthermore, every time after the decelerator has been exposed to air. During the AG focusing and deceleration experiments, voltages are switched between ±15 kV and ground or a bias voltage, creating a maximum electric field of 142.5 kV/cm on the molecular beam axis.

4.6 Detection

4.6.1 Laser system

A scheme of the laser system is shown in figure 4.8. It consists of an argon ion laser (Coherent Innova Sabre, 15 W) which pumps a ring dye laser (Coherent RDL899-21). The light exiting the dye laser is frequency-doubled using a beta

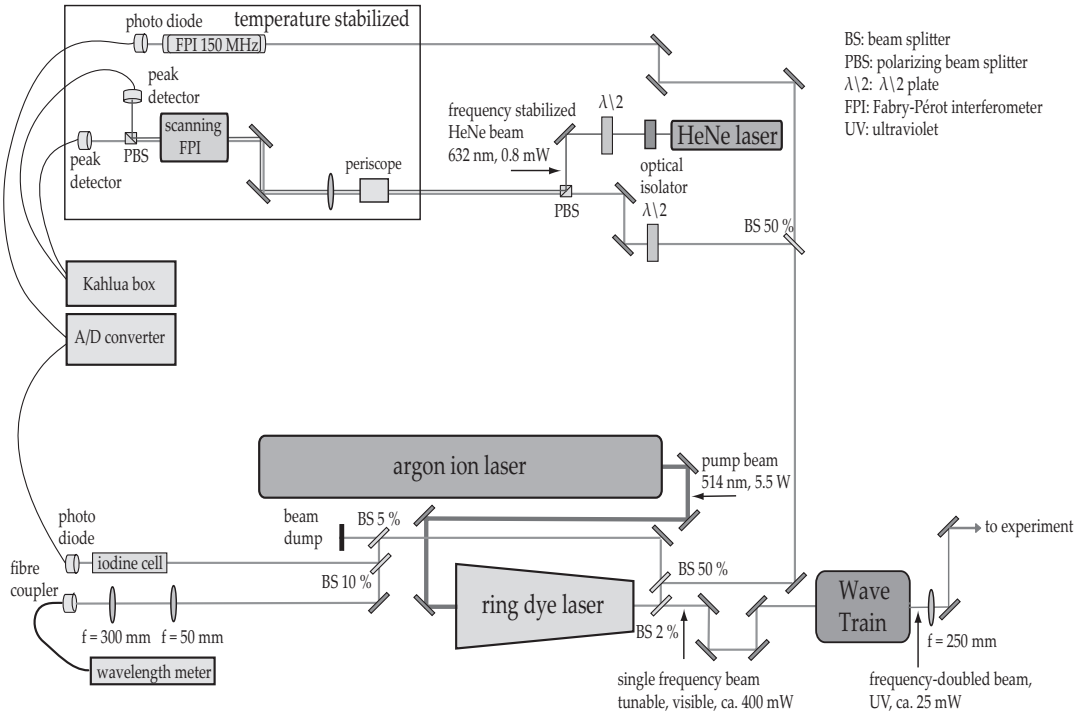

Figure 4.8: Scheme of the laser system and the calibration and frequency stabilization devices. The specified values for the laser powers are typical values. See text for details.

barium borate (BBO) crystal in the focus of an enhancement cavity (Spectra Physics, LAS WaveTrain). A fraction of the laser light is branched off for calibration and frequency stabilization devices. The calibration devices include an iodine cell, a wavelength meter, and a Fabry-Pérot interferometer (FPI). In addition, the frequency of the ring dye laser is externally stabilized relative to a frequency stabilized HeNe laser.

In more detail, the laser system is placed on an actively stabilized optical table. A laminar flow box blows filtered and temperature-controlled air on the laser table, leading to a temperature of $(22.2 \pm 0.3)^\circ$ C after a warming up period for the argon ion laser of about one hour. The argon ion laser is typically operated to provide 5–6.5 W at 514 nm. It pumps a continuous, tunable, and narrow-linewidth ring dye laser. The laser dye Rhodamine 110 (Radiant Dyes) has a lifetime of 250 hours/W and can be tuned between 535 nm and 570 nm. The power decrease during the lifetime period is partly compensated by an increase of the power of the argon ion laser from 5 W up to 6.5 W. 300–550 mW laser light is produced at the desired wavelength of 548 nm for the detection

of benzonitrile and 564 nm for the detection of OH. The dye laser allows to scan a frequency range of up to 30 GHz without mode hops. Some modifications of the ring dye laser have been implemented for a more stable and more reliable operation: The dye nozzle has been replaced by a low pressure special nozzle (Radiant Dyes, RDSN02). Furthermore, a different dye circulator (Radiant Dyes, RD10000W) and an additional high pressure air cushion (Radiant Dyes, RDAC10) have been used. The air cushion is filled with 5 bar of argon to absorb vibrations of the dye circulator. In addition, the servo motor driver has been replaced by a home-built one (FHI Elab 3774), which drives the master cavity of the ring dye laser more stably. It is used for slow frequency scans when molecular spectra are recorded. For fast scans (for instance during the alignment of the ring dye laser), one can switch back to the internal servo motor drive electronics. A plexiglas cover which allows for all optical adjustments protects the ring dye laser. A nitrogen flow helps to keep the optical elements clean from dust particles.

Behind the ring dye laser, the laser light is split into a main path containing 98 % of the laser intensity and a side path for the calibration and frequency stabilization devices. The laser light of the main path is coupled into the WaveTrain resonator, which is actively stabilized using the Pound-Drever-Hall method [156]. The main component of the WaveTrain is a BBO crystal, a non-linear crystal, in which the second harmonic is generated such that the laser light exiting the ring dye laser is frequency doubled. The resonator is a ring cavity and consists of the BBO crystal, two resonator mirrors, and a prism, which is mounted on a piezoelectric transducer. The resonator is tuned by translating the prism. The advantage of this resonator design is that the beam path is unaffected from the translation of the prism. If the phase and mode matching conditions are fulfilled, the injected power is up to a hundredfold enhanced inside the resonator and about 15–30 mW of frequency-doubled light is produced. The ultraviolet (UV) light is transported via two large periscopes to the decelerator setup in the neighboring laboratory. The beam path is about 15 m long.

At the molecular beam machine, the UV light is guided via a second periscope and several mirrors through the detection chamber, where the LIF detection is performed (see section 4.6.2). The UV light exiting the vacuum chamber can be stabilized in its position, using an active beam align detector (MRC). It consists of a quadrant diode detector which detects the UV light and a piezoelectric controlled UV mirror. The signal on the detector is fed back to this mirror, which is used as the first mirror of the periscope next to the laser system. Using the active beam alignment system, the center of the UV light beam can be positioned within about 0.1 mm.

The laser light that is branched off behind the ring dye laser is used for calibration and frequency stabilization devices. A part of the light is coupled into an optical fiber and transmitted to a wavelength meter (High Finesse, WS-6), with which the absolute frequency of the laser light is quickly determined with an accuracy of ±700 MHz. A home-built iodine cell [157] allows to determine the absolute frequency with an accuracy of about 200 MHz by comparison with the known iodine absorption spectrum [158]. In a box, stabilized at a temperature of $(27.00 \pm 0.02)^\circ$ C, a home-built confocal FPI is placed. The mirrors of this confocal FPI are mounted on a 0.5 m long Zerodur rod (Schott, length extension class 1), which length extension is specified to be less than $\pm 5 \cdot 10^{-8}$ m/K at room temperature. The free spectral range of the confocal FPI at room temperature has been determined to (149.94867 ± 0.00022) MHz by several iodine spectra measurements in a well defined frequency range [157]. Here, the confocal FPI is used at 27° C, such that the error of the free spectral range is about 50 % increased. The photodiode signals behind the FPI and the iodine cell are recorded using a 12 bit A/D converter and acquired with KouDA. In frequency scans of the molecular spectra, the FPI signal is recorded in order to provide the relative frequency calibration for these scans.

Using the internal frequency stabilization of the ring dye laser only, frequency shifts of about 5 MHz/min, probably due to temperature fluctuations, have been observed. This stability is not sufficient for the experiments presented in this thesis, because of the natural linewidth of the transitions for benzonitrile of 8 MHz [159]. Hence, the frequency of the ring dye laser is externally stabilized using a HeNe (Sios SL-03, 0.8 mW) laser, which is frequency-stabilized on orthogonally polarized longitudinal modes. Using a scanning FPI (Toptica, FPI 100-0500-2.0) the continuous tunable ring dye laser can be frequency-stabilized relative to the HeNe laser [160, 161]. Behind the HeNe laser an optical isolator with an isolation of 44 dB (Laser 2000 IO-2D-633-VLP) is placed in order to protect the laser from feedback of back-reflected laser light. The HeNe laser beam and a fraction of the dye laser beam are linearly polarized at a 90° angle with $\lambda/2$ plates. The beams are superimposed using polarization beam splitter cubes, and coupled into a scanning FPI with a free spectral range of 1.0 GHz. The scanning FPI is surrounded by a temperature- and pressure-isolated box. Behind the piezoelectric driven scanning FPI, the two laser beams are separated with a polarizing beam splitter cube and detected with home-built peak detectors.

The voltage ramp which drives the scanning FPI is generated by a industrial computer running KWorks (MEN mikro elektronik, Kahlua Box) and home-built

software and amplified with a home-built high voltage amplifier (FHI Elab 3399). The peak detectors detect transmission peaks for both lasers, and the time between the start of the voltage ramp and the detection of the transmission peak is measured by a counter (MEN mikro elektronik, M97). From the difference between the count number of the ring dye laser transmission peak and the count number of the HeNe transmission peak, a feedback signal is generated. This signal is fed back to the servo motor driver of the master cavity of the ring dye laser, such that the difference between the two transmission peaks is kept constant. The parameters of the laser stabilization are controlled by KouDA. Furthermore, the software allows for frequency scans in which the count number of the frequency-stabilized ring dye laser is scanned relative to the count number of the HeNe laser. One count in a scan corresponds to a frequency shift in the UV of approximately (0.22 ± 0.01) MHz. The frequency in the scans is calibrated more accurately by recording the transmission peaks of the confocal 0.5 m long 150 MHz FPI and linearizing the spectra to the transmission peaks. KouDA also allows to record scans over a larger range than the free spectral range of the scanning FPI of 1 GHz. With the frequency stabilization setup, the mean frequency of the dye laser is stable to about ± 1 MHz/hour.

4.6.2 Laser-induced fluorescence detection

The UV beam exiting the WaveTrain is not parallel, but divergent and astigmatic and does not have a Gaussian beam profile, as desired for the LIF detection. Because of the long beam path from the laser table to the AG decelerator setup of about 15 m, the UV beam diverges, and some less intense side modes of the beam profile become visible. The divergence of the UV beam can be almost compensated, using a UV lens with a focal length of 250 mm behind the WaveTrain, such that the size of the UV beam is smaller than the diameter of the mirrors (25 mm) everywhere along the beam path. Directly behind the lower mirror of the periscope, near the molecular beam setup, the diameter of the UV beam is decreased using a telescope, as is shown in the scheme of the optical setup for the LIF detection in figure 4.9. The telescope consists of two lenses with focal lengths of 500 mm and 75 mm, respectively. The side modes of the UV beam are blocked by the first pinhole behind the telescope, where only the central part with a diameter of about 2 mm passes through. The later pinholes are adjusted such that stray light inside the vacuum chamber is minimized. Because of the spatial filtering of the central part of the laser light and the long path length, the power of the UV light transmitted through the vacuum chamber is decreased by about a factor three compared to the power at the laser table. 5–10 mW UV light with a beam diameter of about 1 mm is available at the interaction point with the molecular beam, which is adequate for the LIF detection. The UV

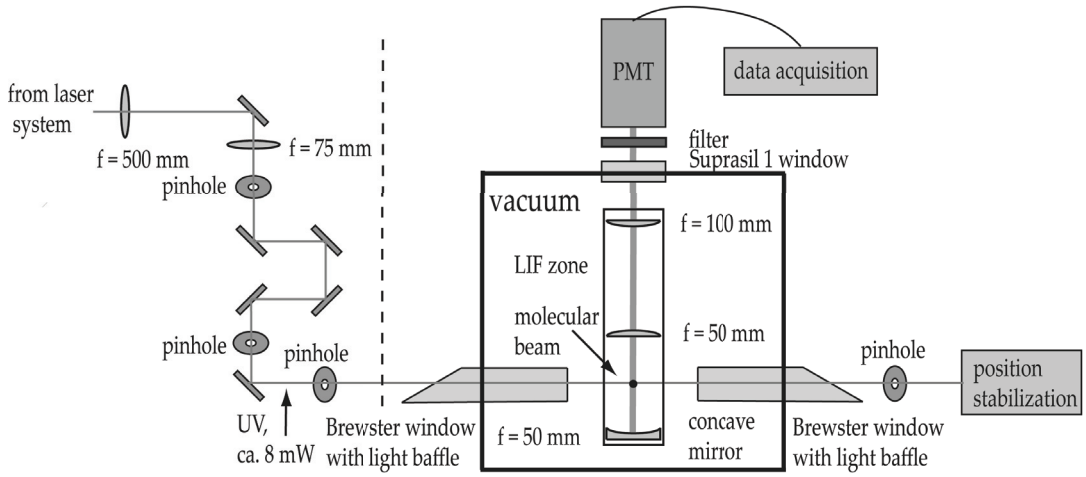

Figure 4.9: Scheme of the optical setup at the molecular beam apparatus for laser-induced fluorescence (LIF) detection. The LIF of the molecules is collected with a LIF zone and detected after filtering using a photomultiplier tube (PMT).

beam enters the vacuum chamber via a Brewster window, which is a Suprasil window mounted under the Brewster angle to allow for a full transmission of the perpendicularly polarized light. The Brewster windows are mounted on rotatable flanges to adjust the Brewster angle relative to the polarization plane of the UV light. Inside the Brewster windows, light baffles are mounted for the reduction of stray light. The light baffles consist of a blackened tube with blackened pinholes and skimmers each with a 5 mm diameter opening, through which the UV beam enters. After the detection of the molecules, the UV beam exits the vacuum chamber through a second Brewster window with a light baffle.

At the interaction point of UV beam and molecular beam in the vacuum chamber, the molecules are electronically excited and their LIF photons are detected using a lens system and a photomultiplier tube (PMT, Electron Tubes Limited, B2F/RFT). The PMT is operated at 1700 V provided by a high voltage power supply (Ortec, 0–3 kV). The LIF zone, which collects the fluorescence, consists of a concave mirror with a focal length $f = 50$ mm and two uncoated Suprasil1 plan-convex lenses with a diameter of 50 mm and $f = 50$ mm and $f = 100$ mm, respectively. The lenses are arranged, such that the LIF of the molecules is imaged onto the PMT. The concave mirror reflects the LIF back to the interaction point with the molecular beam such that the LIF in the direction of the mirror is imaged onto the PMT as well. The LIF signal exits the vacuum chamber through a Suprasil1 window on a CF 40 flange. For the reduction of stray light, a band pass filter (Schott UG 11, 2 mm thick) which filters visible

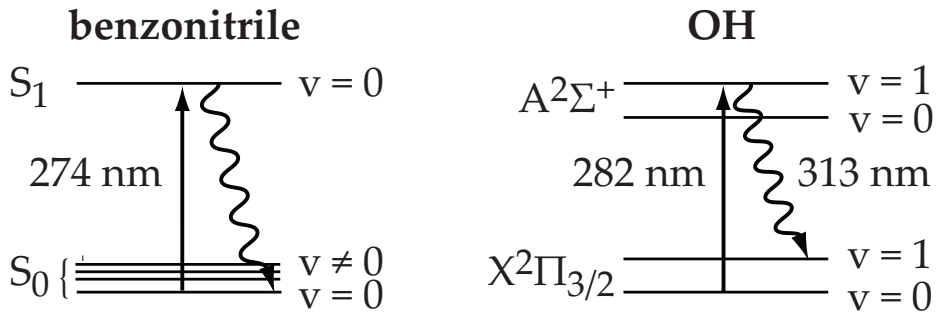

Figure 4.10: Scheme of the laser-induced fluorescence detection for benzonitrile (left) and OH (right). See text for details.

light and a spatial filter with a circular opening of 7 mm are placed in front of the PMT.

The LIF detection schemes for both benzonitrile and OH are shown in figure 4.10. OH is probed via the $A^2\Sigma^+, v' = 1 \leftarrow X^2\Pi_{3/2}, v'' = 0$ transition at 282 nm. From the $A^2\Sigma^+, v = 1$ state, the population decays mainly to the $X^2\Pi, v = 1$ state, resulting in a off-resonant fluorescence at 313 nm [162]. The fluorescence is filtered from the excitation wavelength with two edge filters (Laser Components, LC-300ALP-50). Benzonitrile molecules are probed via the $S_1, v' = 0 \leftarrow S_0, v'' = 0$ transition at 274 nm [163, 164]. The largest fraction of the fluorescence of benzonitrile is resonant. But some dispersed fluorescence occurs at wavelengths between 277–286 nm when the population decays to several excited vibrational modes of the S_0 state [165, 166]. This is so close to the excitation wavelength at 274 nm, that edge filters are not available. Therefore, special care has to be taken to reduce the UV stray light during the detection.

The alignment of the light baffles and the LIF zone is done using two HeNe lasers. One HeNe laser is aligned to the molecular beam axis that is defined by the skimmer and the bronze alignment tools with a 0.8 mm borehole, which is placed on the electrodes of the AG decelerator. The other HeNe laser is aligned to the center of the light baffles. Then the light baffles are aligned to be horizontal, parallel, and on the same height as the molecular beam axis such that the two laser beams cross. Furthermore, the distances of the lenses of the LIF zone are arranged such that the stray light from a needle in the crossing of the two HeNe beams, is imaged optimally onto the PMT.

The detection path can easily be changed to allow for LIF detection in the source chamber. In that case, the UV light is aligned through two Brewster

windows, and the LIF is detected using a LIF zone with a single $f = 75$ mm lens. The same filters and the PMT are mounted above the LIF zone on the source chamber.

4.7 Data acquisition

The PMT signal is amplified using an active 50 Ω pre-amplifier. The signal is discriminated if the negative signal is below an adjustable threshold of typically −40 mV. The data acquisition system utilizes an Acquiris digitizer card (DC 440, 100 MHz) with a time resolution of 2.5 ns in a cPCI crate, which is read out with KouDA. Time-resolved photon counting of the LIF signal is implemented in rtKouDA [155] on VxWorks, which communicates over the network with KouDA on the laboratory Linux computer. Photon counting is used to reduce the noise for low-intensity measurements and to increase the time accuracy compared to an analogue detection. In most measurements, the signal is binned in time intervals of 2 μs and is recorded over 1.5–2.0 ms. A 12 bit A/D converter is used to record the signals of the laser system, namely the laser power output of the ring dye laser, the photo diode signal of the 150 MHz FPI, and the photo diode signal of the iodine cell.

In KouDA, a gate defines a time interval, for which the photon-counting intensity is evaluated. Signals are defined as operations on gates or data from the 12 bit A/D converter. In the scans, the signal in these gates as well as the signals of the 12 bit A/D converter are recorded as function of the ring dye laser frequency. The data acquisition of the experiments with benzonitrile is performed at 40 Hz. Due to the limits of the excimer laser used for the production of OH, the data for OH are recorded at a repetition rate of 20 Hz.

4.8 Outlook

Currently, the AG decelerator setup is extended from one deceleration module to two deceleration modules, and preparations for the extension to three modules are in progress. This extension will allow to decelerate the molecules to much lower velocities and to spatially separate the decelerated packet from the original beam pulse. Because of the modular design of the setup, this extension is easily implemented. In between the deceleration and detection chamber, another deceleration chamber with the new deceleration module is mounted. Special care has to be taken for the alignment of the two decelerator modules on the

molecular beam axis. From the analysis of the deceleration measurements and trajectory simulations for one module, a higher acceptance for the deceleration of molecules in hfs states is expected for an electrode pattern with two successive electrodes in a row instead of three (see chapter 6.7). Therefore, the old module with the $(FO)^3(DO)^3$ grid is replaced by two new modules with a $(FO)^2(DO)^2$ grid. The high voltage switches and the whole electronic setup are designed and tested to operate for the extended setup as well. First measurements on the deceleration of benzonitrile in the extended setup are underway.

A further improvement would be a more intense and shorter molecular beam pulse of benzonitrile, as this would result in a higher signal intensity for the decelerated molecules. This could possibly be achieved by replacing the General Valve by an Even-Lavie valve [167]. Another advancement could be upgrading the data acquisition system to operate at a repetition rate of about 100 Hz, which is about the maximum repetition rate for the other components of the experimental setup for the deceleration of benzonitrile.

Chapter 5

Fourier-transform microwave spectroscopy of benzonitrile

5.1 Introduction

For a detailed analysis of the AG focusing and deceleration experiments presented in chapter 6, a precise knowledge of the dipole moment of benzonitrile is necessary. Due to the C_{2v} symmetry of benzonitrile, only a non-zero μ_a component of the dipole moment exists. However, the value of the dipole moment of benzonitrile has been a matter of debate. To our knowledge, only two independent and incompatible values of the dipole moment of benzonitrile in its electronic ground state had been published so far: From microwave Stark effect measurements, a dipole moment of 4.14(5) D was deduced [168], and a similar value based on the same measurements (4.18(8) D) is listed in the CRC Handbook of Chemistry and Physics [141]. Recently, a different value of 4.48(1) D was determined from Stark effect measurements of the rotationally resolved laser-induced fluorescence spectrum [159]. Therefore, a precise experimental determination of the dipole moment using Fourier-transform microwave (FTMW) spectroscopy in homogeneous electric fields is presented in this chapter. The following chapter is based on reference 115.

5.2 Experimental setup

The technique of FTMW spectrometry is described in detail in reference 169. In brief, a pulsed supersonic jet is expanded into a microwave cavity. A microwave pulse with a certain duration is applied to the cavity. The spectral width of this microwave pulse covers a band of frequencies which can include frequencies resonant to rotational transitions of the molecule. While the microwave pulse

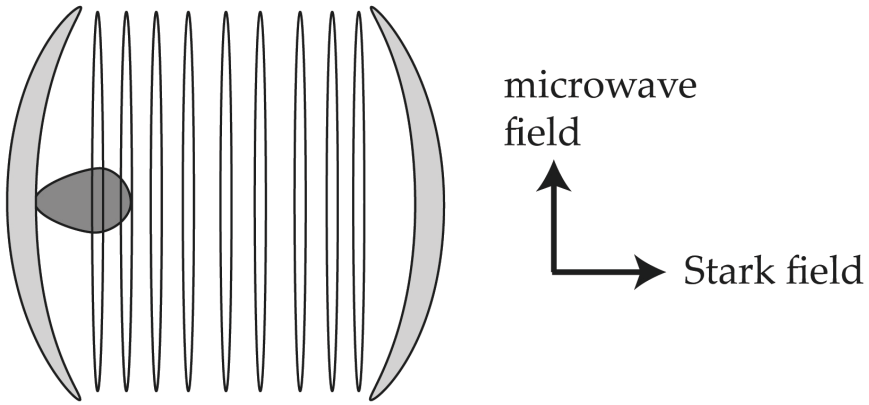

Figure 5.1: Sketch of the Fourier-transform microwave spectrometer in Hannover. The supersonic jet is pulsed into the resonator, which consists of two spherical mirrors. For Stark effect measurements a high potential difference of up to 12 kV is applied between the right mirror and the left mirror, which is grounded. The circular electrodes between the reflectors are kept at a potential decreasing from right to left, in order to homogenize the electric field. See text for details.

decreases, the now polarized molecular ensemble emits radiation at their resonance frequencies. The free induction decay is detected and Fourier-transformed to obtain the microwave spectrum.

The measurements have been performed using the Coaxially Oriented Beam-Resonator Arrangement (COBRA) FTMW spectrometer in Hannover. The experimental setup is described in detail elsewhere [170, 171], and a sketch of the setup is given in figure 5.1. In brief, benzonitrile (Fluka, $\geq 99\,\%$ purity) is co-expanded in 3.5 bar of neon at a temperature of 300 K through a pulsed nozzle (General Valve, Series 9) with a 0.8 mm orifice. The supersonic jet is pulsed coaxially into a broadband (2–26.5 GHz) microwave resonator [172]. The microwave resonator consists of two Fabry-Pérot type arranged spherical aluminum mirrors with a diameter of 63 cm and approximately the same distance. In comparison with previous setups [169, 173, 174], it has been specially developed to provide high sensitivity and resolution at low frequencies down to 2 GHz [175]. The microwave pulse with a duration of 0.5 μs is coupled to the resonator, using an antenna. The distance of the mirrors is tuned to select the frequency of the standing wave.

Homogeneous electric fields for the Stark shift measurements are provided by the Coaxially Aligned Electrodes for Stark effect Applied in Resonators (CAESAR) setup [171]. In figure 5.1, the left mirror which includes the nozzle and

a pair of microwave antennas is grounded, while the right mirror is set to a high potential of up to 12 kV. In between the two mirrors, 18 coaxially aligned circular electrodes are placed, held at increasing (from left to right) potentials, in order to homogenize the electric field over a large region in the resonator. This provides a more homogeneous electric field and therefore higher accuracy for the Stark shift measurements compared to previous setups, where parallel Stark plates above and below the resonator have been used [176]. Electric field strengths of up to 203 V/cm have been applied in the present measurements.

Electric field strength calibration measurements are done, using the $J = 1 \leftarrow 0$ transition of $OC^{36}S$ (0.02 % natural abundance) and a documented dipole moment of 0.71519(3) D [177]. For the calibration [178], an average effective parallel-plate separation l_{eff} is determined such that $E = U/l_{\text{eff}}$, where U is the applied voltage and E the electric field strength. The effective separation l_{eff} depends on the mirror separation. The electric potentials provided by a high voltage power supply (FuG HCD-20000) are calibrated using a high-precision voltmeter. For a displayed voltage U_{disp}, the applied voltage is given by $U/\text{V} = 3.86\,(70) + 1.00203\,(15)\,U_{\text{disp}}/\text{V}$. For two different relative mirror positions $z_1 = 7.21$ mm and $z_2 = 46.13$ mm, the effective plate separation is determined to $l_{\text{eff}_1} = 0.58343(31)$ m and $l_{\text{eff}_2} = 0.60099(55)$ m, respectively. The actual z-position is noted for each measurement. Using a linear interpolation, the l_{eff} value for each measurement is calculated. The estimated uncertainties of z are about 0.01 mm and much smaller than the error of l_{eff} and can therefore be neglected. In order to account for systematic errors, fits were performed at the extreme values of the electric field as derived from calibration of the voltage and of the effective plate separation l_{eff}. The uncertainty of the dipole moment in table 5.3 includes the systematic uncertainties.

5.3 Results

The lowest curve in figure 5.2 shows the measured field-free spectrum of the $J'_{K'_a\,K'_c}F' \leftarrow J''_{K''_a\,K''_c}F'' = 1_{01}0 \leftarrow 0_{00}1$ transition. The spectrum shows a Doppler splitting of ± 6.9 kHz at a mean frequency of 2763.39853 (50) MHz, which arises from the coaxial propagation of the supersonic jet into the microwave resonator. The magnitude of the Doppler splitting depends on the jet velocity and the microwave frequency. The asymmetry of the curve results from a small deviation of the frequency of the microwave pulse from the transition frequency.

Some of the lowest rotational transitions of benzonitrile in the range of 2.8–10.9 GHz are recorded with a linewidth (FWHM) of 2.5 kHz and a frequency

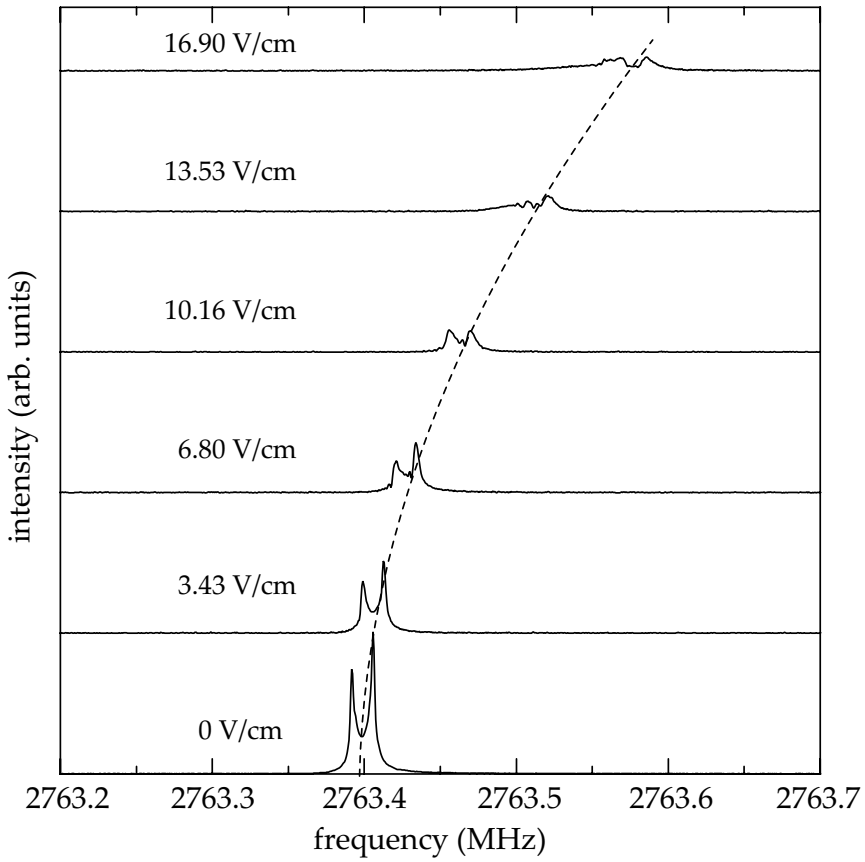

Figure 5.2: Spectrum of the $J'_{K'_a\,K'_c}F' \leftarrow J''_{K''_a\,K''_c}F'' = 1_{01}0 \leftarrow 0_{00}1$ transition. The bottom trace shows the Doppler doublet without any electric fields applied. The stacked traces show the Stark-shifted spectra for linearly increased electric fields. The traces are offset for clarity and the dashed line follows a square root function.

accuracy of 500 Hz. The measured field-free microwave transition frequency of these rotational transitions of benzonitrile together with their estimated uncertainties are listed in table 5.1. The estimated uncertainties vary due to the different signal-to-noise ratios for the individual measurements. Since the transition dipole moment is determined by the single molecular dipole moment component μ_a, all transitions obey a-type selection rules. Whereas the frequencies for the $J = 1 \leftarrow 0$ and $2 \leftarrow 1$ hyperfine transitions are reported for the first time, the accuracy for the $J = 3 \leftarrow 2$ and $4 \leftarrow 3$ transitions have been considerably improved with respect to previous measurements [179], and additional hyperfine splittings could be resolved.

We have simultaneously fit the newly measured lines together with previously published microwave transitions [179, 180], using the QStark program package [181, 182]. A weighted analysis of all lines has been performed, assuming for the transition frequencies from Fliege *et al.* [179] measurement accuracies of 20 kHz and for the transition frequencies from Vormann *et al.* [180] measurement accuracies of 5 kHz. The resulting rotational constants, centrifugal distortion constants, and nitrogen nuclear quadrupole coupling constants of benzonitrile are given in table 5.2. The values of the rotational constants are in good agreement with those found in the literature [179, 180, 183]. The nitrogen nuclear quadrupole coupling constants agree with those determined by the Kiel group using perturbation theory [179, 180] within the published error limits, and, moreover, the accuracy of these nuclear quadrupole coupling constants could be improved considerably in this study. The centrifugal distortion constants agree within error limits with those of high-J microwave transition measurements [183]. The inertial defect, which is also listed in table 5.2, is defined as [113]

$$\Delta I = I_c - I_a - I_b \,, \tag{5.1}$$

where the moments of inertia are calculated from the rotational constants (see chapter 2.1). The resulting value of the inertial defect $\Delta I = 0.0801\,(12)\,\mathrm{u{\cdot}\AA^2}$ is small and confirms the planarity of benzonitrile.

In order to determine the dipole moment of benzonitrile, Stark effect measurements in homogeneous electric fields have been performed on the $J'_{K'_a\,K'_c}F' \leftarrow J''_{K''_a\,K''_c}F'' = 1_{01}0 \leftarrow 0_{00}1$, $1_{01}1 \leftarrow 0_{00}1$, $1_{01}2 \leftarrow 0_{00}1$, and $4_{04}3 \leftarrow 3_{03}3$ transitions. For the deceleration experiments, the Stark effect of the rovibronic ground state of benzonitrile is of special interest, since it exhibits the largest Stark shift in strong electric fields (see chapter 2.1.3). Additionally, the selected transitions have good intensities.

$J'_{K'_a\,K'_c}$	←	$J''_{K''_a\,K''_c}$	F'	←	F''	frequency (MHz)	uncertainty (MHz)	obs.−calc. (MHz)
1_{01}	←	0_{00}	1	←	1	2760.22090	0.00050	0.00030
1_{01}	←	0_{00}	2	←	1	2761.49318	0.00150	0.00154
1_{01}	←	0_{00}	0	←	1	2763.39853	0.00050	-0.00011
2_{02}	←	1_{01}	1	←	0	5502.12082	0.00100	-0.00095
2_{02}	←	1_{01}	1	←	1	5505.30033	0.00100	0.00052
2_{02}	←	1_{01}	3	←	2	5503.27585	0.00100	0.00009
2_{02}	←	1_{01}	2	←	1	5503.19315	0.00100	0.00092
2_{02}	←	1_{01}	1	←	2	5504.02800	0.00100	-0.00077
2_{02}	←	1_{01}	2	←	2	5501.92073	0.00100	-0.00046
2_{02}	←	1_{01}	3	←	2	5503.27579	0.00100	0.00003
2_{11}	←	1_{10}	1	←	0	5856.56986	0.00100	-0.00059
2_{11}	←	1_{10}	1	←	1	5855.10867	0.00150	-0.00070
2_{11}	←	1_{10}	2	←	1	5853.96436	0.00100	-0.00029
2_{11}	←	1_{10}	1	←	2	5855.69296	0.00100	-0.00073
2_{11}	←	1_{10}	2	←	2	5854.54929	0.00100	0.00032
2_{11}	←	1_{10}	3	←	2	5855.28522	0.00100	0.00073
2_{12}	←	1_{11}	1	←	0	5191.71753	0.00050	0.00000
2_{12}	←	1_{11}	1	←	1	5190.00134	0.00050	-0.00017
2_{12}	←	1_{11}	2	←	1	5189.02665	0.00150	0.00008
2_{12}	←	1_{11}	1	←	2	5190.68619	0.00150	0.00170
2_{12}	←	1_{11}	3	←	2	5190.33981	0.00100	0.00062
3_{03}	←	2_{02}	4	←	3	8206.82990	0.00100	0.00066
3_{03}	←	2_{02}	3	←	2	8206.79124	0.00100	0.00102
3_{03}	←	2_{02}	2	←	1	8206.56481	0.00100	0.00051
4_{04}	←	3_{03}	5	←	4	10855.26125	0.00150	0.00071
4_{04}	←	3_{03}	4	←	3	10855.24427	0.00150	0.00092
4_{04}	←	3_{03}	3	←	2	10855.13590	0.00100	0.00043
4_{04}	←	3_{03}	3	←	3	10857.01706	0.00050	-0.00008
4_{04}	←	3_{03}	3	←	4	10855.62177	0.00200	-0.00178
4_{04}	←	3_{03}	4	←	4	10853.84943	0.00050	-0.00032

Table 5.1: Measured hyperfine-resolved field-free transition frequencies, estimated experimental uncertainties, and fit residuals. See text for details.

A (MHz)	5655.2654 (72)
B (MHz)	1546.875864 (66)
C (MHz)	1214.40399 (10)
χ_{aa} (MHz)	-4.23738 (36)
$\chi_{bb} - \chi_{cc}$ (MHz)	0.3397 (10)
χ_{bb} (MHz)	2.2886 (11)
χ_{cc} (MHz)	1.9488 (11)
Δ_J (kHz)	0.0456 (15)
Δ_{JK} (kHz)	0.9381 (56)
Δ_K (kHz)	0.50(38)
δ_J (kHz)	0.01095 (41)
δ_K (kHz)	0.628 (53)
ΔI (u·Å^2)	0.0801 (12)
number of measurements	93
σ (MHz)	0.00524
$\hat{\sigma}$	0.675

Table 5.2: Rotational constants, ^{14}N quadrupole coupling constants, centrifugal distortion constants (Watson's a-reduction), inertial defect, number of hyperfine-resolved components included in the fit, overall standard deviation, and weighted standard deviation from the fit of the field-free lines of benzonitrile. See text for details.

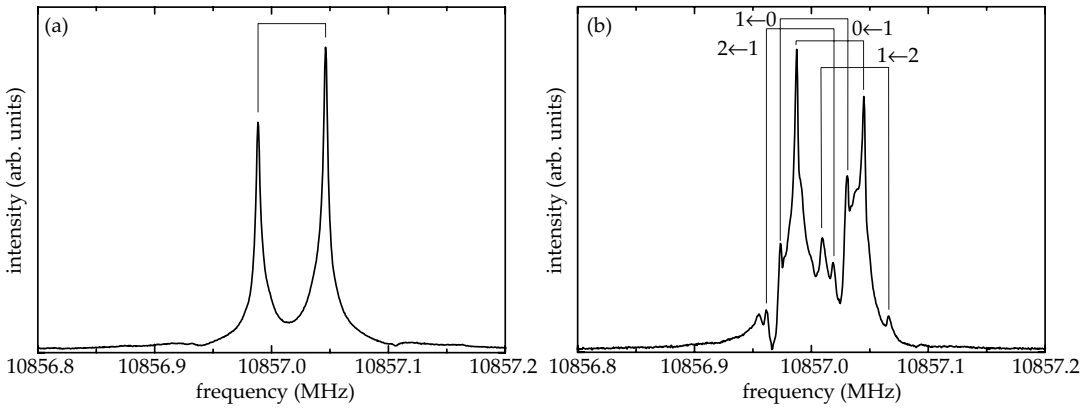

Figure 5.3: (a) Field-free spectrum of the $J'_{K'_a\,K'_c}F' \leftarrow J''_{K''_a\,K''_c}F'' = 4_{04}3 \leftarrow 3_{03}3$ transition. (b) Stark-splitted spectrum of the same transition at an electric field strength of 33.97 V/cm. The Doppler doublets with a splitting of ±14.5 kHz for the individual $M'_F \leftarrow M''_F$ transitions are indicated.

μ_a (D)	4.5152 (68)
number of measurements	78
σ (MHz)	0.00228
$\hat{\sigma}$	0.709

Table 5.3: Dipole moment, number of measurements at different electric field strengths, overall standard deviation, and weighted standard deviation from the fit of the Stark shifts at various electric field strengths. See text for details.

As an example, some spectra of the $J_{K_aK_c}F = 1_{01}0 \leftarrow 0_{00}1$ transition for different linearly increased electric fields are given in figure 5.2. The non-linear behavior of the Stark shifts in the electric fields is demonstrated and indicated by the dashed square root function. With increasing electric field strengths the individual lines are broadened, the intensity and the signal-to-noise ratio decrease, and the mean frequency can be derived with less accuracy. These effects are due to a residual inhomogeneity of the electric field.

In the electric field, the levels split into $(F + 1)$ distinct M_F sublevels. Due to the perpendicular Stark field and microwave field vectors in the CAESAR arrangement, only transitions with $\Delta M_F = \pm 1$ occur between the sublevels. The observed $4_{04}3 \leftarrow 3_{03}3$ transition in an electric field of 34 V/cm is shown in figure 5.3. For electric fields of up to 203 V/cm, the frequencies of the transitions in the electric field could be determined with uncertainties between 0.5 kHz and 8 kHz, depending on the J-complexity of the Stark-split and -shifted spectra and the electric field strength. From the Stark effect measurements, the electric dipole moment is determined to $\mu_a = 4.5152(68)$ D, which is listed together with the fit standard deviations in table 5.3. All measured Stark effect components are listed in table 5.4. The value of the dipole moment is in agreement (3σ) with the value from Stark shift measurements of the rotationally resolved laser-induced fluorescence spectrum [159], but differs considerably from previous microwave measurements [141, 168]. However, it should be noted that in the original publication the author stated that "attempts to study the Stark effect of benzonitrile encountered a number of difficulties," see reference 168 for details.

5.4 Conclusions

From Fourier-transform microwave spectroscopy of benzonitrile in a supersonic jet without and with applied electric fields, we have simultaneously determined the rotational constants, nitrogen nuclear quadrupole coupling constants, and centrifugal distortion constants of benzonitrile. The value of the dipole moment

of benzonitrile is determined precisely to $\mu_a = 4.5152(68)$ D from Stark shift measurements. This settles the issue regarding the value of the dipole moment of benzonitrile and allows precise simulations for the alternating-gradient focusing and deceleration measurements presented in chapter 6 of this thesis. Furthermore, it allows more precise predictions, which could help to detect benzonitrile in space.

$J'_{K'_a\,K'_c}$	←	$J''_{K''_a\,K''_c}$	F'	M'_F	←	F''	M''_F	Stark shift obs. (MHz)	Stark shift obs.−calc. (MHz)	uncertainty (MHz)	field strength (V/cm)
1_{01}	←	0_{00}	1	0	←	1	1	0.0039	-0.0012	0.0010	3.43
1_{01}	←	0_{00}	1	0	←	1	1	0.0194	-0.0008	0.0010	6.79
1_{01}	←	0_{00}	1	0	←	1	1	0.0454	0.0004	0.0010	10.16
1_{01}	←	0_{00}	1	0	←	1	1	0.0786	-0.0012	0.0010	13.52
1_{01}	←	0_{00}	1	0	←	1	1	0.1230	-0.0014	0.0020	16.89
1_{01}	←	0_{00}	1	0	←	1	1	0.4907	-0.0049	0.0050	33.71
1_{01}	←	0_{00}	1	0	←	1	1	1.1150	0.0017	0.0050	50.53
1_{01}	←	0_{00}	1	0	←	1	1	1.9849	0.0065	0.0050	67.38
1_{01}	←	0_{00}	1	1	←	1	0	0.0092	0.0007	0.0010	3.43
1_{01}	←	0_{00}	1	1	←	1	0	0.0323	-0.0006	0.0010	6.79
1_{01}	←	0_{00}	1	1	←	1	0	0.0740	0.0007	0.0010	10.16
1_{01}	←	0_{00}	1	1	←	1	0	0.1288	-0.0002	0.0010	13.52
1_{01}	←	0_{00}	1	1	←	1	0	0.1962	-0.0031	0.0020	16.89
1_{01}	←	0_{00}	1	1	←	1	0	0.7368	-0.0018	0.0030	33.71
1_{01}	←	0_{00}	1	1	←	1	0	1.5084	0.0017	0.0050	50.53
1_{01}	←	0_{00}	1	1	←	1	0	2.4690	0.0061	0.0050	67.39
1_{01}	←	0_{00}	0	0	←	1	1	0.0071	-0.0003	0.0005	3.43
1_{01}	←	0_{00}	0	0	←	1	1	0.0287	-0.0002	0.0005	6.80
1_{01}	←	0_{00}	0	0	←	1	1	0.0641	-0.0006	0.0005	10.16
1_{01}	←	0_{00}	0	0	←	1	1	0.1151	-0.0002	0.0010	13.53
1_{01}	←	0_{00}	0	0	←	1	1	0.1789	-0.0020	0.0010	16.90
1_{01}	←	0_{00}	0	0	←	1	1	0.2591	-0.0031	0.0010	20.26
1_{01}	←	0_{00}	0	0	←	1	1	0.3568	-0.0029	0.0020	23.63
1_{01}	←	0_{00}	0	0	←	1	1	0.4732	-0.0014	0.0020	27.00
1_{01}	←	0_{00}	0	0	←	1	1	0.6027	-0.0050	0.0020	30.36
1_{01}	←	0_{00}	0	0	←	1	1	0.7583	-0.0019	0.0030	33.73
1_{01}	←	0_{00}	0	0	←	1	1	0.9392	0.0057	0.0050	37.10
1_{01}	←	0_{00}	0	0	←	1	1	1.2460	0.0028	0.0080	42.27
1_{01}	←	0_{00}	2	0	←	1	1	0.8772	0.0076	0.0060	33.72
1_{01}	←	0_{00}	2	0	←	1	1	1.8011	-0.0004	0.0080	50.56
1_{01}	←	0_{00}	2	2	←	1	1	0.4899	-0.0062	0.0060	33.73

Continued on next page

$J'_{K'_a\,K'_c}$	←	$J''_{K''_a\,K''_c}$	F' M'_F	←	F'' M''_F	Stark shift obs. (MHz)	Stark shift obs.−calc. (MHz)	uncer-tainty (MHz)	field strength (V/cm)
1_{01}	←	0_{00}	2 2	←	1 1	1.5194	0.0036	0.0080	58.97
1_{01}	←	0_{00}	2 2	←	1 1	1.9893	0.0100	0.0080	67.39
1_{01}	←	0_{00}	2 2	←	1 1	3.1052	0.0138	0.0080	84.25
2_{11}	←	1_{10}	1 1	←	0 0	-0.0286	-0.0034	0.0020	3.50
2_{11}	←	1_{10}	1 1	←	0 0	-0.0920	-0.0007	0.0020	6.94
2_{11}	←	1_{10}	1 1	←	0 0	-0.2434	-0.0040	0.0030	13.80
2_{11}	←	1_{10}	1 1	←	0 0	-0.2636	-0.0027	0.0030	17.24
2_{11}	←	1_{10}	1 1	←	0 0	-0.2591	-0.0041	0.0030	18.96
2_{11}	←	1_{10}	1 1	←	0 0	-0.2444	-0.0049	0.0030	20.67
2_{11}	←	1_{10}	1 1	←	0 0	-0.2233	-0.0075	0.0060	22.39
2_{11}	←	1_{10}	1 1	←	0 0	-0.1894	-0.0045	0.0050	24.11
2_{11}	←	1_{10}	1 1	←	2 0	0.7319	0.0028	0.0050	25.83
2_{11}	←	1_{10}	1 1	←	2 0	0.7717	-0.0006	0.0100	27.54
4_{04}	←	3_{03}	3 0	←	3 1	-0.0007	-0.0006	0.0005	8.54
4_{04}	←	3_{03}	3 0	←	3 1	-0.0003	-0.0000	0.0010	17.01
4_{04}	←	3_{03}	3 0	←	3 1	-0.0012	-0.0001	0.0010	33.97
4_{04}	←	3_{03}	3 0	←	3 1	-0.0016	-0.0001	0.0010	42.45
4_{04}	←	3_{03}	3 0	←	3 1	-0.0018	-0.0002	0.0020	50.92
4_{04}	←	3_{03}	3 0	←	3 1	-0.0017	-0.0004	0.0020	59.40
4_{04}	←	3_{03}	3 0	←	3 1	0.0433	-0.0010	0.0040	127.21
4_{04}	←	3_{03}	3 1	←	3 0	-0.0081	0.0015	0.0010	25.49
4_{04}	←	3_{03}	3 1	←	3 0	-0.0153	0.0017	0.0010	33.97
4_{04}	←	3_{03}	3 1	←	3 0	-0.0253	0.0012	0.0010	42.45
4_{04}	←	3_{03}	3 1	←	3 0	-0.0409	-0.0029	0.0020	50.92
4_{04}	←	3_{03}	3 1	←	3 0	-0.0493	0.0023	0.0029	59.40
4_{04}	←	3_{03}	3 1	←	3 2	0.0075	0.0026	0.0020	17.02
4_{04}	←	3_{03}	3 1	←	3 2	0.0098	-0.0013	0.0010	25.49
4_{04}	←	3_{03}	3 1	←	3 2	0.0203	0.0002	0.0010	33.97
4_{04}	←	3_{03}	3 1	←	3 2	0.0336	0.0014	0.0010	42.45
4_{04}	←	3_{03}	3 1	←	3 2	0.0463	-0.0014	0.0020	50.92
4_{04}	←	3_{03}	3 1	←	3 2	0.1574	0.0009	0.0030	84.83
4_{04}	←	3_{03}	3 2	←	3 1	-0.0274	-0.0003	0.0010	33.97
4_{04}	←	3_{03}	3 2	←	3 1	-0.0463	-0.0045	0.0030	42.45
4_{04}	←	3_{03}	3 2	←	3 1	-0.0606	-0.0001	0.0020	50.92
4_{04}	←	3_{03}	3 2	←	3 1	-0.0804	-0.0003	0.0020	59.40
4_{04}	←	3_{03}	3 2	←	3 1	-0.4982	0.0008	0.0030	203.49
4_{04}	←	3_{03}	3 3	←	3 2	-0.0080	0.0002	0.0010	17.02
4_{04}	←	3_{03}	3 3	←	3 2	-0.0184	-0.0003	0.0010	25.49
4_{04}	←	3_{03}	3 3	←	3 2	-0.0351	-0.0033	0.0010	33.97

Continued on next page

$J'_{K'_a\,K'_c}$	←	$J''_{K''_a\,K''_c}$	F'	M'_F	←	F''	M''_F	Stark shift obs. (MHz)	Stark shift obs.−calc. (MHz)	uncer-tainty (MHz)	field strength (V/cm)
4_{04}	←	3_{03}	3	3	←	3	2	-0.2488	0.0006	0.0030	127.21
4_{04}	←	3_{03}	3	3	←	3	2	-0.2500	-0.0001	0.0030	135.68
4_{04}	←	3_{03}	3	3	←	3	2	-0.2423	-0.0001	0.0030	144.16
4_{04}	←	3_{03}	3	3	←	3	2	-0.2265	-0.0014	0.0030	152.63
4_{04}	←	3_{03}	3	3	←	3	2	-0.2001	-0.0022	0.0030	161.11
4_{04}	←	3_{03}	3	3	←	3	2	-0.1615	-0.0014	0.0030	169.59
4_{04}	←	3_{03}	3	3	←	3	2	0.1068	0.0030	0.0030	203.49
4_{04}	←	3_{03}	3	2	←	3	3	0.0278	0.0023	0.0010	25.49

Table 5.4: Measured Stark shifts of hyperfine levels in the electric field, estimated experimental uncertainties, and fit residuals.

Chapter 6

Alternating-gradient focusing and deceleration of benzonitrile

6.1 Introduction

In this chapter, which is based on reference 143, the focusing and deceleration of benzonitrile (C_7H_5N) using an array of time-varying inhomogeneous electric fields in alternating-gradient configuration are demonstrated. Benzonitrile is a prototypical large asymmetric top molecule that exhibits rich rotational structure and a high density of states (see chapter 2). At the rotational temperature of 3.0 K in the pulsed molecular beam, still about 1000 rotational states are populated. Experiments are performed with benzonitrile in various rotational states, including its absolute ground state $J'_{K'_a K'_c} = 0_{00}$. This is the only state that is stable against collisions at sufficiently low temperatures. Excited rotational states have the added complication of real and avoided crossings as a function of the electric field strength. It is not *a priori* clear whether one can focus and decelerate molecules in states within such a dense Stark manifold [119, 184]. However, this is successfully demonstrated in this chapter for the 1_{01} and 4_{04} state. All focusing and deceleration measurements are compared to trajectory simulations.

6.2 Rotationally resolved electronic excitation spectrum

The experimental setup and the detection scheme are described in detail in chapter 4. A part of the experimental vibrationless $S_1 \leftarrow S_0$ excitation spectrum, which is detected behind the AG decelerator using laser-induced fluorescence,

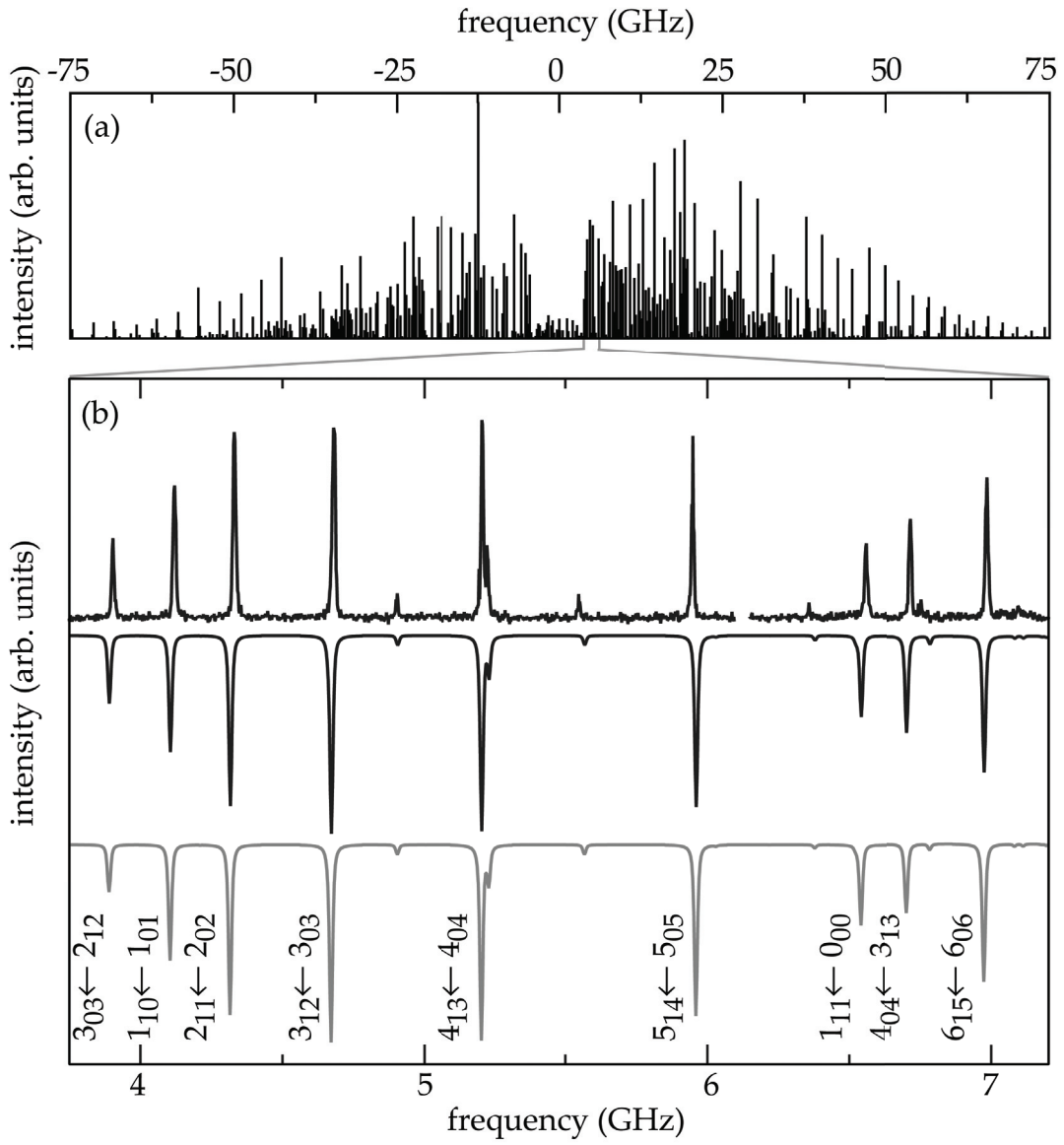

Figure 6.1: (a) Simulated rotationally resolved $S_1\, v' = 0\, J'_{K'_a\, K'_c} \leftarrow S_0\, v'' = 0\, J''_{K''_a\, K''_c}$ electronic excitation spectrum of benzonitrile at the rotational temperature of 3.0 K. The frequencies are given relative to the origin at 36512.74 cm^{-1}. (b) Expanded view of the experimental (upper black trace) and simulated spectrum using nuclear spin statistical weights of $(K'_a = \text{even}) : (K'_a = \text{odd}) = 20 : 17$ (middle black trace) and $(K'_a = \text{even}) : (K'_a = \text{odd}) = 5 : 3$ (lower grey trace). The line assignments for the strongest transitions are given.

is shown in figure 6.1(b). The individual rovibronic transitions are clearly resolved. For the frequency calibration, a 150 MHz Fabry-Pérot interferometer is used (see chapter 4), which is sensitive to temperature changes and mechanical vibrations. Hence, small frequency mismatches in the measured spectra can be attributed to slight shifts of the free-spectral-range value.

The spectrum is simulated using the known molecular constants (see chapter 5, references 159 and 115) and the program package Pgopher [185]. Good agreement with the measured spectrum is achieved using a rotational temperature of 3.0 K, the known natural linewidth (FWHM) of 8 MHz [159], and a Gaussian contribution of 7.5 MHz which accounts for Doppler broadening and laser linewidth. The transitions obey *b*-type selection rules. In order to record time-of-flight profiles for the AG focusing and deceleration measurements, the laser is set to the desired transition frequency. Specifically, the laser is set to the $J'_{K'_a K'_c} \leftarrow J''_{K''_a K''_c} = 1_{01} \leftarrow 0_{00}$, $1_{10} \leftarrow 1_{01}$, or $4_{13} \leftarrow 4_{04}$ transitions, for the focusing and deceleration measurements on the 0_{00}, 1_{01}, or 4_{04} states, respectively. In figure 6.1(a), the complete 0_0^0 band of the $S_1 \leftarrow S_0$ transition of the simulated spectrum at 3.0 K is presented.

In figure 6.1(b), two simulated traces are shown, which are calculated using different spin statistical weights. The lower grey trace gives the spectrum using the nuclear spin statistical weights with $(K'_a = \text{even}) : (K'_a : \text{odd}) = 5 : 3$, as expected for benzonitrile (see chapter 2.1.2), but the simulated intensities of states with $K'_a = 1$ (transitions: $3_{0\,3} \leftarrow 2_{1\,2}$ and $4_{0\,4} \leftarrow 3_{1\,3}$) are too small compared to the states with $K'_a = 0$. For the middle black trace, a nuclear spin statistical weight of $(K'_a = \text{even}) : (K'_a : \text{odd}) = 20 : 17 = 5 : 4.25$ is used, which matches the measured intensities for the lines with $K'_a = 1$ much better. This can be understood as explained in the following. Before the supersonic expansion, the nuclear spin states are in a thermal equilibrium at room temperature, and the nuclear spin statistical weights are $(K'_a = \text{even}) : (K'_a : \text{odd}) = 5 : 3$. During the expansion, the molecules are cooled to a rotational temperature of 3.0 K, but on the time scales of the experiment of a few ms the nuclear spins of the molecules do not thermalize. Taking that into account, the population in the beam is calculated. The populations of all states up to a certain J value are determined from a thermal distribution at room temperature. Then the levels are separated into individual ladders according to their spin symmetry (see chapter 2). The relative nuclear spin statistical weights for each stack are calculated to $(K'_a = \text{even}) : (K'_a : \text{odd}) = 5 : 4.16$ at room temperature. If one assumes that the nuclear spin statistics do not change during the supersonic expansion, this ratio will remain constant during the experiment. Indeed, this value matches the experimental measured intensities very well.

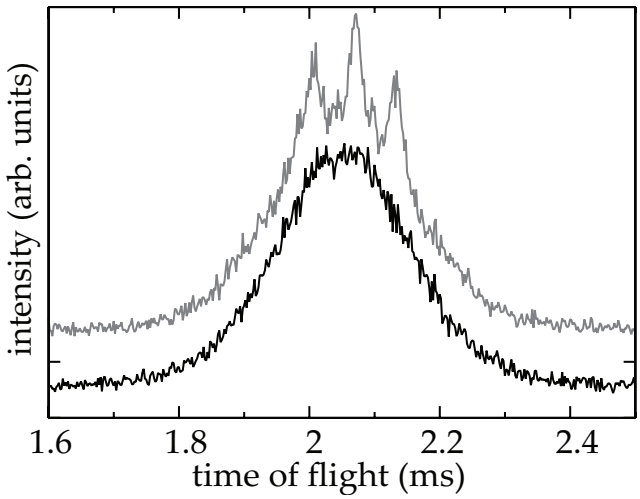

Figure 6.2: LIF signal of benzonitrile in its ground state as a function of time of flight from the nozzle to the detector. The lower (black) trace depicts the free-flight signal, and the upper (grey) trace, which is offset for clarity, depicts the signal for optimum focusing conditions.

6.3 Alternating-gradient focusing of benzonitrile

The switching scheme for the focusing of molecules in hfs states is discussed in detail in chapter 3.5. For all experiments presented in this section, the molecules are focused in both transverse and the longitudinal directions, but no change of the synchronous velocity occurs. This is achieved by switching the high voltage symmetrically around the center of the AG lenses. The amount of focusing and bunching is described by the focusing length f.

TOF profiles from the nozzle to the detector for the 0_{00} state are shown in figure 6.2, both for free flight, i. e. , when no voltages are applied to the decelerator, and for optimum focusing conditions. When the high voltages are applied, a structured TOF distribution is observed containing a background that resembles the free-flight distribution. The peak intensity of the focused molecules is enhanced by 30 % with respect to that of the molecules in free flight. For the TOF profiles, 16000 single measurements are averaged, corresponding to a measuring time of about 7 min at 40 Hz repetition rate.

In order to obtain the TOF from the nozzle to the detector, the delay time between the electronic trigger signal and the opening time of the nozzle is determined from the ground state focusing measurements as well as from the free-flight measurements in the source chamber (see chapter 4.3) to 0.4022 ms and

subtracted from the original data. In the remainder, the difference-TOF profiles, obtained by taking the difference of the measurements with and without electric fields, are shown and discussed. For the rotationally excited states, the difference between the focusing or deceleration measurements and the TOF profile with applied bias voltage (but no switched voltage) is taken. For the measurements on the 1_{01} state, a bias voltage of ± 200 V and for the 4_{04} state a bias voltage of ± 300 V is used for the suppression of unwanted transitions between levels at low electric field strengths.

Focusing sequences for the 0_{00}, 1_{01}, and 4_{04} states are presented in figure 6.3. In the experiments, three packets of focused molecules are observed. The central peaks of the TOF distributions occur 2.07 ms after the molecules exit the nozzle. These packets contain the synchronous molecule (see chapter 3.4). Hereafter, they are referred to as the "synchronous packets", and they are shaded in the simulated difference-TOF distributions. The peaks at earlier and later arrival times correspond to molecular packets leading and trailing the synchronous packet by one AG lens, respectively. These packets are also focused in all three dimensions. However, due to the electrode pattern in our setup (see chapter 4.4), they experience only 2/3 of the lenses at high voltage. This results in a reduced overall focusing for these packets.

For the focusing of the 0_{00} state, the synchronous packet is most intense for a focusing length of $f = 5$ mm. From the number of detected photons, the number of molecules per pulse confined in the central peak is estimated to be approximately 10^5 molecules, corresponding to a density of about 10^7 cm^{-3}. In this estimation, the quantum efficiency of benzonitrile and the PMT, the detection solid angle, and losses at filters are taken into account. The same number of molecules is calculated, if one assumes that for the supersonic expansion about 10^{10} molecules in a volume of 0.01 cm^3 are per pulse are in the ground state. The fraction of molecules which is accepted by the AG decelerator can be determined using trajectory simulations with misalignment.

For smaller focusing lengths, a shallower time-averaged confinement potential is created, and less molecules are guided through the decelerator. For larger focusing lengths, the synchronous packet is over-focused, also resulting in a decreased transmission. For $f = 7$ mm, the over-focusing is so severe that the synchronous packet completely disappears. As expected, the non-synchronous packets benefit from the increased focusing lengths. Figures 6.3(b) and 6.3(c) show the focusing behavior for the 1_{01} and 4_{04} state, respectively. The observed focusing effects are similar to those for the 0_{00} state. Due to the smaller Stark shifts, a larger optimum focusing length of $f = 6$ mm for the 4_{04} state is ex-

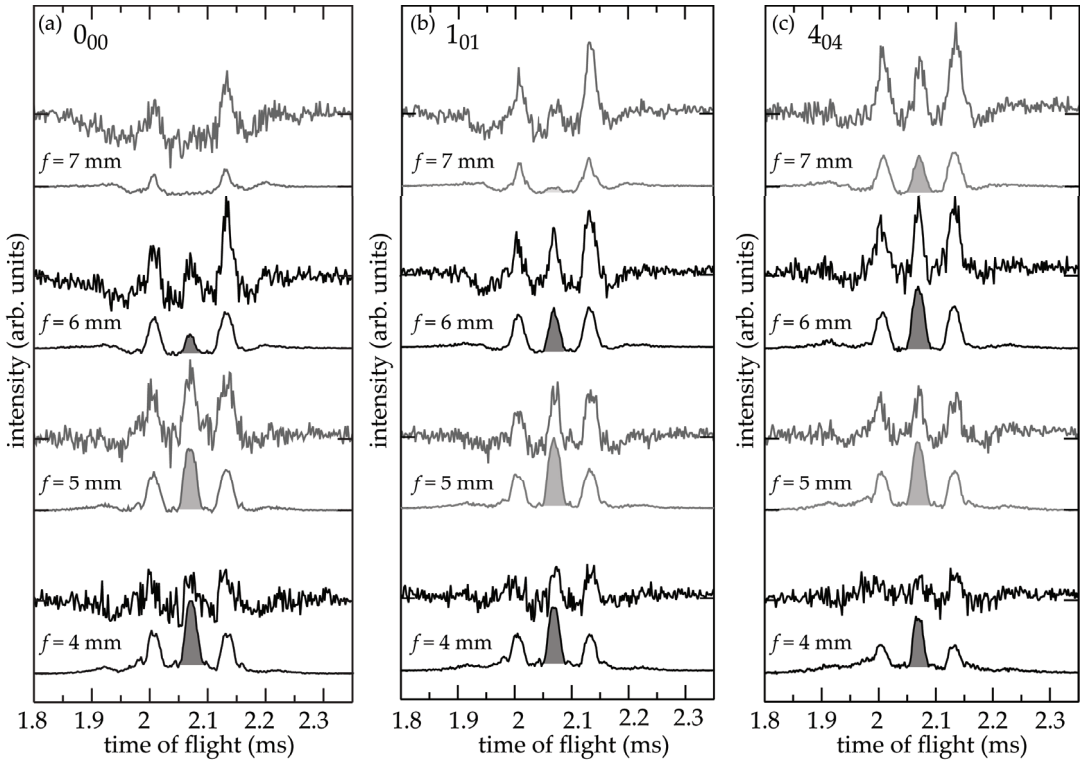

Figure 6.3: Sequence of difference-TOF profiles for the (a) 0_{00}, (b) 1_{01}, and (c) 4_{04} states of benzonitrile obtained using different focusing lengths f for a constant velocity of 320 m/s. The upper traces show the difference between the experimental TOF profiles with and without high voltages applied. The lower traces show the corresponding simulations, where the packets containing the synchronous molecule have been shaded.

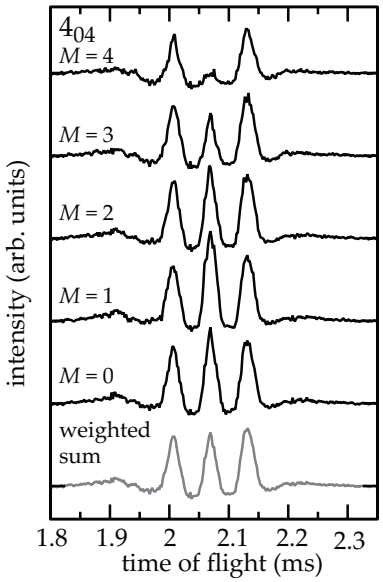

Figure 6.4: The upper traces show simulations of difference-TOF profiles for the different M levels for the 4_{04} state of benzonitrile, and the lowest grey trace shows the weighted sum. The switching sequence is calculated for a velocity of 320 m/s and a focusing strength of $f = 7$ mm. The traces are offset for clarity.

perimentally found for the synchronous packet. For the 1_{01} state, a maximum peak intensity is obtained between $f = 5.0$ mm and $f = 6.0$ mm. Actually, $f = 5.5$ mm (not shown) is the optimum focusing length for the 1_{01} state and, therefore, used for the measurements in the next section 6.4.

The 4_{04} state has five individual M levels. Each M level has a distinct Stark curve and, therefore, a distinct focusing behavior (see chapter 2.1.3). This is illustrated in figure 6.4, where the simulations for the individual M levels of the 4_{04} state for a beam with 320 m/s at a focusing length of $f = 7$ mm and the weighted sum (grey trace) are shown. It is clearly seen that the synchronous packet for the $M = 1$ level, which has the smallest effective dipole moment, is optimally focused, while the $M = 4$ level, which has the largest effective dipole moment, is strongly over-focused. The measured TOF profiles are composed of these five individual contributions, where the non-zero M levels are two-fold degenerate. Therefore, in the simulations of the measurements, the weighted sums are given. For the 4_{04} state in figure 6.3(c), a considerably weaker dependence of the overall transmission on the exact focusing length is observed.

The simulated TOF distributions obtained from trajectory simulations match the experimental results very well. The parameters, fitted to obtain a good agree-

state	v_{z_0}	Δv_z	Δt
0_{00}	323 m/s	30 m/s	150 μs
1_{01}	322 m/s	30 m/s	150 μs
4_{04}	323 m/s	37 m/s	150 μs

Table 6.1: Beam parameters used in the simulations of the focusing measurements. Listed are the longitudinal beam velocity v_{z_0}, the longitudinal velocity spread Δv_z, and the time width Δt. See text for details.

ment of the simulations with the original TOF distributions with and without electric field, are listed in table 6.1. Before each measurement series, the parameters of the molecular beam are optimized in order to obtain a maximum signal and a narrow time spread. However, the conditions of the molecular beam vary slightly from day to day, and, therefore, the parameters of the simulations have to be adapted. For all focusing measurements, the initial mean velocity of the molecules is a bit larger then the velocity of 320 m/s, at which the molecules are focused. The initial time width of $\Delta t = 150\,\mu$s corresponds to the opening time of the nozzle (see chapter 4.3). Other parameters of the simulations are equal for all traces: the initial widths of the molecular packet $\Delta x = \Delta y = \Delta z = 2$ mm and the initial transverse velocity spread $\Delta v_x = \Delta v_y = 20$ m/s. Only the molecules which pass the 1.5 mm diameter skimmer are considered further in the simulation. Behind the decelerator, only molecules in a 1 mm $\times$ 20 mm rectangle along the transverse plane, representing the size of the detection laser, are detected. The detection laser line width and Doppler broadening effects are included in the simulations.

All simulated profiles are scaled down by a factor of seventeen. This can be attributed to mechanical misalignments of the electrodes. The influence of the misalignment on the transverse acceptance is discussed in chapter 3.8. In figure 6.5, the decrease of the focusing intensities is shown for the difference-TOF profiles obtained from three-dimensional trajectory calculations for optimum focusing for the 0_{00} state of benzonitrile. For each electrode stage, the displacement values in x, y, and z are randomly chosen from a Gaussian distribution with the standard deviation Δ. For each misalignment trace, twenty simulations with randomly chosen misalignments for five million molecules have been averaged. A mechanical misalignment of about $m = 100\,\mu$m is sufficient to explain the scaling factor. From the setup of the decelerator, a transverse misalignment of about $\pm 50\,\mu$m and a longitudinal misalignment of about $\pm 100\,\mu$m is found (see chapter 4.4), such that the scaling factor is slightly larger than expected. However, in the simulations not all effects which occur in the experiment are

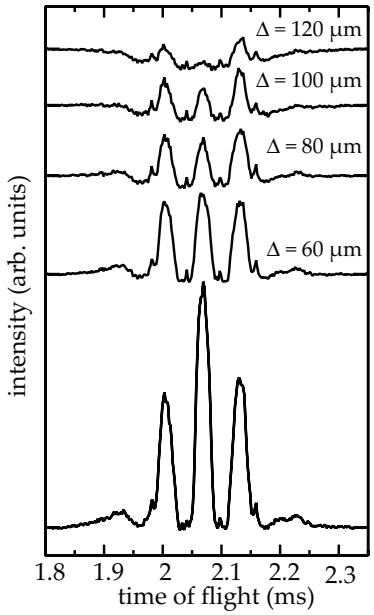

Figure 6.5: Simulations of difference-TOF profiles for optimum focusing at 320 m/s of the 0_{00} state of benzonitrile. The bottommost trace is simulated without misalignment, whereas for the upper traces displacement values for the electrode stages in x, y, and z are randomly chosen from a Gaussian distribution with standard deviations Δ indicated. The traces are offset for clarity.

included: misalignments of the detection laser, skimmer, or of the individual electrodes in an electrode pair relative to each other. For example, the detection laser is aligned to obtain optimum signal, but due to the long pathway from the laser to the experiment, the laser position can move slightly. This is reduced to about 100 μm by using an active beam align detector (see chapter 4.6). In figure 6.5 it is also shown that with increasing Δ the synchronous peak decreases stronger than the other peaks. This is also partly seen in figure 6.3, where the relative heights of the non-synchronous peaks are larger in the experimental data than predicted from the simulations. A better agreement of the simulations with the measurements could be obtained if the misalignment was partly included in all trajectory simulations instead of scaling all measurements down by an overall factor. However, because a more realistic description of all misalignment effects is very difficult, this is not done here.

For the measurements on the rotationally excited states, a bias voltage is used instead of ground. The dependence of the integrated intensity of the synchronous peak on the bias voltage is studied for the optimum focusing switching sequence (f = 6 mm) for the 4_{04} state. The results are shown in figure 6.6(a), where

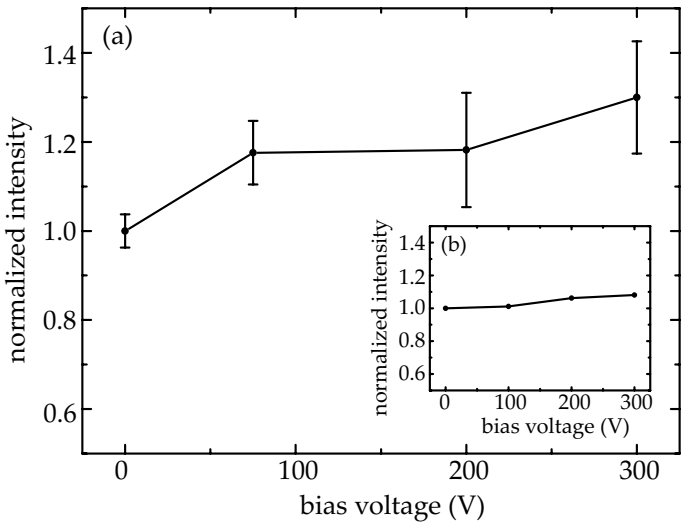

Figure 6.6: (a) Normalized integrated intensity as a function of the absolute value of the bias voltage for optimum focusing with $f = 6$ mm for the 4_{04} state. (b) Inset: simulated bias voltage dependence of the TOF profiles without switched high voltages applied.

a maximum signal is achieved for a bias voltage of ±300 V. ±300 V is the maximum bias voltage that currently can be applied. For the 4_{04}, state avoided crossings occur at fields up to 25 kV/cm (see figure 2.2), such that the bias voltage of ±300 V is not large enough to prevent all possible transitions. For a bias voltage of ±300 V, the normalized integrated intensity is increased by about 30 % compared to the measurement without bias voltage. For comparison, the simulated bias voltage dependence for the TOF profiles without switched high voltages applied for the 4_{04} state is shown in figure 6.6(b). Only a small increase of the intensity of about 8% at a bias voltage of ±300 V is obtained in the simulations and is in good agreement with the measured TOF profile with only a bias voltage applied. This small increase is due to focusing effects of the 4_{04} state in the bias field. In figure 6.6(a), the error bars are relatively large due to a limited number of measurements, experimental fluctuations of the detection laser power and position, and the beam intensity. However, the intensity of the synchronous peak is clearly increased for bias voltages larger than 75 V compared to the case where no bias voltage is applied. This increase cannot only be explained due to focusing effects of the bias field. Therefore, the increased intensity for the synchronous peak is an evidence that unwanted transitions at a zero electric field are indeed reduced by applying an additional

bias voltage. Furthermore, from the comparison of the focusing measurements for the different quantum states, it can be seen that no additional losses for the 4_{04} state compared to the 0_{00} state are observed when a bias voltage of ± 300 V is used. This shows that, if a sufficiently high bias voltage is used, the transitions between different states at avoided crossings will not be as severe as might have been anticipated [119, 184].

6.4 Alternating-gradient deceleration of benzonitrile

Figure 6.7 presents the results for the deceleration of benzonitrile in its 0_{00} and 4_{04} states starting from 320 m/s and figure 6.8 the deceleration of benzonitrile in its 1_{01} state starting from 325 m/s. For the TOF profiles, 16000 single measurements (20000 single measurements for deceleration of the 0_{00} state) are averaged. For the focusing measurements of the 0_{00} state no bias voltage is used, but in the measurements on the 1_{01} state and 4_{04} state bias voltages of ± 200 V and ± 300 V are used, respectively. The bottommost (black) traces show focusing experiments for a constant velocity of the synchronous molecule of 320 m/s (325 m/s), using the optimum focusing lengths of $f = 5$ mm for 0_{00} state, $f = 5.5$ mm for the 1_{01} state, and $f = 6.0$ mm for the 4_{04} state. The other traces show experiments in which the synchronous packet is decelerated from 320 m/s (325 m/s) to successively lower velocities, resulting in later arrival times at the detector.

For the 0_{00} state (see figure 6.7(a)) using $d = 5.0$ mm, the packet is decelerated to 289 m/s, corresponding to a reduction of the kinetic energy by 18 %. For the topmost trace, recorded using $d = 5.5$ mm, the molecules are decelerated from 320 m/s to 275 m/s, which is a reduction of the kinetic energy of 26 %. The 4_{04} state (see figure 6.7(b)) is decelerated from 320 m/s to 296 m/s using $d = 5.0$ mm such that the kinetic energy is reduced by 14 %. The 4_{04} state is decelerated less than the 0_{00} state for the same d value due to its smaller effective dipole moment. 17 % of the kinetic energy is removed for the 4_{04} state using $d = 5.25$ mm. For each deceleration measurement, the focusing length is optimized, which is for the 0_{00} state $f = 5$ mm for focusing and deceleration to 312 m/s and $f = 4.75$ mm for all other deceleration traces. Generally, for lower velocities smaller focusing lengths are needed. For the 4_{04} state, the focusing lengths are $f = 6.0$ mm for focusing and the deceleration to 313 m/s and 305 m/s and $f = 5.75$ mm for the other deceleration traces. The deceleration of the 1_{01} state from 325 m/s is shown in figure 6.8. For $d = 5.0$, the molecules are

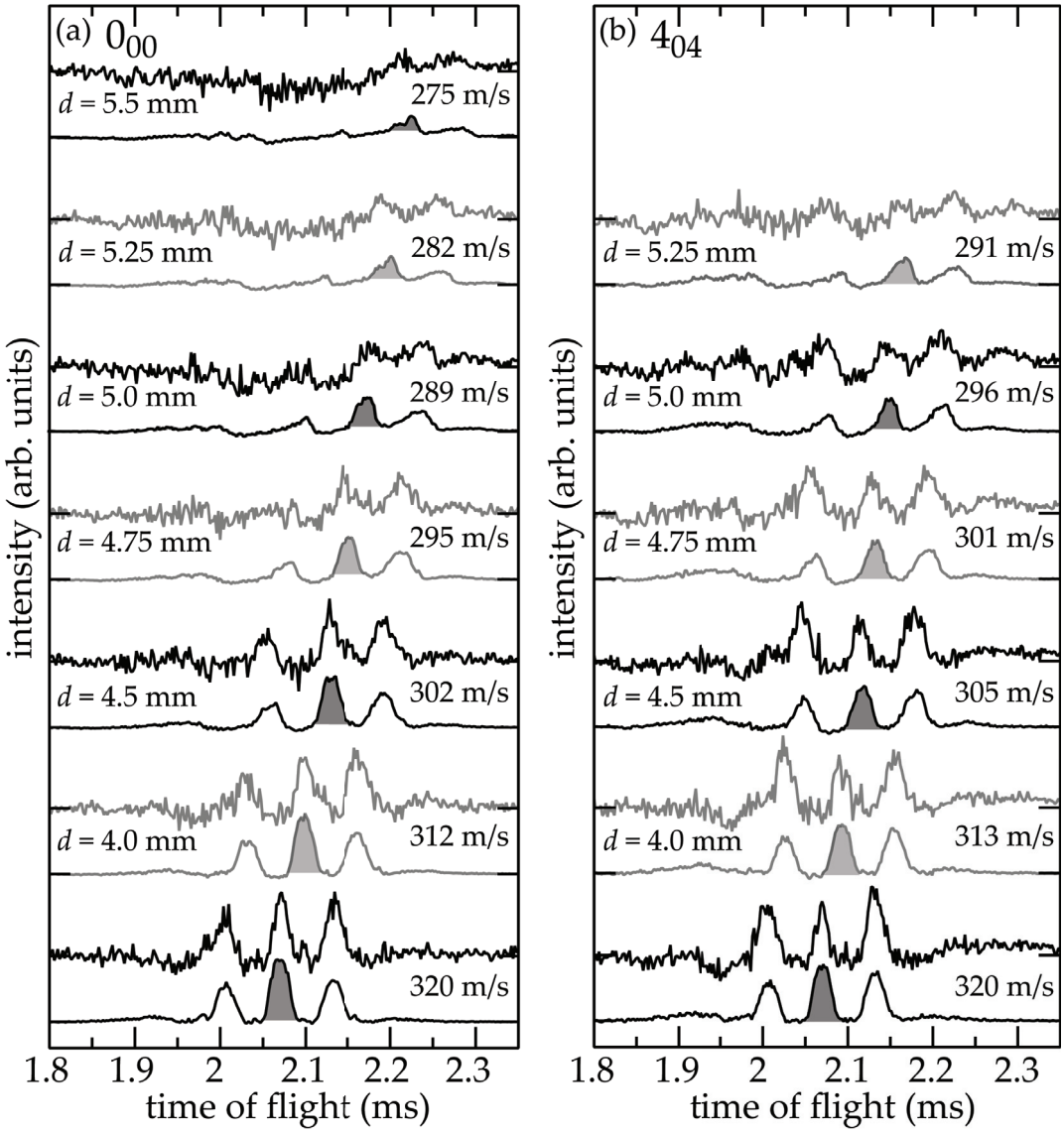

Figure 6.7: Sequence of difference-TOF profiles for the deceleration of the (a) 0_{00} and (b) 4_{04} states of benzonitrile from an initial velocity of 320 m/s to the indicated final velocities. The positions d that have been used to reach these final velocities are specified. The upper traces show the difference between the experimental TOF profiles with and without high voltages applied. The lower traces show the corresponding simulations, where the packets containing the synchronous molecule have been shaded. See text for details.

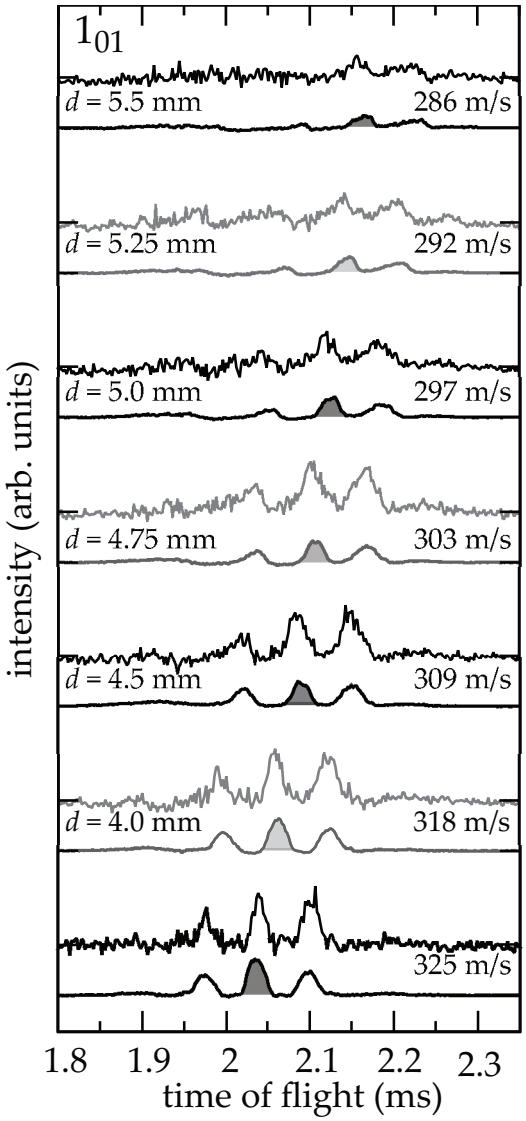

Figure 6.8: Sequence of difference-TOF profiles for the deceleration of the 1_{01} state of benzonitrile from an initial velocity of 325 m/s to the indicated final velocities. The positions d that have been used to reach these final velocities are specified. The upper traces show the difference between the experimental TOF profiles with and without high voltages applied. The lower traces show the corresponding simulations, where the packets containing the synchronous molecule have been shaded. See text for details.

state	v_{z_0}	Δv_z	Δt
0_{00}	323 m/s	30 m/s	150 μs
1_{01}	325 m/s	32 m/s	150 μs
4_{04}	325 m/s	33 m/s	200 μs

Table 6.2: Beam parameters used in the simulations of the deceleration measurements. Listed are the longitudinal beam velocity v_{z_0}, the longitudinal velocity spread Δv_z, and the time width Δt. See text for details.

decelerated to 297 m/s and for $d = 5.5$ mm to 286 m/s, which means that 16 % or 23 % of the kinetic energy are removed, respectively. The focusing lengths are $f = 5.5$ mm for focusing and the deceleration to 318 m/s, 309 m/s, and 303 m/s. It is $f = 5.25$ for the other traces.

When deceleration to lower velocities is performed by increasing d, as is done here, the signal intensity decreases due to the reduction in phase space acceptance. The observed intensities of the non-synchronous packets decrease more strongly with increasing d. Because the molecules in these packets miss every third deceleration stage, their trajectories are not stable and they are only observed due to the finite length of the decelerator. One could also decelerate to lower velocities by increasing the number of AG lenses for a given value of d (see section 6.7).

The deceleration behavior of the 1_{01} state and of the 4_{04} state are similar to that of the ground state. This demonstrates that such molecules in rotationally excited states can indeed be focused and decelerated. It is important to realize that the optimum deceleration time sequences differ for the individual M levels. Here, the time sequences are calculated for the $M = 0$ level. Apart from slightly different final velocities and intensities, analogue results are obtained for time sequences calculated for other M levels. For a considerably longer decelerator and a given time sequence, the M levels could, in principle, be separated based on their different Stark shifts (see also figure 6.4).

The optimum parameters for the deceleration simulations are listed in table 6.2. The other initial parameters are equal to the parameters for the focusing simulations, which are $\Delta x = \Delta y = \Delta z = 2$ mm and $\Delta v_x = \Delta v_y = 20$ m/s. For all deceleration measurements up to $d = 5.0$ mm, the relative intensities and the arrival times of the molecular packets at the detector are nicely reproduced by the trajectory simulations. For the deceleration measurements for the 1_{01} state, the overall scaling factor of seventeen seems to be too large. This can be

understood by the behavior of the 1_{01} state when a bias voltage is applied which is different from the behavior of the 4_{04} state. The peak signal intensity of the free-flight TOF of the 1_{01} state is decreased by about 20 % if a bias voltage of $\pm$200 V is applied. However, this bias voltage results in a better contrast of the focused and decelerated peaks compared to the free-flight TOF, and is therefore used in the measurements. For the difference-TOF profiles the decreased distribution at $\pm$200 V is subtracted from the TOF profiles with switched electric fields. Because the decrease of the signal with the bias voltage is not included in the simulations, the overall scaling factor is too large for the 1_{01} state.

If the molecules are decelerated using d values larger than $d = 5.0$ mm, the synchronous packet in the experimental measurements is detected earlier than in the simulations. For example, for the 0_{00} state (see figure 6.7(a)) the synchronous packet is detected 5 μs earlier for $d = 5.25$ and 7 μs earlier for $d = 5.5$ than predicted, which means that the molecules are decelerated a bit less than expected. A similar effect is observed in the deceleration measurements for the 1_{01} state for large d values (see figure 6.8) and the 4_{04} state (see figure 6.7(b)). In chapter 3.4, it has been shown that the point of inflection of the electric field along the molecular beam axis is at 5.0 mm. Only for d values up to $d = 5.0$ mm the molecules are bunched properly in longitudinal direction. When the molecules are decelerated using a larger d, they are no longer bunched properly, resulting in a decreased intensity and a broader synchronous peak. This is also seen in the corresponding simulations. Simulations including misalignments of the electrodes show that the molecules are decelerated and bunched less than in simulations without misalignment. Therefore, the earlier arrival of the synchronous peak can be explained by misalignment effects.

Focusing and deceleration experiments have also been performed for the 6_{06} state of benzonitrile, which has been decelerated from 320 m/s to 300 m/s using $d = 4.75$ mm and $f = 5$ mm. Due to the smaller overall Stark shift of the 6_{06} state, the AG focusing and deceleration is more difficult than for the other states discussed above. Because of experimental difficulties with the detection, the data are not presented here. Already in the current experiment, a significant amount of state selection is achieved. Whereas the different low-energy rotational states investigated in this thesis are focused and decelerated with similar acceptances, higher rotational states often have negligible Stark shifts and are practically not accepted by the decelerator. Partly, this is already observed in the poor acceptance for the 6_{06} state.

6.5 Phase space acceptances

Phase space distributions allow a better understanding of measured TOF profiles. The distributions determined from trajectory simulations for optimum focusing ($f = 5$ mm) for the 0_{00} state, are shown in figure 6.9. For each graph the horizontal axis corresponds to the position and the vertical axis to the velocity along a specific direction in space. In the TOF profiles in figure 6.3(a) three molecular packets are visible, i. e. , the synchronous packet and the leading and trailing non-synchronous packets. The phase space distributions are presented for the three molecular packets. For each molecular packet, the phase space distributions are determined only for the molecules which arrive within the arrival time interval corresponding to one of the three peaks in the TOF profiles. For the three molecular packets, the two transverse and the longitudinal phase space distributions are given 20 mm before the center of the first AG lens (figures 6.9(a), (b), and (c)) and 20 mm behind the center of the last AG lens (figures 6.9(d), (e), and (f)). For instance, figure 6.9(c) shows the longitudinal phase space acceptance before the entrance of the decelerator, and indeed the three different peaks in the TOF profiles correspond to molecular packets, leading and trailing the synchronous packet by one AG lens (or 20 mm), respectively. The cut-off shape of the three molecular packets in figure 6.9(f) is due to the selection of the molecular packets due to their arrival time in the TOF profile. The transverse acceptances before the entrance of the decelerator are similar for all three molecular packets, but behind the decelerator the phase space is rotated differently for the synchronous and non-synchronous packets. This is due to the effect that the non-synchronous molecules experience only 2/3 of the focusing fields.

By comparing the graphs before and behind the decelerator, it is seen that the phase space areas remain constant, in accordance with Liouville's theorem. From the phase space areas the acceptance of the decelerator can be determined. The approximate size of the phase-stable areas is indicated by a white rectangle, which has in all graphs the same area in the phase space distributions before and behind the decelerator. The rectangle gives only an estimate of the phase-stable area, as this has an elliptical shape (see chapter 3.4). The approximate transverse acceptance is about 2.5 mm $\times$ m/s along the x-direction, and about 4.2 mm $\times$ m/s along the y-direction. The transverse acceptance is larger for y than for x, because the last two AG lenses are focusing in y-direction and the whole decelerator consists of 14 focusing elements along the y-direction, but only 13 focusing elements along the x-direction. In figure 6.9(d) the phase space acceptance appears larger than the indicated rectangle, but the density of molecules outside the rectangle is much smaller than inside the rectangle.

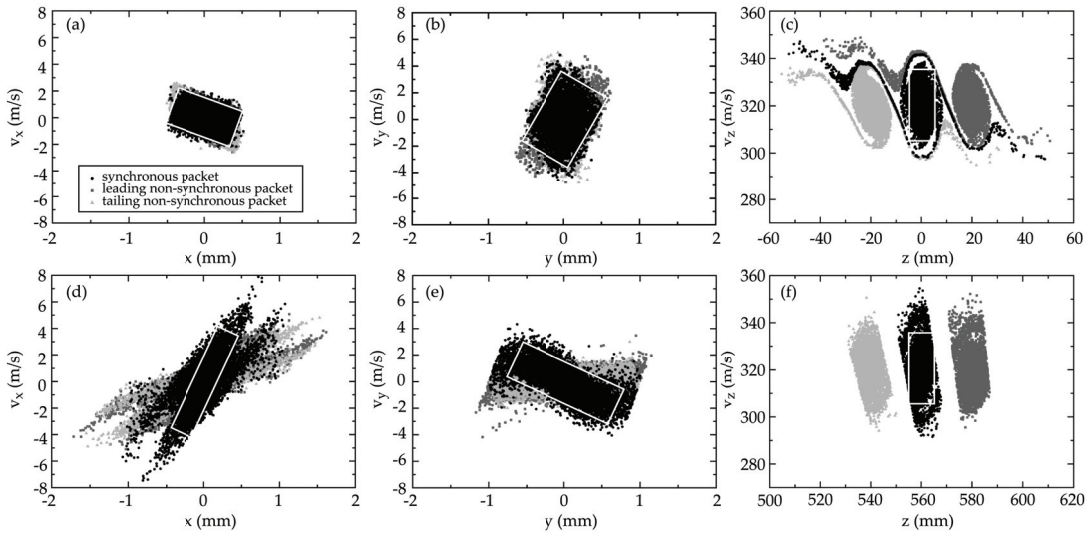

Figure 6.9: Phase space acceptances for the 0_{00} state of benzonitrile obtained from trajectory simulations for focusing using $f = 5$ mm at a velocity of 320 m/s. The distributions are given for molecules which are accepted in the synchronous (black) and the leading and tailing non-synchronous (grey) packets. (a), (b), and (c) show the two transverse and the longitudinal phase space distributions 20 mm before the center of the first AG lens ($z = 0$ mm), whereas (d), (e), and (f) show the distributions 20 mm behind the center of the last AG lens ($z = 560$ mm). The white rectangles give an estimate for approximate size of the phase-stable area for the synchronous packet.

The molecules outside the rectangle move on metastable trajectories and are not considered in the given phase space area. The longitudinal acceptance is about 30 mm × m/s, resulting in a total six-dimensional phase space acceptance of about 315 $mm^3 \times (m/s)^3$. It should be noted that the exact determination of the phase acceptance is difficult for a decelerator which only consists of 27 AG lenses. Molecules which move on metastable trajectories are also detected due to the finite length. Therefore, the uncertainties of the given acceptances are relatively large. The transverse four-dimensional phase space acceptance obtained from three-dimensional trajectory simulations for this decelerator is about 10.5 $mm^2 \times (m/s)^2$, which is larger than the transverse acceptance determined from pure two-dimensional simulations of a 96 stages long decelerator for $f = 5$ mm of 6.7 $mm^2 \times (m/s)^2$ (see figure 3.10 in chapter 3.8). This occurs due to a better longitudinal bunching for $f = 5$ mm and shows that three-dimensional trajectory simulations are needed to describe the motions in the AG decelerator.

The transverse and longitudinal phase space distributions for the deceleration of benzonitrile in the 0_{00} state from 320 m/s to 289 m/s before and behind the decelerator are shown in figure 6.10. As discussed before, for each molecular packet, the phase space distributions are determined only for the molecules which arrive within the arrival time interval corresponding to one of the three peaks in the deceleration TOF profiles. Figures 6.10(c) and (f) show the phase spaces along the z-direction. At the entrance of the decelerator, the phase space of the synchronous packet has an average velocity of about 320 m/s. Behind the decelerator, the mean velocity is reduced to about 289 m/s, which shows that the molecules are decelerated according to the applied high voltage switching sequence. From the phase space distributions of the non-synchronous molecules, it is seen that the non-synchronous peaks originate from molecules which start with an average velocity of about 312 m/s one AG lens before or behind the synchronous molecule. Due to the finite length of the decelerator, these molecules are also accepted and decelerated to an average velocity of about 296 m/s behind the decelerator.

For the deceleration phase space distributions, the transverse acceptance for the synchronous packet along the x-direction is about 2.0 mm × m/s, and along the y-direction about 3.8 mm × m/s. The longitudinal acceptance is about 25 mm × m/s, resulting in a total six-dimensional phase space acceptance of about 190 $mm^3 \times (m/s)^3$. All acceptances are reduced for the deceleration compared to the focusing acceptances, resulting in a decreased intensity of the synchronous packet in the difference-TOF profiles.

In figure 6.10(f), only the molecules of the synchronous packet inside the

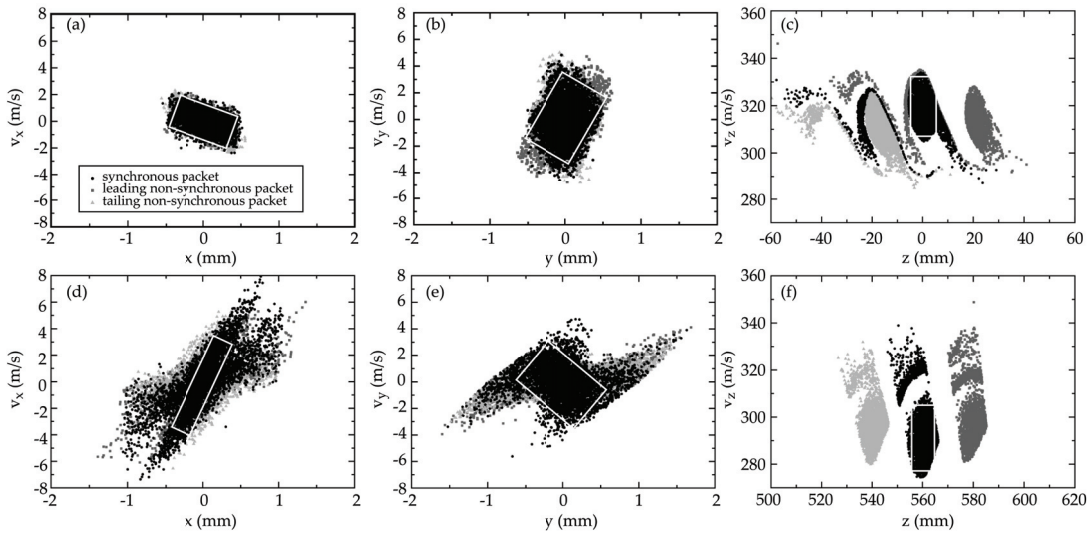

Figure 6.10: Phase space acceptances for the 0_{00} state of benzonitrile obtained from trajectory simulations for deceleration from 320 m/s to 289 m/s for $f = 4.75$ mm and $d = 5$ mm. The distributions are given for molecules which are accepted in the synchronous (black) and the leading or tailing non-synchronous (grey) packets. (a), (b), and (c) show the two transverse and the longitudinal phase space distributions 20 mm before the center of the first AG lens, whereas (d), (e), and (f) show the distributions 20 mm behind the center of the last AG lens. The white rectangles give an estimate for approximate size of the phase-stable area for the synchronous packet.

lower ellipse are phase stably accepted. The molecules in the upper area with velocities of about 320 m/s are molecules originating from the phase space area in figure 6.10(c) around the position $z = -20$ mm with an average velocity of 313 m/s before the decelerator. These molecules move on metastable trajectories and would be lost in a longer decelerator (see section 6.7). These metastable phase space areas occur also for the focusing phase space distributions in figures 6.9(c) and (f). The longitudinal phase space areas have a similar structure and area for pure one-dimensional simulations along the molecular beam axis. Therefore, the longitudinal phase space acceptance is not reduced as a result of loss effects due to the coupling of longitudinal and transverse motion, as observed for the normal Stark decelerator [186]. A general advantage of the AG decelerator compared to the normal Stark decelerator is the better decoupling of the longitudinal and transverse motion such that unwanted parametric amplifications of the motions of the molecules can be avoided (see also chapter 7.6).

6.6 Deceleration measurements of benzonitrile seeded in krypton

In all experiments shown so far, benzonitrile has been seeded in xenon in order to obtain a molecular beam with a low initial velocity. Benzonitrile can also be seeded in other carrier gases, for instance, in krypton. The disadvantage is that, due to the smaller mass of krypton compared to xenon, the initial velocity is larger. Therefore, a longer decelerator is needed to decelerate benzonitrile to similar final velocities. One advantage is that the free-flight TOF profiles of benzonitrile seeded in krypton have a higher intensity and a smaller time spread due to a better quality of the produced molecular beam. In figure 6.11, the lowest traces show free-flight and the upper traces focusing and deceleration experiments for the 1_{01} state together with the corresponding simulations. Here, the original TOF profiles and not the difference-TOF profiles are shown. The peak intensity of the central peak for optimum focusing is a factor 2.6 increased compared to the free-flight signal, which is a much larger enhancement factor than for benzonitrile seeded in xenon. For the topmost traces, the synchronous packet is decelerated from 385 m/s to 359 m/s for $d = 5.0$ mm, corresponding to a reduction of the kinetic energy of 13 %.

The measurements were performed with an early version of the experimental setup, where the distance from the exit of the decelerator to the detection region was 103 mm (instead of 65 mm), resulting in a detection of the molecules 700 mm

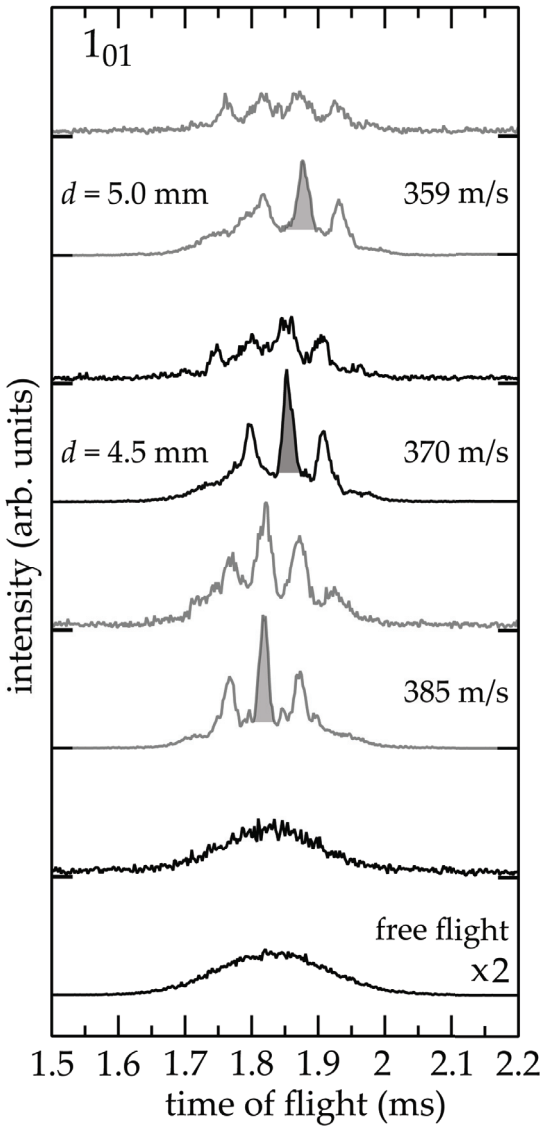

Figure 6.11: Sequence of TOF profiles for the deceleration of the 1_{01} state of benzonitrile seeded in krypton from an initial velocity of 385 m/s to the indicated final velocities. The positions d that have been used to reach these final velocities are specified. The traces are offset for clarity. The lowest traces show the free-flight TOF profile without any high voltages applied. The upper traces show the experimental TOF profiles with high voltages applied. The lower traces show the corresponding simulations, where the packets containing the synchronous molecule have been shaded. The simulated free-flight TOF profile has been scaled up by a factor two.

behind the nozzle and an about 8 % reduced detection efficiency for the focused and decelerated molecules. No bias voltage was used. An optimum signal intensity was achieved at a stagnation pressure of 1.2 bar. For each experimental trace 1500 experiments have been averaged. The parameters of the simulations are: an initial beam velocity of 382 m/s, a velocity spread of $\Delta v_z = 25$ m/s, and a time width of $\Delta t = 150\,\mu$s. The other parameters are the same as for the simulations for benzonitrile seeded in xenon. The delay time between the trigger signal and the opening of the nozzle depends on the stagnation pressure, and is 0.338 ms here, which has been subtracted from the measurements.

In figure 6.11, it is seen that for the decelerated synchronous packets the intensity decreases stronger than expected from the simulations. The optimum experimental focusing length in all measurements is $f = 5.0$ mm, but the simulations predict an optimum focusing length of $f = 6.0$ mm due to the higher beam velocity. In these early measurements, the interpretation of the different peaks in the TOF profiles was not fully understood. Therefore, the focusing lengths and the delay times have not been optimized properly. Furthermore, due to alignment difficulties, the skimmer was off-axis when the measurements were performed. These experimental difficulties explain the mismatch in the intensities of the simulated and measured TOF profiles for the deceleration measurements. If the deceleration measurements of benzonitrile seeded in krypton were repeated with optimum parameters in the current setup, a better agreement between measurements and simulation would be expected.

In conclusion, the use of krypton as seed gas has the advantage of higher beam intensities and a stronger enhanced focusing signal. Therefore, it can be used for first focusing and deceleration measurements in a longer decelerator setup. Because of the higher initial beam velocity, more stages are needed to decelerate benzonitrile seeded in krypton to the same final velocity as benzonitrile seeded in xenon. Thus, for the deceleration to low velocities, xenon is preferred. Benzonitrile has also been seeded in 2.3 bar of argon, resulting in a beam velocity of about 540 m/s. Small focusing effects have been observed, when high voltages with a focusing length of $f = 8$ mm have been applied to the decelerator.

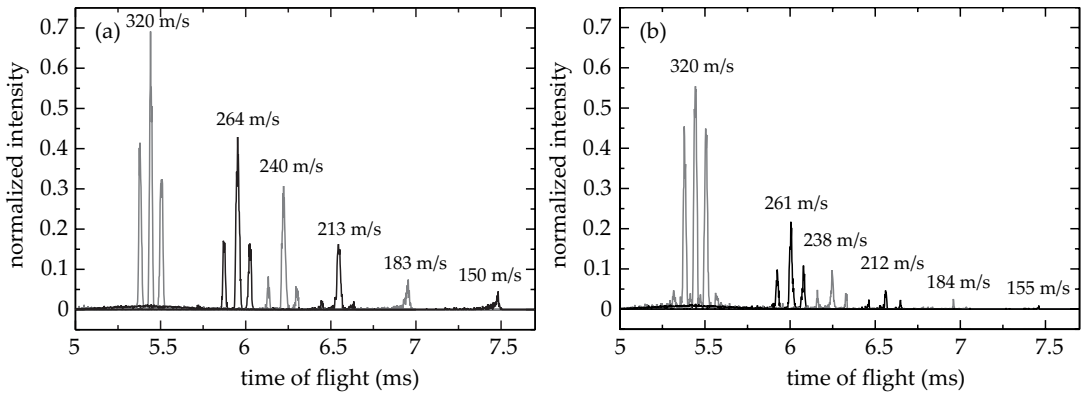

Figure 6.12: Simulations of TOF profiles for the alternating-gradient deceleration of benzonitrile in the 0_{00} state from 320 m/s to the indicated lower final velocities, using a decelerator consisting of 81 electrode pairs. (a) shows an arrangement, where the focusing direction is rotated after two and (b) after three AG lenses by 90°. The intensity is normalized on the intensity for guiding of molecules in the AG decelerator consisting out of 27 AG lenses. During the deceleration process, the focusing lengths have been decreased. See text for details.

6.7 An extended alternating-gradient decelerator

In figure 6.12, simulations for the 0_{00} state of benzonitrile are shown for an AG decelerator consisting of 81 electrode stages. The electrodes have the same geometry as used in the setup described before. In the simulations in figure 6.12(a), the focusing direction is rotated after two AG lenses, corresponding to a $(FO)\cdot((DO)^2(FO)^2)^{40}$ grid (two-electrode pattern), and in figure 6.12(b) after three AG lenses, corresponding to a $(FO)((DO)^3(FO)^3)^{13}(DO)^2$ grid (three-electrode pattern). The intensity of the TOF profiles in both graphs is normalized on the peak intensity for optimum focusing of molecules in the AG decelerator consisting of 27 AG lenses. It is seen that for the two-electrode pattern the molecules can be decelerated with larger intensities to lower velocities compared to the three-electrode pattern. While the free-flight intensity is strongly decreased by a factor of 15 for the longer setup, the integrated intensity for optimum focusing is still 51 % of the integrated intensity in the short decelerator. This relatively small reduction of the intensity for both the two-electrode pattern and for the three-electrode pattern is due to the phase stability of the AG decelerator [106]. The simulations are calculated for an ideal decelerator without misalignment effects. If a random misalignment with a standard deviation of $m = 50\,\mu$m is assumed (which should be realistic, because the alignment of the electrodes has

final velocity	f_{max}	f_{min}	d	normalized integrated intensity
(a)				
320 m/s	8.0 mm	8.0 mm	-	0.51
264 m/s	8.0 mm	5.25 mm	4.5 mm	0.41
240 m/s	8.0 mm	3.75 mm	4.75 mm	0.30
213 m/s	8.0 mm	3.0 mm	5.0 mm	0.19
183 m/s	8.0 mm	2.0 mm	5.25 mm	0.08
150 m/s	8.0 mm	2.0 mm	5.5 mm	0.06
(b)				
320 m/s	4.5 mm	4.5 mm	-	0.51
261 m/s	4.5 mm	3.0 mm	4.5 mm	0.18
238 m/s	4.5 mm	2.25 mm	4.75 mm	0.07
212 m/s	4.5 mm	2.0 mm	5.0 mm	0.03
184 m/s	4.5 mm	1.75 mm	5.25 mm	0.001
155 m/s	4.5 mm	1.25 mm	5.5 mm	0.0003

Table 6.3: Switching sequence parameters and integrated intensity for the synchronous packet for (a) the two-electrode and (b) three-electrode pattern for the simulations shown in figure 6.12. The initial velocity is 320 m/s. For direct comparison, the integrated intensity is normalized on the integrated intensity for optimum focusing for the short decelerator. The focusing length is varied quadratically between f_{max} and f_{min}. See text for details.

been improved for the newly setup decelerator modules), an overall scaling factor between measurements and simulations of 25 will be expected. Therefore, deceleration experiments in an extended setup with a two-electrode pattern should be feasible.

The simulations presented in figure 6.12 are performed for reasonable d values, as used for the deceleration measurements for the short setup (see section 6.4). In the long setup, the decelerated beam is completely separated from the free-flight beam using $d = 4.75$ mm. In the decelerator with the two-electrode pattern, benzonitrile can be decelerated for $d = 5.0$ mm from 320 m/s to 212 m/s with a normalized integrated intensity of 0.19 for the synchronous packet. For $d = 5.5$ mm, the molecules are decelerated to 150 m/s, corresponding to a reduction of the kinetic energy of 78 %, the synchronous packet has a normalized intensity of 0.06. The integrated intensities together with the parameters of the simulations are listed in table 6.3. In a decelerator with a three-electrode pattern, benzonitrile is less efficiently decelerated, due to

an over-focusing of the molecules especially at low velocities. For $d = 5.0$ mm, the molecules are decelerated from 320 m/s to 212 m/s, and the synchronous packet has a normalized intensity of only 0.031. For larger d values, almost no intensity is left. The integrated intensities of the synchronous packet are comparable for the two-electrode patterns: For the two-electrode pattern, the peak intensity is larger, but the synchronous peak is narrower than for the three-electrode pattern. However, for deceleration the acceptance for the synchronous packet is much higher for the two-electrode pattern. In a two-electrode pattern, the non-synchronous peaks experience only half the amount of focusing than the synchronous peak, but 2/3 of the focusing for the three-electrode pattern. Therefore, the non-synchronous packets are better accepted for the three-electrode pattern. Non-synchronous packets are a disadvantage, because for clean experiments with decelerated molecules, only one molecular packet is wanted.

The switching scheme used for the calculations for the longer AG decelerator, is similar to the one discussed before for the focusing and deceleration of molecules in hfs states. In particular, the parameter d and, therefore, the amount of kinetic energy removed per stage, remains constant. The amount of transverse focusing should also remain constant over the decelerator, and the molecules should spend the same time in the focusing field for all stages. In the experiments presented in section 6.4, the velocity changes have been relatively small and a constant focusing length f could be used. In the longer decelerator, the molecules are decelerated to much lower velocities. Therefore, the focusing parameter f has to be reduced over the course of the decelerator to compensate for the velocity changes. If one assumes that the energy removed per lens is small compared to the total kinetic energy of the molecule, the velocity changes quadratically with the number of electric field stages. Therefore, the actual focusing length f_n for the AG lens n is changed quadratically over the deceleration process

$$f_n = f_{\max} - n^2 \cdot \frac{f_{\max} - f_{\min}}{(n_{\text{total}} - 1)^2}\,, \tag{6.1}$$

where the total number of electrode stages is $n_{\text{total}} = 81$. In table 6.3, the maximum and minimum focusing lengths $f_{\max}$ and $f_{\min}$ are listed, which are optimized for a maximum intensity for the synchronous peak. Switching sequences with (in first order) linear changes of the focusing lengths have been used in the deceleration experiments on OH in a lfs state, and a 20 % increased signal compared to switching sequences with constant focusing lengths has been observed (see chapter 7.4).

Based on the simulations discussed above, we are currently extending the AG decelerator to 81 deceleration stages using refined mechanical alignment procedures and the improved lens pattern, where we rotate the focusing direction every two stages. With this setup, we expect to be able to decelerate benzonitrile molecules from 320 m/s to 150 m/s with reasonable intensities. For the deceleration to even lower velocities, hyperbolically shaped electrodes or the asymmetric four-electrode configuration (see chapter 3.3) will be used. At low velocities, the focusing direction is rotated every stage. It could also be necessary to reduce the length and/or the voltage for the last electrode stages to avoid over-focusing of the molecules. After the molecules will have been decelerated to about 20 m/s in an extended AG decelerator setup, three-dimensional confinement will be possible. For instance, AC electric traps can be used, in which the very same principles of dynamic focusing as in the AG decelerator are employed [78, 108, 109, 187].

6.8 Conclusions

In conclusion, AG focusing and deceleration of benzonitrile in multiple quantum states have been demonstrated. The focusing properties for benzonitrile have been studied in three different low-lying rotational states, namely the absolute ground state 0_{00} as well as the rotationally excited states 1_{01} and 4_{04}. Benzonitrile has been decelerated in its absolute ground state 0_{00} from 320 m/s to about 275 m/s, and similar changes in velocity have been obtained for rotationally excited states. All measurements agree well with the outcome of trajectory calculations. If desired, in an AG decelerator different rotational states with similar Stark shifts can be decelerated simultaneously, albeit with different acceptances. This demonstrates that alternating-gradient focusing and deceleration can be performed for large asymmetric top molecules, in order to produce cold, slow samples thereof. This vastly extends the range of species which motion and orientation can be precisely controlled. Furthermore, phase space acceptances for focused and decelerated molecules and the prospects of using krypton as a carrier gas instead of xenon, have been discussed, in this chapter. Currently, we are extending the AG decelerator setup, in order to decelerate benzonitrile to velocities slow enough to directly load them into an AC trap.

Chapter 7

Alternating-gradient focusing and deceleration of OH radicals

7.1 Introduction

In this chapter, the alternating-gradient focusing and deceleration of OH radicals in both the low-field-seeking and high-field-seeking levels of the rovibronic $X^2\Pi_{3/2}, v = 0, J = 3/2$ ground state are demonstrated using a single experimental setup. For the AG deceleration of OH in the hfs $X^2\Pi_{3/2}, v = 0, J = 3/2\, e$ state, the same switching scheme as for the deceleration of benzonitrile, presented in chapters 3.5 and 6.4, is employed. However, for the deceleration of molecules in the lfs $X^2\Pi_{3/2}, v = 0, J = 3/2\, f$ state, a different switching scheme has to be applied to achieve phase stability in all three dimensions (see chapter 3.5). In this switching scheme, the high voltage is switched on and off twice per AG lens.

Molecules in lfs states have been decelerated using a normal Stark decelerator [70]. The coupling of longitudinal and transverse motion in a normal Stark decelerator and its influence on the phase stability have been studied, and resonances similar to parametric oscillations in AC ion traps [188] and AC traps for neutral molecules [109, 187] have been observed [186]. Exploiting overtones in the Stark decelerator, the coupling can be changed, and improved transmission through the decelerator has been observed [186, 189]. In these experiments, only a fraction of the electric field stages is used for the deceleration, whereas the remaining ones are needed for an optimized transverse focusing.

Recently, new concepts for electrode geometries for a normal Stark decelerator using deceleration stages and quadrupole focusing stages have been proposed

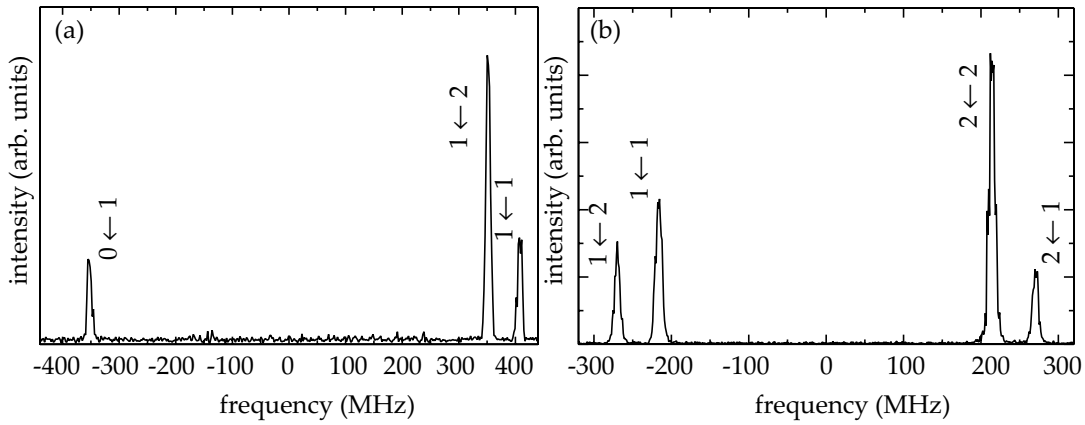

Figure 7.1: Hyperfine-resolved excitation spectrum of the (a) $P_1(1)$ transition $A^2\Sigma^+, v' = 1, J' = 1/2 \leftarrow X^2\Pi_{3/2}, v'' = 0, J'' = 3/2\, e$ and (b) $Q_1(1)$ transition $A^2\Sigma^+, v' = 1, J' = 3/2 \leftarrow X^2\Pi_{3/2}, v'' = 0, J'' = 3/2\, f$. The frequencies are given relative to the origins of the rotational transitions at (a) 35429.16 cm^{-1} and (b) 35461.50 cm^{-1} [124], respectively. The hyperfine transitions $F' \leftarrow F''$ are labelled.

in order to allow for the decoupling of transverse focusing and longitudinal manipulation of the molecular packet [190], but no experimental evidence for the improvement as a result of such electrode geometries has been given yet. The alternating-gradient focusing and deceleration of molecules in hfs states have been demonstrated using the AG decelerator [9, 13, 106] (see also chapter 6). In the following, it is demonstrated that an AG configuration can also be used for the focusing and deceleration of molecules in lfs states. Moreover, it allows to effectively circumvent the problems related to the inherent coupling of transverse and longitudinal motion in the Stark decelerator for molecules in lfs states.

7.2 Detection of OH

The experimental setup for the AG focusing and deceleration of OH is described in detail in chapter 4. The same AG decelerator as for the measurements on benzonitrile has been used, but the source has been modified to produce OH via photodissociation of HNO_3 with an excimer laser pulse. Compared to the benzonitrile experiments, this has the advantage that the initial molecular packet is narrow and well defined, when it enters the AG decelerator with an initial velocity of approximately 360 m/s.

OH is detected via LIF with an excitation wavelength of 282 nm. Fluorescence is predominantly around 313 nm (see chapter 4.6.2). The hyperfine-

resolved excitation spectra for the $P_1(1)$ transition $A^2\Sigma^+, v' = 1, J' = 1/2 \leftarrow X^2\Pi_{3/2}, v'' = 0, J'' = 3/2\,e$ and $Q_1(1)$ transition $A^2\Sigma^+, v' = 1, J' = 3/2 \leftarrow X^2\Pi_{3/2}, v'' = 0, J'' = 3/2\,f$ of OH are shown in figures 7.1(a) and (b), respectively. The splittings with a frequency of 55 MHz are due to the hyperfine splittings in the Λ-doublet components of the $X^2\Pi_{3/2}, v = 0, J = 3/2\,v = 0$ ground state [191]. The large splitting corresponds to the hyperfine spitting of the $A^2\Sigma^+, v = 1$ state and is 775.6 MHz for the $A^2\Sigma^+, v = 1, J = 1/2$ state and 490.0 MHz for the $A^2\Sigma^+, v = 1, J = 3/2$ state [192].

In all focusing and deceleration measurements of OH in its hfs $X^2\Pi_{3/2}, v = 0, J = 3/2\,e$ state, the $F' = 1 \leftarrow F'' = 2$ transition shown in figure 7.1(a) is used for detection. In an electric field, the $X^2\Pi_{3/2}, v = 0, J = 3/2\,e, F = 2$ state splits into the more polar $M\Omega = 9/4$ and the less polar $M\Omega = 3/4$ levels (see chapter 2.3.1), which are simultaneously detected. In the simulations, the appropriate weighting due to the number of hyperfine states belonging to these two manifolds is included, which is 40 % for $M\Omega = 9/4$ and 60 % for $M\Omega = 3/4$. OH in its lfs $^2\Pi_{3/2}, v = 0, J = 3/2\,f$ state is detected using the $F' = 2 \leftarrow F'' = 2$ transition shown in figure 7.1(b). For the lfs state, the appropriate weighting due to the number of hyperfine states is 80 % for $M\Omega = -9/4$ and 20 % for $M\Omega = -3/4$. In the AG decelerator, both the more polar and the less polar $M\Omega$ components are decelerated, although the switching sequences are optimized for the more polar level, which is therefore accepted with a higher efficiency.

7.3 Focusing and deceleration of OH in a high-field-seeking state

In figure 7.2, the focusing of OH in the hfs $X^2\Pi_{3/2}, v = 0, J = 3/2\,e$ state is demonstrated. The lowest traces show the free-flight TOF profiles. Since OH radicals are produced by photodissociation using an excimer laser pulse, the initial position and time width of the molecular packet is well defined when it enters the AG decelerator. This results in a sharp synchronous peak around 1.85 ms in the measured TOF profiles and simplifies the interpretation of the deceleration measurements, which are presented later. For all focusing and deceleration TOF profiles shown in this chapter, 8000 single measurements are averaged, corresponding to a measuring time of approximately 7 min at a 20 Hz repetition rate. The optimum experimental and simulated focusing traces are scaled such that they have about the same intensity. Compared to all other traces, the simulated free-flight TOF profile (lowest trace) needs to be scaled up by a factor of ten. The scaling factor can be attributed to misalignment of the

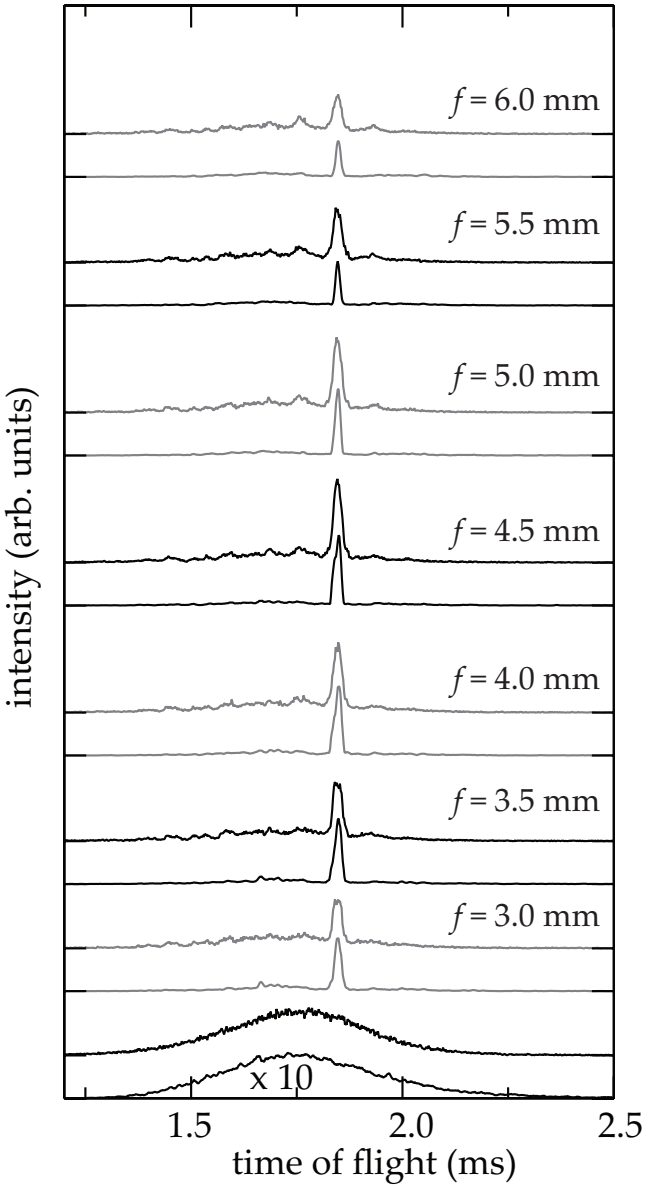

Figure 7.2: Focusing sequence of OH in the high-field-seeking $X^2\Pi_{3/2}, v = 0, J = 3/2\, e$ state at a velocity of 355 m/s, with the simulated time-of-flight profiles shown underneath the experimental measurements for different focusing lengths f, as indicated.

measurements	v_{z_0}	Δv_{z_1}	Δv_{z_2}	Δt_1	Δt_2
hfs focusing (figure 7.2)	363 m/s	110 m/s	70 m/s	400 ms	124 μs
hfs deceleration (figure 7.3)	365 m/s	120 m/s	70 m/s	420 ms	122 μs
lfs focusing and bunching (figure 7.4)	360 m/s	120 m/s	70 m/s	440 ms	125 μs
lfs deceleration from 345 m/s (figure 7.5)	350 m/s	120 m/s	70 m/s	440 ms	125 μs
lfs deceleration from 305 m/s (figure 7.8)	330 m/s	120 m/s	70 m/s	620 ms	138 μs

Table 7.1: Parameters used in the simulations and delay times used for the measurements of the AG focusing and deceleration of OH. Listed are the initial longitudinal beam velocity v_{z_0}, the FWHM of a bi-Gaussian distribution Δv_{z_1} and Δv_{z_2}, the delay time of the trigger for the excimer laser relative to the trigger of the nozzle Δt_1, and the delay time between the trigger for the excimer laser and the trigger for the start of the switching sequence Δt_2. See text for details.

electrodes, as discussed in the following section. The overall focusing behavior is similar to the focusing behavior of benzonitrile (see chapter 6.3). The optimum focusing length is $f = 4.5$ mm, where the peak intensity is enhanced by 90 % compared to the free-flight intensity.

A bias voltage of ± 300 V is used for all focusing and deceleration measurements in this chapter. For each measurement sequence, the delay time between the trigger signal of the excimer laser and the trigger for the nozzle Δt_1 as well as the delay time between the trigger for the excimer laser and the trigger for the start of the switching sequence Δt_2 are optimized. The optimum parameters and the beam velocity depend on the stagnation pressure and opening time of the nozzle. By choosing a larger Δt_1, a slower part of the HNO_3 exiting the nozzle is dissociated, resulting in a reduced mean velocity of the OH beam. This is utilized for the deceleration of OH in the lfs state starting from 305 m/s presented later. Δt_2 is optimized to obtain a maximum enhancement of the focused signal compared to the free-flight signal at a certain velocity. Because the free-flight TOF profile cannot be described properly by a Gaussian distribution, a bi-Gaussian distribution was used for the simulations. The bi-Gaussian distribution has the FWHM Δv_{z_1} and Δv_{z_2}, where Δv_{z_2} is smaller than Δv_{z_1}. The beam parameters and delay times for the focusing and deceleration measurements shown in this chapter are given in table 7.1. The distribution with a FWHM Δv_{z_2} contributes to the bi-Gaussian distribution with 30 %. For the

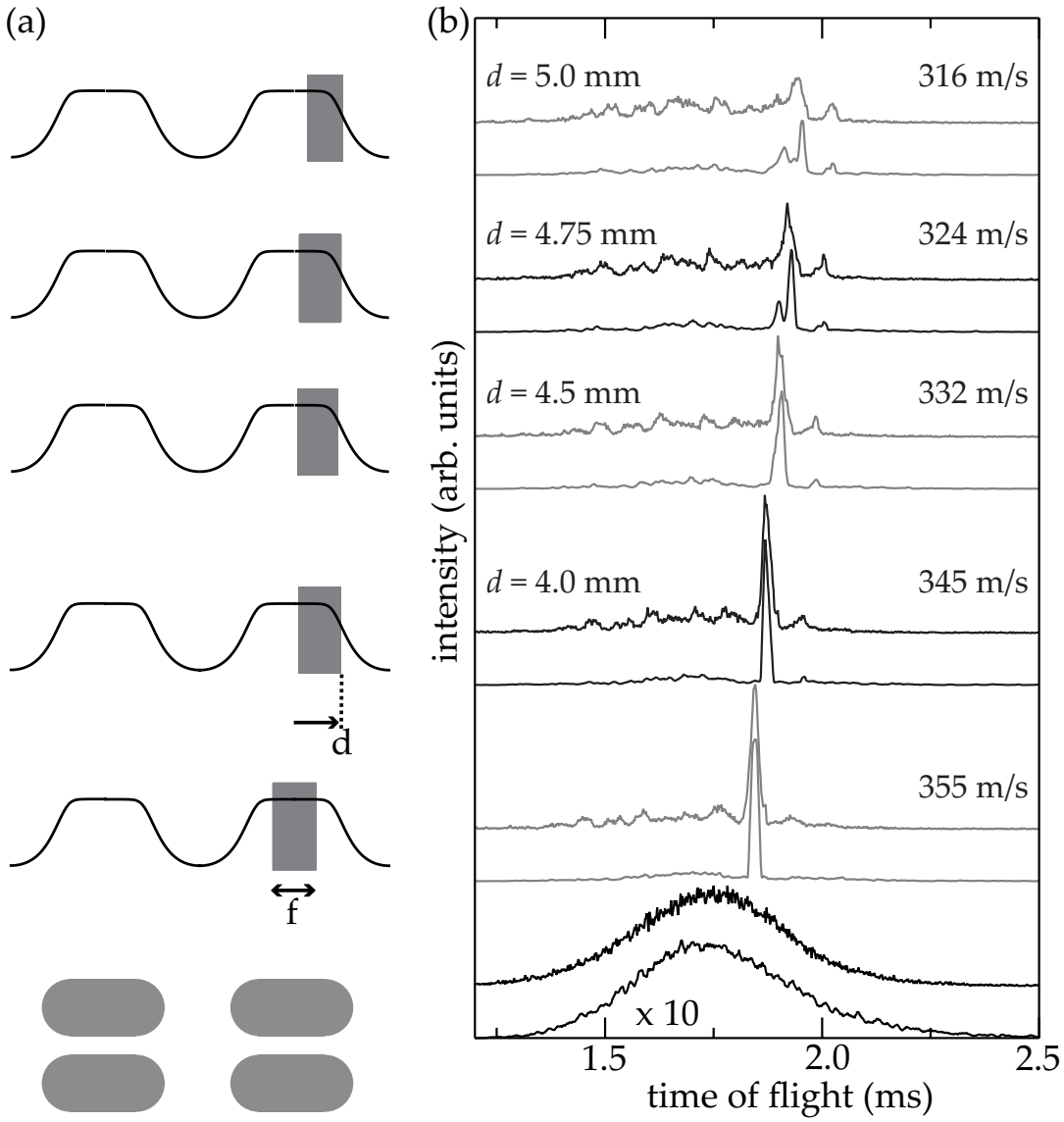

Figure 7.3: (a) Graphical representations of the high voltage switching parameters d and f. (b) Deceleration sequence for OH in its high-field-seeking $X^2\Pi_{3/2}, v = 0, J = 3/2\, e$ state with the simulated time-of-flight profiles shown underneath the experimental measurements for different focusing and deceleration parameters. The lowest traces are free-flight profiles. The second (grey) traces show the arrival time distribution for transverse focusing at a constant velocity of 355 m/s. The other traces are TOF profiles for deceleration from 355 m/s to successively slower final velocities, as indicated.

transverse velocity spread, a FWHM of $\Delta v_x = \Delta v_y = 36$ m/s and for the initial molecular packet a size of $\Delta x = \Delta y = \Delta z = 2$ mm are assumed. For the free-flight simulations, $5 \cdot 10^7$ trajectories and for the focusing and deceleration measurements $1 \cdot 10^7$ trajectories have been calculated.

For the deceleration of packets of OH radicals in the hfs $X^2\Pi_{3/2}, v = 0, J = 3/2\, e$ state, the same switching scheme and similar d values as for benzonitrile are used (see chapter 3.5), as indicated by the shaded areas in figure 7.3(a). Due to the larger initial beam velocity of OH compared to benzonitrile, the final velocities are larger as well. The deceleration measurements and the corresponding simulations are presented in figure 7.3(b). The lowest traces show free-flight TOF profiles, the second two (grey) traces optimum focusing using $f = 4.5$ mm at a velocity of 355 m/s, and all other traces the deceleration to successively slower final velocities. For $d = 4$ mm, the packet is decelerated from 355 m/s to 345 m/s, for example. For the strongest deceleration to 316 m/s using $d = 5$ mm, the kinetic energy of the molecules is reduced by 21 %, resulting in a shift of the arrival time of the synchronous peak from 1.85 m/s to 1.95 ms. The optimum focusing length is $f = 4.25$ mm for the deceleration to 345 m/s, 332 ms, and 324 m/s. For the deceleration to 316 m/s, it is $f = 3.75$ mm. The background structure in the TOF profiles originates mainly from the weak focusing $M\Omega = 3/4$ component, but also from the $M\Omega = 9/4$ component. Not all features of in the background of the simulations are reproduced probably, as this is for the weak focusing component more difficult. However, some features, for instance, peaks with a later arrival time than the synchronous peak which originate from the $M\Omega = 9/4$ component are well reproduced by the simulations (see also section 7.4). The molecules in this peak are lost from the synchronous packet during the deceleration process and arrive one electrode stage behind when the synchronous packet arrives at the detector, as can be seen from trajectory simulations and from the phase space distribution (see also section 7.5).

7.4 Focusing and deceleration of OH in a low-field-seeking state

For the focusing and deceleration of OH is its lfs $X^2\Pi_{3/2}, v = 0, J = 3/2\, f$ state, the double switching scheme described in chapter 3.5 is used. Additional to the focusing at the center of the AG lens, the high voltage is switched on and off once more, when the synchronous molecule is in between two AG lenses. This allows to longitudinally bunch the molecular packet. Figures 7.4(a) and (b) show TOF profiles at a velocity of 345 m/s for different focusing lengths f using a constant

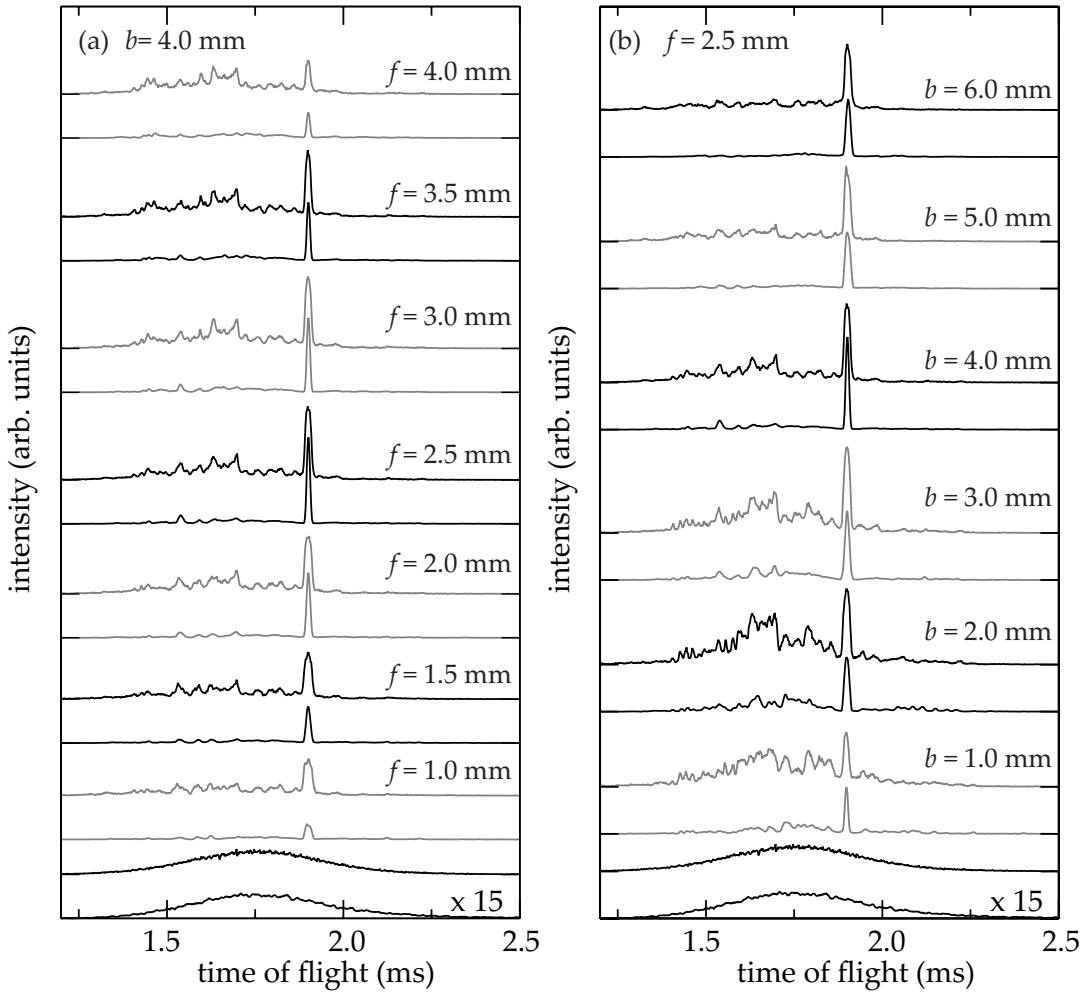

Figure 7.4: (a) Focusing and (b) bunching sequences of OH in its low-field-seeking $X^2\Pi_{3/2}, v = 0, J = 3/2\, f$ state, with the simulated time-of-flight profiles shown underneath the experimental measurements. The focusing length f and bunching length b are indicated. The lowest traces are free-flight TOF profiles.

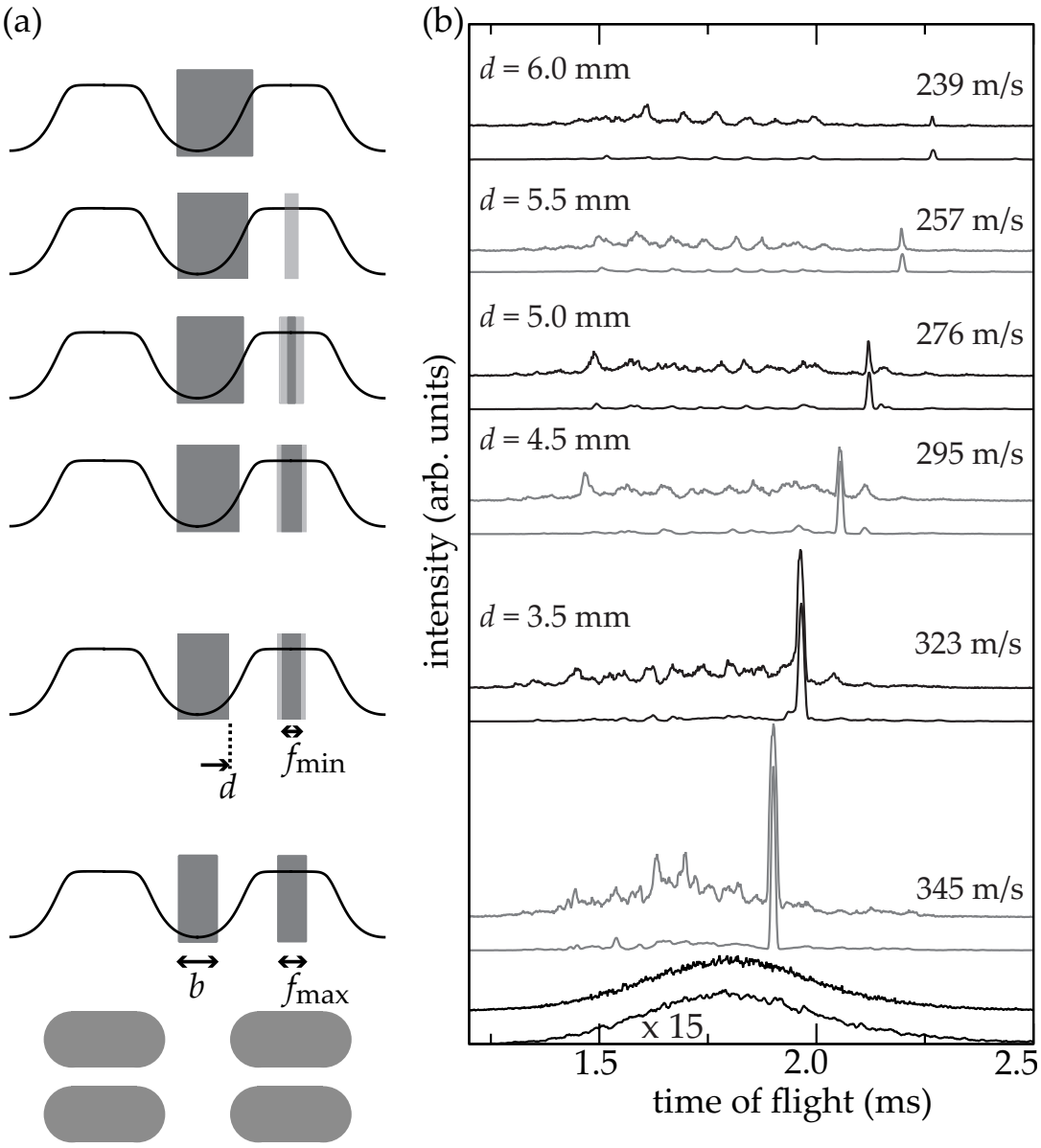

Figure 7.5: (a) Graphical representations of the high voltage switching parameters b, d, $f_{\max}$, and $f_{\min}$. (b) Deceleration sequence for OH in its low-field-seeking $X^2\Pi_{3/2}, v = 0, J = 3/2\, f$ state, with the simulated time-of-flight profiles underneath the experimental measurements for different focusing and deceleration parameters. The lowest traces are free-flight profiles. The second (grey) traces show the arrival time distribution for transverse focusing at a constant velocity of 345 m/s. The other traces are TOF profiles for deceleration from 345 m/s to successively slower final velocities, as indicated.

bunching length b and for different values of b for constant f, respectively. The optimum parameters are $f = 2.5$ mm or 3.0 mm and $b = 4.0$ mm. Without the second switching step ($b = 0$ mm (not shown)), for molecules in lfs states almost no longitudinal bunching is achieved, and the intensity of the synchronous peak in the TOF profiles is 75 % lower than for optimum bunching. The measurements agree well with the simulations, when the simulated free-flight trace is scaled up by a factor fifteen. For optimum focusing and bunching parameters, the focusing intensity is three times larger than the free-flight intensity.

The experimental results for the deceleration of OH in its lfs $X^2\Pi_{3/2}, v = 0, J = 3/2\, f$ state are shown in figure 7.5(b) together with their corresponding simulations. For the topmost trace, the molecules are decelerated from 345 m/s to 239 m/s. For molecules in lfs states the transverse focusing forces are larger than the defocusing forces, which is opposite for molecules in hfs states (see chapter 3.3). Furthermore, due to the double switching scheme, a better decoupling of the transverse and longitudinal motion as for molecule in the hfs states is possible, and the amount of transverse focusing and longitudinal bunching can be adjusted almost independently. Therefore, molecules in lfs states, compared to molecules in hfs states, are decelerated to lower velocities in the same experimental setup, removing more than 50 % of the kinetic energy.

As a typical example, the contributions of the different $M\Omega$ components to the TOF profiles for the deceleration of OH from 345 m/s to 276 m/s are depicted in figure 7.6. Below the experimental curve (topmost trace), the corresponding simulations and the individual contributions of the $M\Omega$ = -3/4 component, the $M\Omega$ = -9/4 component, and the combined simulation for both $M\Omega$ components are shown. In all other simulated TOF profiles of this chapter, the combined simulations for both $M\Omega$ components are given. The synchronous peak at 2.12 ms as well as the non-synchronous peak at 1.49 ms originate from the $M\Omega$ = -9/4 component. The molecules in the non-synchronous peak at 1.49 ms have a initial mean velocity of 438 m/s and are longitudinally bunched at this velocity. The other non-synchronous peaks, especially the one with the late arrival time of 2.15 ms, originate from the $M\Omega$ = -3/4 component. Also the non-synchronous peaks in the measurements are reproduced by the deceleration simulations. For some focusing and bunching measurements the exact reproduction of the non-synchronous peaks is more difficult (see figure 7.4). Due to misalignment effects, the non-synchronous peaks in all measurements have a higher intensity than the non-synchronous peaks in the simulations. This is probably, because the $M\Omega$ = -3/4 component is transversely less focused and defocused.

As already discussed in chapter 6.7, the focusing length f should be reduced

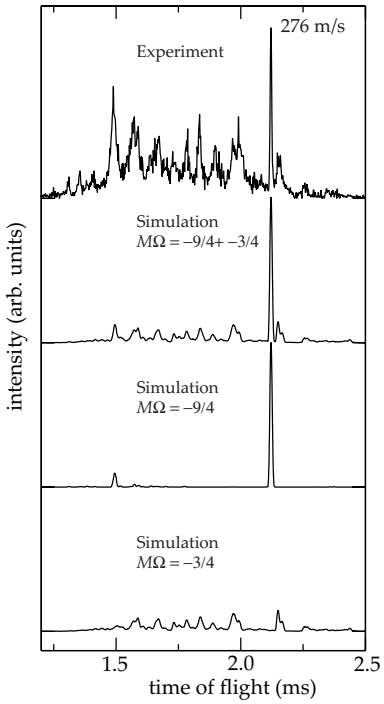

Figure 7.6: Upper trace: measurement for the deceleration of the low-field-seeking $X^2\Pi_{3/2}, v = 0, J = 3/2\, f$ state from 345 m/s to 276 m/s. Lower traces: simulations for the individual contributions of the $M\Omega$ = -3/4 component, the $M\Omega$ = -9/4 component, and the combined simulation.

quadratically along the decelerator, when significant changes in the velocity are achieved in order to avoid an over-focusing. For the deceleration of OH in the lfs state, this has been accounted for in first order, by reducing the focusing lengths f_n in the AG lens n linearly over the deceleration process:

$$f_n = f_{\max} - n \cdot \frac{f_{\max} - f_{\min}}{n_{\text{total}} - 1}\,, \tag{7.1}$$

where $f_{\max}$ is the maximum focusing length, $f_{\min}$ the minimum focusing length, and $n_{\text{total}} = 27$ the total number of electrode stages. The variation of f is depicted in the graphical representation of the switching scheme by the shaded areas in figure 7.5 (a). The linear change of the focusing length results in an enhancement of the synchronous peak of up to 20 % compared to the optimum measurement using a constant f. This is demonstrated in figure 7.7 for the deceleration from 345 m/s to 276 m/s. The focusing parameters are optimized for every time sequence and listed in table 7.2. For a small deceleration, f stays nearly constant and the focusing length is only decreased by 1 mm during the deceleration process. For the largest deceleration to 239 m/s using $d = 6.0$ mm,

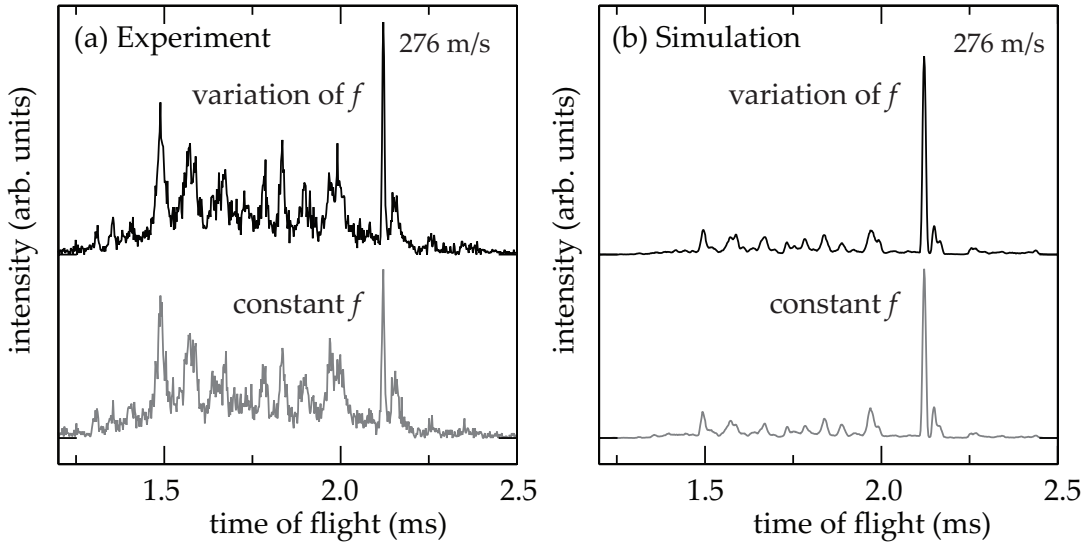

Figure 7.7: (a) measured and (b) simulated TOF profiles for the deceleration of OH in its low-field-seeking $X^2\Pi_{3/2}, v = 0, J = 3/2\, f$ state from 345 m/s to 276 m/s. The black traces show results for a variation of the focusing length f over the length of the decelerator, while the grey traces are obtained for the optimum constant focusing length.

initial velocity	final velocity	$f_{\max}$	$f_{\min}$	b	d
(a)					
345 m/s	345 m/s	3.0 mm	3.0 mm	4.0 mm	-
345 m/s	323 m/s	3.0 mm	2.0 mm	5.5 mm	3.5 mm
345 m/s	295 m/s	3.0 mm	2.0 mm	6.5 mm	4.5 mm
345 m/s	276 m/s	2.5 mm	0.75 mm	7.0 mm	5.0 mm
345 m/s	257 m/s	1.5 mm	0.0 mm	7.5 mm	5.5 mm
345 m/s	239 m/s	0.0 mm	0.0 mm	8.0 mm	6.0 mm
(b)					
305 m/s	305 m/s	2.25 mm	2.25 mm	4.0 mm	-
305 m/s	280 m/s	2.25 mm	1.5 mm	5.5 mm	3.5 mm
305 m/s	247 m/s	2.25 mm	0.5 mm	6.5 mm	4.5 mm
305 m/s	224 m/s	1.75 mm	0.25 mm	7.0 mm	5.0 mm
305 m/s	200 m/s	0.75 mm	0.0 mm	7.5 mm	5.5 mm

Table 7.2: Switching sequence parameters $f_{\max}$, $f_{\min}$, b, and d for the measurements and simulations for deceleration of OH in its low-field-seeking state from (a) 345 m/s and (b) 305 m/s shown in figures 7.5 and 7.8, respectively. The focusing length is varied linearly between $f_{\max}$ and $f_{\min}$. See text for details.

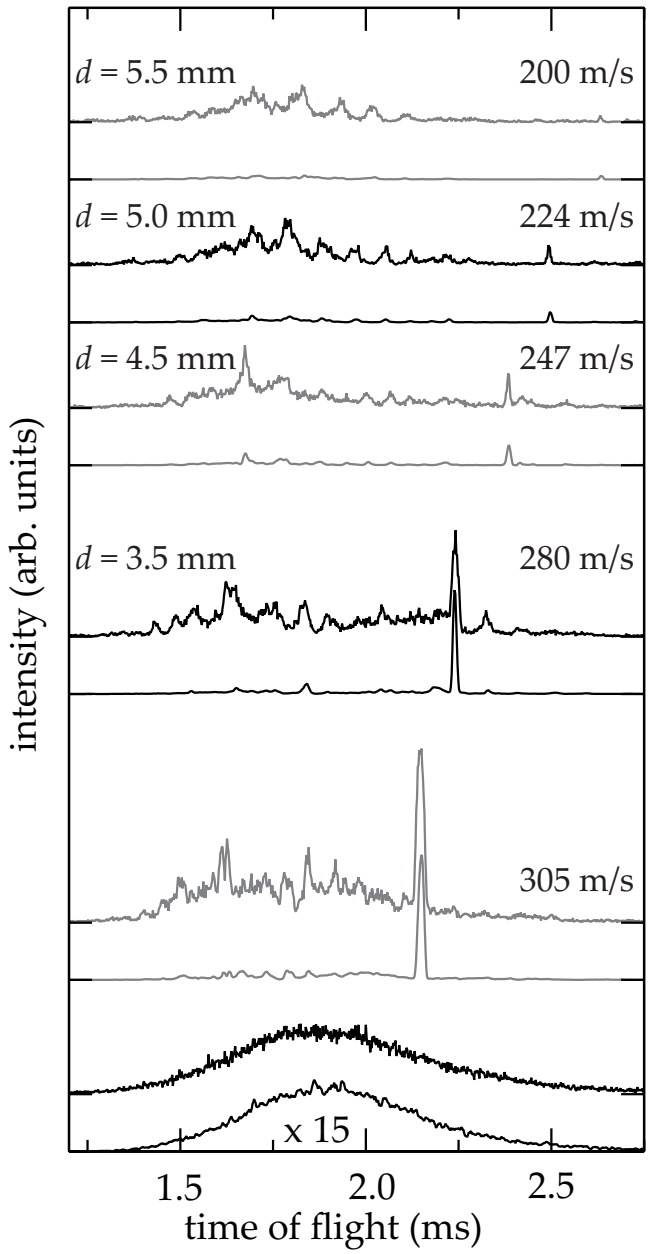

Figure 7.8: Deceleration sequence for OH in its low-field-seeking $X^2\Pi_{3/2}, v = 0, J = 3/2\, f$ starting from 305 m/s, with the simulated time-of-flight profiles shown underneath the experimental measurements for different focusing and deceleration parameters. The lowest traces are free-flight profiles. The second (grey) traces show the arrival time distribution for transverse focusing at a constant velocity of 305 m/s. The following traces are TOFs for deceleration from 305 m/s to successively slower final velocities, as indicated.

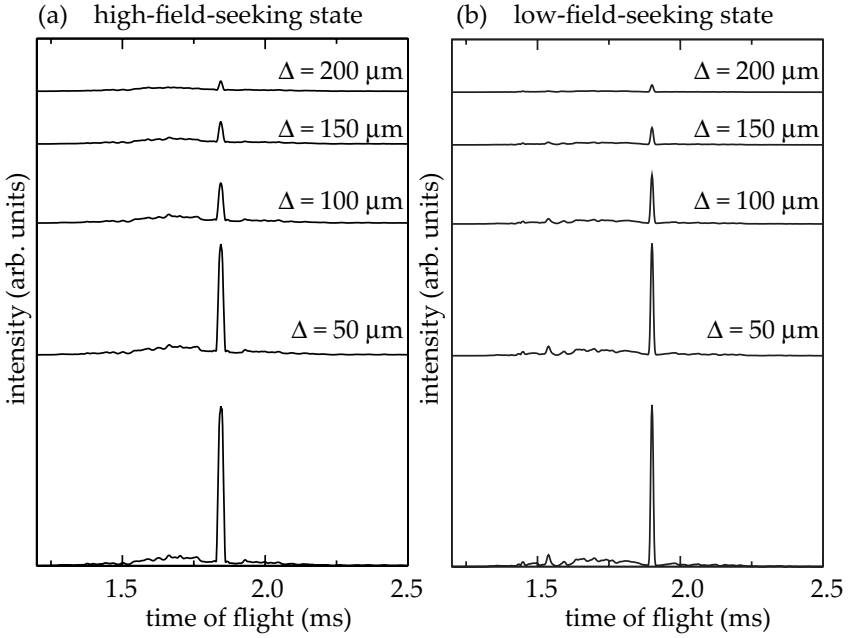

Figure 7.9: Influence of misalignment for optimum focusing at 355 m/s for the (a) high-field-seeking $X^2\Pi_{3/2}, v = 0, J = 3/2\, e$ state and (b) for optimum focusing and bunching at 345 m/s for the low-field-seeking $X^2\Pi_{3/2}, v = 0, J = 3/2\, f$ state for three-dimensional electrode displacements randomly chosen from a Gaussian distribution with standard deviation Δ.

the electric field is switched on and off only once in between the electrodes, because the amount of transverse focusing along the rising slope of the electric field is already sufficient. An additional transverse focusing would over-focus the molecules, resulting in a decreased intensity of the synchronous peak.

In additional experiments presented in figure 7.8, OH in the lfs state is decelerated from 305 m/s to 200 m/s, the lowest velocity obtained for molecular packets in an AG decelerator so far. In order to achieve this low velocity with the same experimental setup, a longer excimer delay time Δt_1 has been chosen such that a slower part of the HNO_3 exiting the nozzle is dissociated, resulting in a slower molecular beam with an initial mean velocity of 330 m/s. By optimizing the delay time Δt_2 between the trigger for the excimer laser and the trigger for the switching sequence, a focused synchronous peak at a velocity of 305 m/s is obtained, which is decelerated to lower velocities. The switching parameters are also listed in table 7.2.

The intensity ratios and arrival times of all measurements with switched

electric fields applied match the simulations very well. However, the simulations predict a considerably larger intensity of the synchronous peaks of the focused and decelerated TOF profiles compared to the free-flight measurements than observed experimentally. As has been already discussed for benzonitrile (see chapter 6.3), this can be attributed to mechanical misalignments of the electrodes. The simulated decrease of the intensity for an increased random displacement of electrode pairs with a standard deviation Δ is shown in figure 7.9. The scaling factor of ten can be understood by a mechanical misalignment of about ± 150 μm, which is larger than that predicted from the misalignment simulations for benzonitrile. One possible explanation may be that the decrease in intensity compared to the simulations is not only due to the displacements of the electrode stages but also partly due to frequency shifts in the detection. The following effect has been observed. A shift of 4 MHz of the optimum detection frequency for the focused and decelerated molecules compared to the free-flight TOF profiles is observed and considered in the detection. This shift is of opposite sign for molecules in lfs and hfs states. A misalignment of the single electrodes in the last electrode stage would deflect the molecular beam towards or away from the detection laser, resulting in a frequency shift due to the Doppler effect. The Doppler effect is included in the simulations for an ideal decelerator without misalignment only. Since the natural linewidth of benzonitrile is with 8 MHz [159] much larger compared to the 204 kHz for OH [193], the frequency shift has not been observed for benzonitrile, and could partly explain the decreased detected intensity in the synchronous peak for focused and decelerated molecules. The simulations for OH yield the same scaling factor for the hfs and lfs state, but the measurements in the lfs state need to be scaled by an additional factor 1.5. This larger factor may be a consequence of the different high voltage switching schemes. As already discussed previously (see chapter 6.3), no misalignment effects of the individual electrodes in an electrode pair relative to each other are considered in the simulations. Because of the double switching scheme for OH in its lfs state, where the high voltages are also switched on and off in between two electrode pairs, the individual displacements of four neighboring electrodes relative to each other have to be considered. For molecules in hfs states, only the displacement in between one electrode pair has to be taken into account. Therefore, individual displacements of the electrodes could result in a stronger decrease of the intensity for molecules in lfs states, which could explain the larger scaling factor.

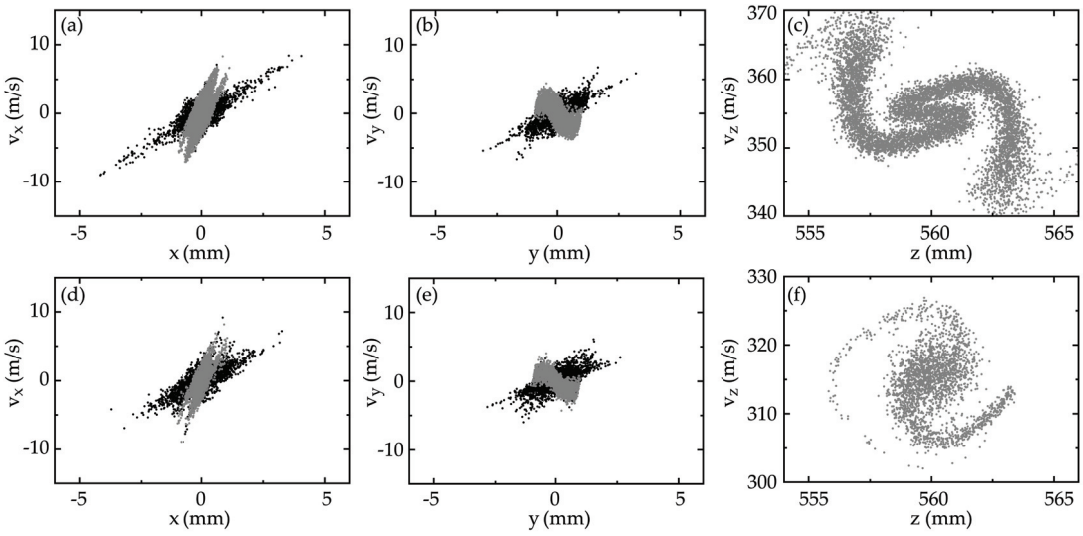

Figure 7.10: Simulated phase space distributions 20 mm behind the center of the last AG lens for the high-field-seeking ${}^2\Pi_{3/2}, v = 0, J = 3/2\,e$, $M\Omega = 9/4$ state of OH. (a), (b), and (c) show the two transverse and the longitudinal phase space distributions for focusing using $f = 4.5$ mm at 355 m/s, whereas (d), (e), and (f) show the distributions for deceleration from 355 m/s to 316 m/s. The grey phase space areas depict the molecules in the captured packet, whereas the black areas depict all other molecules which are not captured, but pass the decelerator on unstable or metastable trajectories. For the longitudinal distributions only the captured packets are shown.

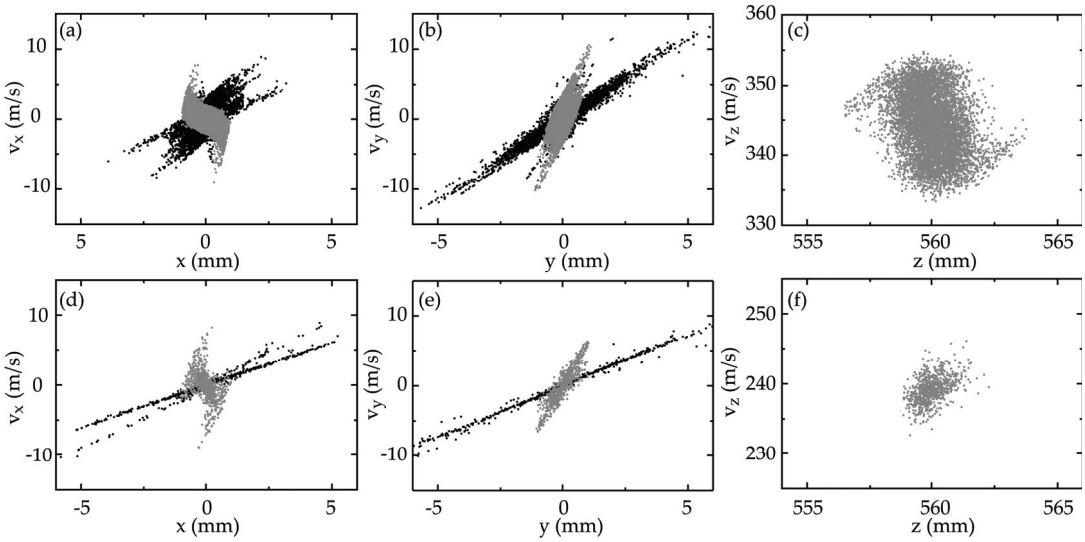

Figure 7.11: Simulated phase space distributions 20 mm behind the center of the last AG lens for the low-field-seeking $^2\Pi_{3/2}, v = 0, J = 3/2\, f$, $M\Omega = -9/4$ state of OH. (a), (b), and (c) show the two transverse and the longitudinal phase space distributions for focusing using $f = 3$ mm and $b = 4$ mm at 345 m/s, whereas (d), (e), and (f) show the distributions for deceleration from 345 m/s to 239 m/s. The grey phase space areas depict the molecules in the captured packet, whereas the black areas depict all other molecules which are not captured, but pass the decelerator on unstable or metastable trajectories. For the longitudinal distributions only the captured packets are shown.

7.5 Phase space distributions

Figures 7.10 and 7.11 show the phase space distributions obtained from trajectory simulations for the hfs $^2\Pi_{3/2}, v = 0, J = 3/2\,e$, $M\Omega = 9/4$ state and the lfs $^2\Pi_{3/2}, v = 0, J = 3/2\,f$, $M\Omega = -9/4$ state, respectively. As discussed in chapter 6.5, due to Liouville's theorem the phase space areas before and behind the decelerator stay constant. Therefore, only the phase space acceptances 20 mm behind the last AG lens of the decelerator are given. In figures 7.10(a), (b), and (c) the phase space distributions for the hfs state for optimum focusing at 355 m/s are shown, whereas figures 7.10(d), (e), and (f) show the distributions for the deceleration from 355 m/s to 316 m/s. The grey phase space areas depict the molecules in the captured packet. For focusing, the transverse acceptance is about 3.0 mm × m/s along the x-direction, about 4.5 mm × m/s along the y-direction, and the longitudinal distribution along the z-direction is about 49 mm × m/s. While the phase space acceptances for both transverse directions are similar to the ones discussed for benzonitrile, the phase space distribution along the z-direction for focusing (figure 7.10(c)) has not an ellipse but a helix shape. This is due to the narrow initial longitudinal position and time spread but large longitudinal velocity spread of the molecular packet. The longitudinal phase space acceptance is actually larger as seen from the distribution, but due to the initial conditions of the molecular packet, the phase space is not homogenously filled. From the helix shape it can be seen that the longitudinal bunching works best in the fringe fields of the electrodes, such that molecules in a wide velocity range are accepted. The six-dimensional phase space volume is 662 mm^3 × (m/s)^3. For the deceleration from 355 m/s to 316 m/s (see figure 7.10(d), (e), and (f)), the acceptances are about 1.8 mm × m/s along the x-direction, about 3.2 mm × m/s along the y-direction, and the phase space distribution along the z-direction is about 30 mm × m/s . This results in a six-dimensional volume of 173 mm^3 × (m/s)^3. As already described for benzonitrile, the phase space volume of accepted molecules for deceleration is smaller than for focusing.

In figures 7.11(a), (b), and (c), the phase space distributions for the lfs state for optimum focusing at 345 m/s are shown, whereas figures 7.11(d), (e), and (f) depict the distributions for the deceleration from 345 m/s to 239 m/s. For focusing, the transverse acceptance is about 7.5 mm × m/s along x, about 3.0 mm × m/s along y, and the longitudinal distribution is about 32 mm × m/s. The six-dimensional phase space volume is 720 mm^3 × (m/s)^3, which is slightly larger than for focusing of the hfs state. For the deceleration from 345 m/s to 239 m/s (see figure 7.10(d), (e), and (f)), the acceptances are about 2.0 mm × m/s along x, about 1.5 mm × m/s along y, and the longitudinal distribution is about

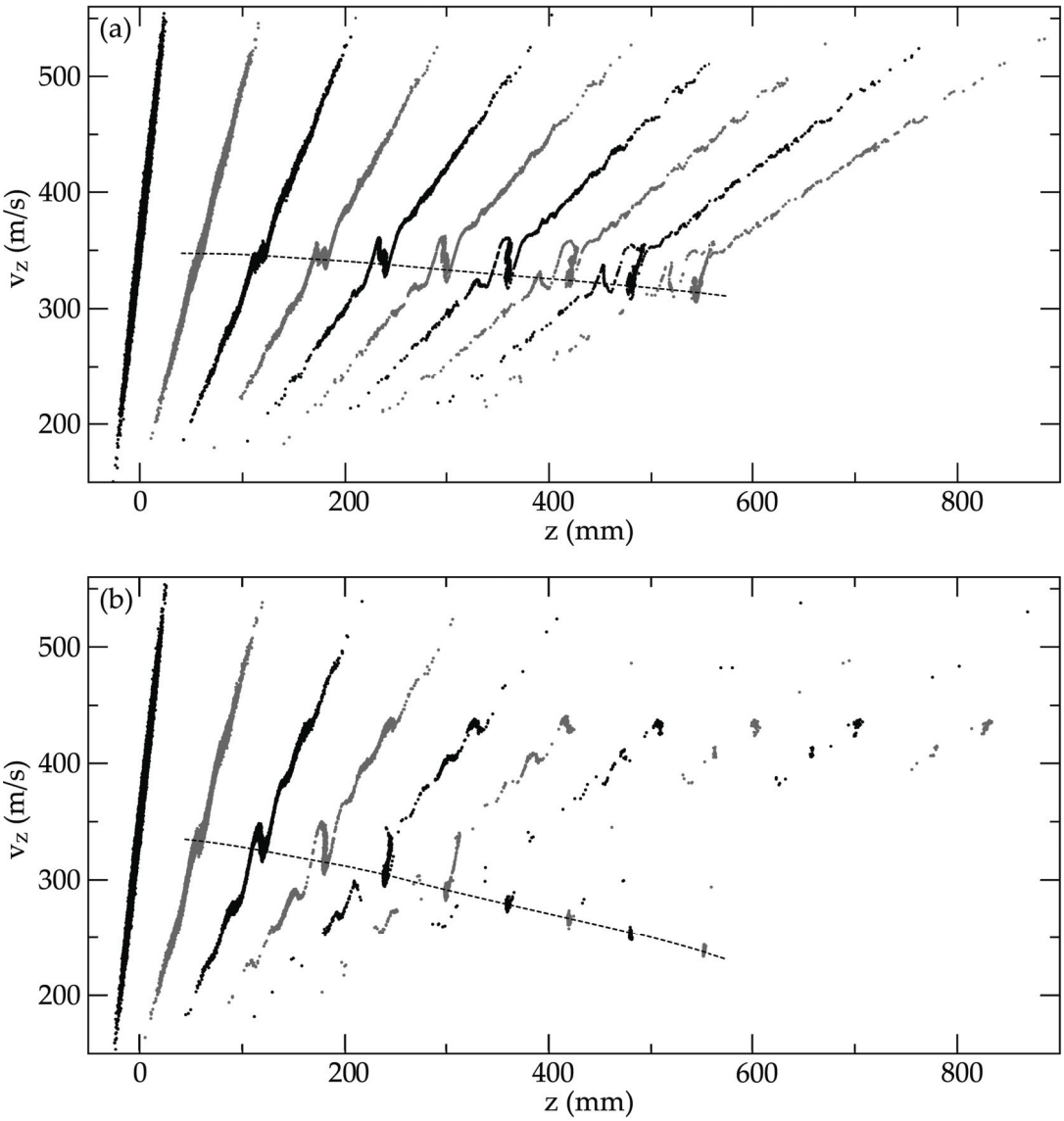

Figure 7.12: (a) Longitudinal phase space evolution for the deceleration of OH in the high-field-seeking $^2\Pi_{3/2}, v = 0, J = 3/2\, e, M\Omega = 9/4$ state from 355 m/s to 316 m/s. (b) Longitudinal phase space evolution for the deceleration of OH in the low-field-seeking $^2\Pi_{3/2}, v = 0, J = 3/2\, f, M\Omega = -9/4$ state from 345 m/s to 239 m/s. The formation of the captured phase-stable packet of decelerated molecules is indicated by the dashed line.

4 mm × m/s. This results in a six-dimensional volume of 12 $mm^3 \times (m/s)^3$, which is considerably smaller than for focusing, mainly due to the decreased acceptance along the z-direction. The transverse phase space distribution plots for focusing for the hfs state and the lfs state are similar if x and y are interchanged. Furthermore, the transverse acceptance for the hfs state is larger along y, while for the lfs state it is larger along x. This is due to the fact that the forces which are focusing for the hfs state are defocusing for the lfs state and vice versa. The last two AG lenses are focusing in y-direction for the hfs state, but focusing in x-direction for the lfs state.

Figure 7.12 shows the longitudinal phase space evolution for the hfs $^2\Pi_{3/2}, v = 0, J = 3/2\, e, M\Omega = 9/4$ state for the deceleration from 355 m/s to 316 m/s and for the lfs $^2\Pi_{3/2}, v = 0, J = 3/2\, f, M\Omega = -9/4$ state from 345 m/s to 239 m/s, respectively. In the figures, the phase space distributions of all molecules are given at particular times, in which the synchronous molecule moves 60 mm or three AG lenses. The first distribution is plotted for $z = 0$ mm, which is 20 mm before the center of the first AG lens. The formation of the captured phase-stable packets shown in figures 7.10(f) and 7.11(f) and their deceleration to lower mean velocities are demonstrated. The other molecules which are not captured move on metastable trajectories. For the molecules in the hfs state also the formation of a the metastable packet which is lost from the synchronous packet and arrives in the last distribution 20 mm before with velocities between 315 m/s and 335 m/s the synchronous packet is visible (see also figure 7.3). For the molecules in the lfs state beside the synchronous packet also the metastable packet which is bunched at a velocity of about 433 m/s, similar to the metastable packet discussed in figure 7.6, is shown. These metastable packets result in non-synchronous peaks in the TOF profiles and are well reproduced in the measurements, as discussed in sections 7.3 and 7.4.

7.6 Coupling of transverse and longitudinal motion

In the following, the effects due to coupling of transverse and longitudinal motion for OH radicals in their lfs $^2\Pi_{3/2}, v = 0, J = 3/2\, f, M\Omega = -9/4$ state in the AG decelerator are studied using phase space distributions. In figure 7.13, the longitudinal phase space acceptance of the AG decelerator for OH radicals in their lfs state is shown for different focusing high voltage switching sequences. In contrast to the phase space acceptances discussed before, the acceptances are given in the center of the second electrode pair ($z = 40$ mm) and have been

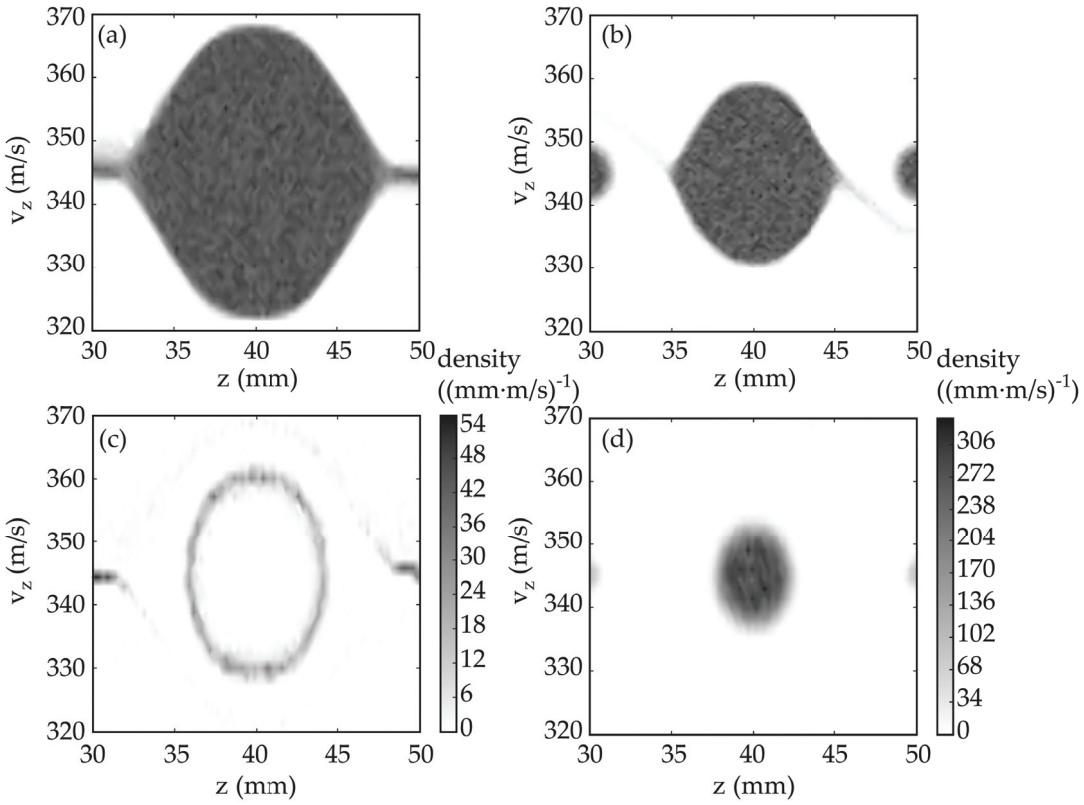

Figure 7.13: The longitudinal phase-space acceptances for focusing of OH radicals at a mean velocity of 345 m/s in their low-field seeking $^2\Pi_{3/2}, v = 0, J = 3/2\, f, M\Omega = -9/4$ state. Shown is the density of the projection of the phase space acceptance onto the (z, v_z) plane. Panels (a) and (b) are the acceptances for a one-dimensional model along the molecular beam axis. Panels (c) and (d) display the results of the full three-dimensional calculations. In (a) and (c) high-voltages are switched analogous to those in a normal Stark decelerator experiment, whereas in (b) and (d) the simulations are performed with the optimum focusing switching sequence as used in the experiments. See text for details.

calculated for a two meter long AG decelerator. For each plot, 300 million trajectories have been calculated.

The upper two images (figures 7.13(a) and (b)) show the phase space acceptance obtained from one-dimensional calculations where all molecules are confined on the molecular beam axis. Generally, in such a calculation all molecules eventually reach the detector. Therefore, in figures 7.13 (a) and (b) only the initial phase space positions of molecules that reach the detector within the synchronous packet are given in the shaded phase space areas. In figures 7.13 (c) and (d), the density of initial phase space positions of molecules of the synchronous packet with stable trajectories in full three-dimensional simulations projected onto the (z, v_z) plane are plotted. The density is given in units of accepted molecules (of 300 million calculated trajectories) per mm·m/s.

In order to compare the AG decelerator with a normal Stark decelerator, the high voltages for the AG decelerator are only switched on and off when the synchronous molecule is in between successive electrode pairs, using a bunching length of $b = 4$ mm. This results in the one- and three-dimensional phase space acceptances shown in figures 7.13 (a) and (c), respectively. In the three-dimensional calculation only a small ring of phase-stable positions is observed and for most phase space positions, i. e. , in the central part of the one-dimensional distribution, the trajectories are not stable. The observed halo and the central region of instability have been observed and analyzed before for the normal Stark decelerator and are attributed to parametric instabilities as a result of the coupling of longitudinal and transverse motion [186]. In the normal Stark decelerator, this problem can partly be avoided by applying overtone switching frequencies.

The AG decelerator used in this thesis allows to independently control the longitudinal bunching and the transverse focusing strength such that parametric amplification from the coupling of longitudinal and transverse motion can be minimized. The effect of applying an additional transverse focusing field applied around the center of the electrode pairs is shown in figures 7.13 (b) and (d), where the acceptances are calculated using the optimum focusing switching sequence ($f = 3$ mm and $b = 4$ mm) applied in the experiments described above. In the one-dimensional calculation, the packet is split up into two smaller packets due to the smaller lattice-cell lengths: the molecules encounter the force of the electric fields every 10 mm instead of every 20 mm, due to the doubled number of high voltage pulses (half of them for longitudinal bunching, the other half for transverse focusing). Since the molecules do not know this, they might use the fields for bunching instead of focusing and vice versa. These smaller packets are

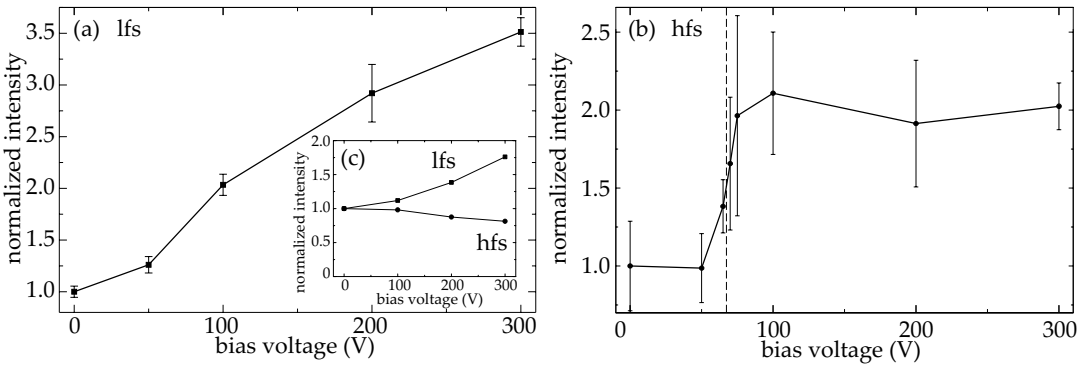

Figure 7.14: (a) Dependence of the integrated intensity for OH in the low-field-seeking (lfs) $X^2\Pi_{3/2}, v = 0, J = 3/2\, f, F = 2$ state and (b) the high-field-seeking (hfs) $X^2\Pi_{3/2}, v = 0, J = 3/2\, e, F = 2$ state for optimum focusing on the absolute value of the bias voltage. The bias voltage which corresponds to the electric field strength along the molecular beam axis where the level crossing of two hyperfine states occurs is indicated by the vertical dashed line. (c) Inset: simulated bias voltage dependence of the TOF profiles without switched high voltages applied.

not observed, due to the small initial molecular packet of $\Delta z = 2$ mm in the experiments. For the three-dimensional calculation, the projection of the phase space acceptance onto the (z, v_z) plane closely resembles the one-dimensional acceptance, and the central region of instability observed in figure 7.13(c) does not exist at all. Instead, the phase space acceptance is highest around the synchronous molecule, allowing to efficiently couple a molecular beam, which typically has a Gaussian-like phase space distributions, into the AG decelerator. From these findings it can be concluded that the AG decelerator allows to efficiently decouple transverse and longitudinal focusing properties. However, since for deceleration using large d values some transverse focusing already occurs during the first switching step for bunching and deceleration, the transverse and longitudinal motion may couple again. By choosing moderate d values and a longer AG decelerator, this can be circumvented.

7.7 Influence of the bias voltage

OH radicals can be lost from a certain quantum state due to Majorana transitions at zero electric field strength or due to non-adiabatic transitions at level crossings. These effects are reduced by applying a bias voltage of ±300 V to the electrodes instead of switching them between high voltage and ground. The dependence of the integrated intensity of the synchronous peak for OH in the lfs and hfs state on the bias voltage is presented in figures 7.14(a) and (b). For

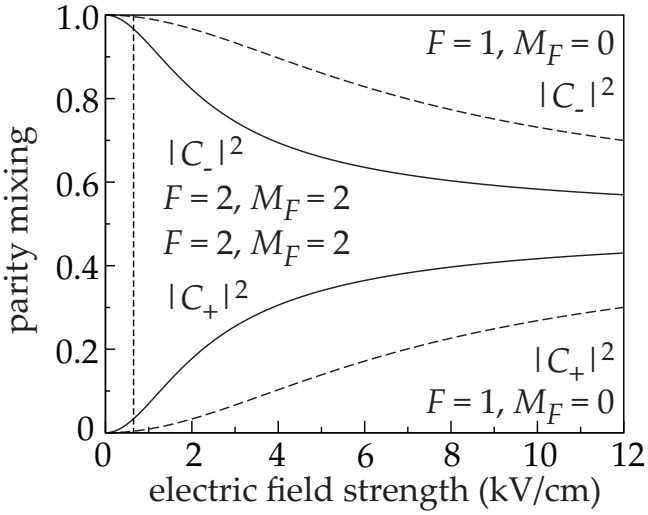

Figure 7.15: Squares of the mixing coefficients with states of positive and negative parity as a function of the electric field strength for the $F = 1$, $M_F = 0$ state (dashed line) and $F = 2$, $M_F = 2$ state (solid line). The bias voltage which corresponds to the electric field strength along the molecular beam axis, where the level crossing of two hyperfine states occurs, is indicated by the vertical dashed line.

comparison, the bias voltage dependencies of the integrated intensities without switched fields applied for hfs and lfs states are shown in the inset 7.14(c). For the experiments with OH in the lfs state, a continuous signal enhancement of up to a factor of 3.5 can be observed when tuning the bias voltage from 0 V to ±300 V. This increase is mainly due to focusing effects of the lfs molecules in the electric field and is also observed in the simulations of the free-flight TOF profile. Furthermore, Majorana transitions at zero field are suppressed. For the hfs states, a sudden rise in signal intensity can be observed for a voltage of about ±67 V, which corresponds to a maximum electric field strength on the molecular beam axis of 640 V/cm. The threshold is broadened due to the inhomogeneity of the electric fields along an electrode stage. At a field strength of 650 V/cm, a real crossing between the $X^2\Pi_{3/2}, v = 0, J = 3/2\,e$, $F = 2$, $M_F = 2$ and $X^2\Pi_{3/2}, v = 0, J = 3/2\,e, F = 1, M_F = 0$ hyperfine states occurs, as shown in figure 2.4(b) in chapter 2.3.

Both hyperfine states have negative parity (see chapter 2.3). The coupling of states with the same parity is dipole forbidden in the absence of an electric field. In an electric field, however, hyperfine states of different parities mix. The squares of the mixing coefficients are given by the projection of the hyperfine states involved in the crossing on the hyperfine states of the two Λ-doublet

components in the electric field. Only states with the same M_F contribute, and the mixing coefficients for the $X^2\Pi_{3/2}, v = 0, J = 3/2\,e,\ F = 2,\ M_F = 2$ state are

$$|C_-|^2 = \langle e, F = 2, M_F = 2|H_{\text{Stark}}|e, F = 2, M_F = 2\rangle^2 \quad (7.2)$$
$$|C_+|^2 = \langle e, F = 2, M_F = 2|H_{\text{Stark}}|f, F = 2, M_F = 2\rangle^2\,, \quad (7.3)$$

where $|C_-|^2$ is the square of the mixing coefficient for negative parity and $|C_+|^2$ for positive parity. The mixing coefficients for the $X^2\Pi_{3/2}, v = 0, J = 3/2\,e, F = 1, M_F = 0$ state are obtained accordingly. In figure 7.15, the squares of the mixing coefficients for both hyperfine levels of the crossing are shown. For positive parity, the mixing ratios at an electric field strength of 650 V/cm are 1 % and 4 % for the $X^2\Pi_{3/2}, v = 0, J = 3/2\,e, F = 1, M_F = 0$ and $X^2\Pi_{3/2}, v = 0, J = 3/2\,e, F = 2, M_F = 2$ state, respectively. This parity mixing for bias voltages below the threshold can be sufficient to allow transitions from the $F = 2, M_F = 2$ state to the $F = 1, M_F = 0$ state. In our experiment, the $F = 2,\ M_F = 2$ state is detected only, and, therefore, the detected intensity is reduced. For a bias voltage above the threshold, no loss from the $F = 2$ state to the $F = 1$ state can occur. Hence, this loss channel can be avoided by using an electric field bias larger than the crossing. A nearly two-fold increase of the signals is obtained for bias voltages above 100 V compared to bias voltages below 50 V.

7.8 Conclusions

The alternating-gradient focusing and deceleration of OH in both hfs and lfs states have been demonstrated using a single experimental setup. For the deceleration of the hfs state, the same switching sequences have been used as for benzonitrile (see chapter 6) and previous experiments [9, 13, 106]. About 21 % of the kinetic energy has been removed for the hfs state. In addition, the dependence of the focusing intensity on the bias voltage has been studied, where for the high-field-seeking quantum state, a threshold behavior has been found. This is most likely due to a real crossing of hyperfine states at the corresponding electric field strength.

More than 50 % of the kinetic energy has been removed in deceleration experiments for OH in its lfs state using an AG decelerator. This demonstrates the versatility of the AG decelerator, which can, in principle, be used for the deceleration of molecules in any polar quantum state. Due to the short length of the AG decelerator, a deceleration to a standstill was not possible. The results for

the deceleration of OH in the lfs state should be compared to the deceleration of OH using a normal Stark decelerator, where OH in the lfs state has been decelerated to standstill and finally trapped using an electrostatic trap [73]. However, it has been demonstrated that the AG decelerator allows to separately change the transverse and longitudinal focusing properties, avoiding the problems due to the coupling of the transverse and longitudinal motion [186, 189].

Chapter 8

Summary and outlook

In the framework of this thesis, a new alternating-gradient decelerator experiment for the focusing and deceleration of large molecules has been set up. Due to its large Stark energy-to-mass ratio, benzonitrile (C_7H_5N) is a prime candidate for alternating-gradient focusing and deceleration, and is prototypical for large asymmetric top molecules that exhibit rich rotational structure and a high density of states. Using the new alternating-gradient decelerator, the focusing properties for benzonitrile have been studied in three different low-lying rotational states, namely the absolute ground state $J_{K_aK_c} = 0_{00}$ and the rotationally excited states 1_{01} and 4_{04}. Benzonitrile molecules in the ground state have been decelerated from 320 m/s to 275 m/s and similar velocity changes have been obtained for the rotationally excited states. Due to the complicated Stark manifold with many real and avoided crossings, it was not *a priori* clear whether excited rotational states of benzonitrile could be decelerated. However, this has been successfully demonstrated in this thesis. These experiments show that such large polyatomic molecules are amenable to the powerful method of deceleration, using time-varying inhomogeneous electric fields. For the planning and the theoretical description of the alternating-gradient focusing and deceleration measurements, a precise knowledge of the dipole moment is essential. As published values for the dipole moment of benzonitrile [159, 168] did not give a consistent value, the dipole moment was determined to $\mu_a = 4.5152(68)$ D, using Fourier-transform microwave spectroscopy.

In another set of experiments, OH radicals in both low-field-seeking and high-field-seeking quantum states have been decelerated using the same alternating-gradient decelerator setup. For the deceleration of low-field-seeking OH radicals, a new high voltage switching scheme has been used in order to ensure phase stability. In addition, the decoupling of the longitudinal and transverse motion in an alternating-gradient decelerator has been studied. OH in the high-field-

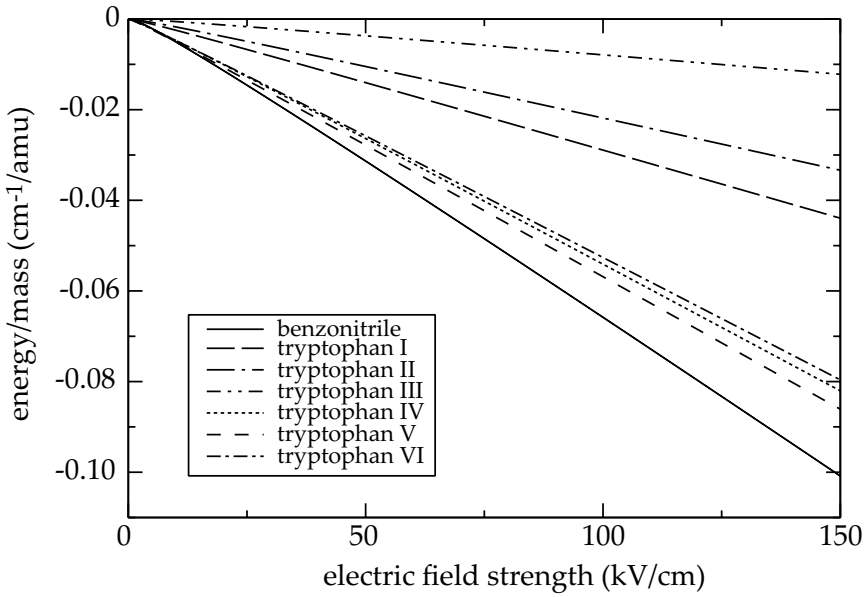

Figure 8.1: Energy-to-mass ratio of the ground state of benzonitrile (solid line) and the ground state of the six different conformers of tryptophan (dashed lines) as a function of the electric field strength.

seeking $X^2\Pi_{3/2}, v = 0, J = 3/2\, e$ state has been decelerated from 355 m/s to 316 m/s which corresponds to a reduction of kinetic energy of 21 %. OH in the low-field-seeking $X^2\Pi_{3/2}, v = 0, J = 3/2\, f$ state has been decelerated from 345 m/s to 276 m/s, removing more than 50 % of the kinetic energy, and from 305 m/s to 200 m/s. These experiments demonstrate the versatility of the AG decelerator, which can, in principle, be used for the deceleration of molecules in any polar quantum state. In addition, the dependence of the focusing intensity on the bias voltage has been studied, where for the high-field-seeking quantum state a threshold behavior has been observed. This is most likely due to a real crossing of hyperfine states at the corresponding electric field strength of the threshold.

The long-term goal of the project initiated in the framework of this thesis is the deceleration of large molecules and biomolecules to velocities low enough for trapping in AC electric traps. In order to trap the molecules, they have to be decelerated to almost a standstill. Therefore, the alternating-gradient decelerator is currently extended using a two-electrode pattern from 27 stages to 54 stages, and later 81 stages (see chapters 4.8 and 6.7). With a 81 stages long device, the deceleration of benzonitrile to velocities of 150 m/s should be feasible, which corresponds to reduction of the kinetic energy by about 80 %. For

the deceleration to even lower velocities, hyperbolically shaped electrodes or an asymmetric four-electrode configuration (see chapter 3.3) will be used. Furthermore, it will also be necessary to reduce the length and/or the voltage for the last electrode stages to avoid over-focusing of the molecules. After deceleration to about 20 m/s in an extended alternating-gradient decelerator setup, three-dimensional confinement in AC electric traps, in which the same principles of dynamic focusing as in the alternating-gradient decelerator are employed, will be possible. The trapping of molecules in their high-field-seeking states, which were decelerated in a normal Stark decelerator in their low-field-seeking state and were pumped to the high-field-seeking state using a microwave transition, has already been demonstrated for ND_3 [78, 108, 109]. The AC electric trapping should also be feasible for benzonitrile, once decelerated to sufficiently low velocities.

Interesting other molecular candidates for alternating-gradient focusing and deceleration have been discussed in chapter 2.4. One possible future candidate is the amino acid tryptophan. In figure 8.1, the energy-to-mass ratio for the ground state of benzonitrile and the ground state of the six different conformers of tryptophan as a function of the electric field strength are shown. The more polar conformers IV, V, and VI have similar energy-to-mass ratios as benzonitrile and could, therefore, be decelerated with comparable acceptances. Because of their different Stark energies, the more polar conformers could be separated from the less polar ones. The separation of the *cis* and *trans* conformers of 3-aminophenol in an electric quadrupole selector using AG focusing has recently been demonstrated [23]. Similarly, using an alternating-gradient decelerator, different conformers of decelerated molecules could be separated from each other. A trapped sample of conformer-selected biomolecules would enable precise studies of the intrinsic properties of these species, for example, dynamical processes on timescales ranging from femto-seconds to fractions of a second, i. e. , interconversion between conformational structures.

Bibliography

[1] Special Issue "Ultracold Polar Molecules: Formation and Collisions", Eur. Phys. J. D **31**, 149 (2004).

[2] H. L. Bethlem and G. Meijer, Int. Rev. Phys. Chem. **22**, 73 (2003).

[3] R. V. Krems, Int. Rev. Phys. Chem. **24**, 99 (2005).

[4] L. R. Hunter, Science **252**, 73 (1991).

[5] D. DeMille, F. Bay, S. Bickman, D. Kawall, D. K. Jr., S. E. Maxwell, and L. R. Hunter, Phys. Rev. A **61**, 052507 (2000).

[6] D. Kawall, F. Bay, S. Bickman, Y. Jiang, and D. DeMille, Phys. Rev. Lett. **92**, 133007 (2004).

[7] J. J. Hudson, B. E. Sauer, M. R. Tarbutt, and E. A. Hinds, Phys. Rev. Lett. **89**, 023003 (2002).

[8] B. C. Regan, E. D. Commins, C. J. Schmidt, and D. DeMille, Phys. Rev. Lett. **88**, 071805 (2002).

[9] M. R. Tarbutt, H. L. Bethlem, J. J. Hudson, V. L. Ryabov, V. A. Ryzhov, B. E. Sauer, G. Meijer, and E. A. Hinds, Phys. Rev. Lett. **92**, 173002 (2004).

[10] E. R. Hudson, H. J. Lewandowski, B. C. Sawyer, and J. Ye, Phys. Rev. Lett. **96**, 143004 (2006).

[11] J. Mikosch, S. Trippel, C. Eichhorn, R. Otto, U. Lourderaj, J. X. Zhang, W. L. Hase, M. Weidemüller, and R. Wester, Science **319**, 183 (2008).

[12] D. Auerbach, E. E. A. Bromberg, and L. Wharton, J. Chem. Phys. **45**, 2160 (1966).

[13] H. L. Bethlem, A. J. A. van Roij, R. T. Jongma, and G. Meijer, Phys. Rev. Lett. **88**, 133003 (2002).

[14] Special issue "Molecular physics of building blocks of life under isolated or defined conditions", Eur. Phys. J. D **20**, 309 (2002).

[15] Special issue "Bio-active molecules in the gas phase", Phys. Chem. Chem. Phys. **6**, 2543 (2004).

[16] M. S. de Vries and P. Hobza, Annu. Rev. Phys. Chem. **58**, 585 (2007).

[17] J. van Veldhoven, J. Küpper, H. L. Bethlem, B. Sartakov, A. J. van Roij, and G. Meijer, Eur. Phys. J. D **31**, 337 (2004).

[18] R. D. Suenram and F. J. Lovas, J. Am. Chem. Soc. **102**, 7180 (1980).

[19] T. R. Rizzo, Y. D. Park, L. Peteanu, and D. H. Levy, J. Chem. Phys. **83**, 4819 (1985).

[20] T. R. Rizzo, Y. D. Park, L. A. Peteanu, and D. H. Levy, J. Chem. Phys. **84**, 2534 (1986).

[21] I. Compagnon, F. C. Hagemeister, R. Antoine, D. Rayane, M. Broyer, P. Dugourd, R. R. Hudgins, and M. F. Jarrold, J. Am. Chem. Soc. **123**, 8440 (2001).

[22] L. C. Snoek, R. T. Kroemer, M. R. Hockridge, and J. P. Simons, Phys. Chem. Chem. Phys. **3**, 1819 (2001).

[23] F. Filsinger, U. Erlekam, G. von Helden, J. Küpper, and G. Meijer, Phys. Rev. Lett. **100** (2008).

[24] K. Hedberg, L. Hedberg, D. S. Bethune, C. A. Brown, H. C. Dorn, R. D. Johnson, and M. de Vries, Science **254**, 410 (1991).

[25] H. N. Chapman, A. Barty, M. J. Bogan, S. Boutet, S. Frank, S. P. Hau-Riege, S. Marchesini, B. W. Woods, S. Bajt, W. H. Benner, L. W. A., E. Plönjes, M. Kuhlmann, R. Treusch, S. Düsterer, T. Tschentscher, J. R. Schneider, E. Spiller, T. Möller, C. Bostedt, M. Hoener, D. A. Shapiro, K. O. Hodgson, D. van der Spoel, F. Burmeister, M. Bergh, C. Caleman, G. Huldt, M. M. Seibert, F. R. N. C. Maia, R. W. Lee, A. Szönke, N. Timneanu, and J. Hajdu, Nature Phys. **2**, 839 (2006).

[26] S. Gerlich, L. Hackermüller, K. Hornberger, A. Stibor, H. Ulbricht, M. Gring, F. Goldfarb, T. Savas, M. Müri, M. Mayor, and M. Arndt, Nature Phys. **3**, 711 (2007).

[27] D. W. Rein, J. Mol. Evol. **4**, 15 (1974).

[28] V. S. Letokhov, Phys. Lett. A **53**, 275 (1975).

[29] C. Daussy, T. Marrel, A. Amy-Klein, C. T. Nguyen, C. J. Bordé, and C. Chardonnet, Phys. Rev. Lett. **83**, 1554 (1999).

[30] S. Chu, Rev. Mod. Phys. **70**, 685 (1998).

[31] C. N. Cohen-Tannoudji, Rev. Mod. Phys. **70**, 707 (1998).

[32] W. D. Phillips, Rev. Mod. Phys. **70**, 721 (1998).

[33] J. T. Bahns, W. C. Stwalley, and P. L. Gould, J. Chem. Phys. **104**, 9689 (1996).

[34] M. H. Anderson, J. R. Ensher, M. R. Matthews, C. E. Wieman, and E. A. Cornell, Science **269**, 198 (1995).

[35] K. B. Davis, M. O. Mewes, M. R. Andrews, N. J. van Druten, D. S. Durfee, D. M. Kurn, and W. Ketterle, Phys. Rev. Lett. **75**, 3969 (1995).

[36] M. Greiner, C. A. Regal, and D. S. Jin, Nature **426**, 537 (2003).

[37] S. Jochim, M. Bartenstein, A. Altmeyer, G. Hendl, C. Chin, J. H. Denschlag, and R. Grimm, Phys. Rev. Lett. **91**, 240402 (2003).

[38] M. W. Zwierlein, C. A. Stan, C. H. Schunck, S. M. F. Raupach, S. Gupta, Z. Hadzibabic, and W. Ketterle, Phys. Rev. Lett. **91**, 250401 (2003).

[39] J. H. Denschlag, H.-C. Nägerl, and R. Grimm, Physik Journal **3**, 33 (2003).

[40] H. R. Thorsheim, J. Weiner, and P. S. Julienne, Phys. Rev. Lett. **58**, 2420 (1987).

[41] A. Fioretti, D. Comparat, A. Crubellier, O. Dulieu, F. Masnou-Seeuws, and P. Pillet, Phys. Rev. Lett. **80**, 4402 (1998).

[42] C. Gabbanini, A. Fioretti, A. Lucchesini, S. Gozzini, and M. Mazzoni, Phys. Rev. Lett. **84**, 2814 (2000).

[43] A. J. Kerman, J. M. Sage, S. Sainis, T. Bergeman, and D. DeMille, Phys. Rev. Lett. **92**, 153001 (2004).

[44] C. Haimberger, J. Kleinert, M. Bhattacharya, and N. P. Bigelow, Phys. Rev. A **70**, 021402 (2004).

[45] M. W. Mancini, G. D. Telles, A. R. L. Caires, V. S. Bagnato, and L. G. Marcassa, Phys. Rev. Lett. **92**, 133203 (2004).

[46] S. D. Kraft, P. Staanum, J. Lange, L. Vogel, R. Wester, and M. Weidemüller, J. Phys. B **39**, S993 (2006).

[47] J. M. Sage, S. Sainis, T. Bergeman, and D. DeMille, Phys. Rev. Lett. **94**, 203001 (2005).

[48] C. P. Koch, J. P. Palao, R. Kosloff, and F. Masnou-Seeuws, Phys. Rev. A **70**, 013402 (2004).

[49] F. Weise, S. Birkner, A. Merli, S. M. Weber, F. Sauer, L. Wöste, A. Lindinger, W. Salzmann, T. G. Mullins, J. Eng, M. Albert, R. Wester, and M. Weidemüller, Phys. Rev. A **76**, 063404 (2007).

[50] J. Kim, B. Friedrich, D. P. Katz, D. Patterson, J. D. Weinstein, R. deCarvalho, and J. M. Doyle, Phys. Rev. Lett. **78**, 3665 (1997).

[51] J. D. Weinstein, R. deCarvalho, T. Guillet, B. Friedrich, and J. M. Doyle, Nature **395**, 148 (1998).

[52] W. C. Campbell, E. Tsikata, H. I. Lu, L. D. van Buuren, and J. M. Doyle, Phys. Rev. Lett. **98**, 213001 (2007).

[53] M. Stoll, J. Bakker, T. C. Steimle, G. Meijer, and A. Peters, In preparation (2008).

[54] S. A. Rangwala, T. Junglen, T. Rieger, P. W. H. Pinkse, and G. Rempe, Phys. Rev. A **67**, 043406 (2003).

[55] T. Rieger, T. Junglen, S. A. Rangwala, G. Rempe, and P. W. H. Pinkse, Phys. Rev. A **73**, 061402 (2006).

[56] T. Junglen, T. Rieger, S. A. Rangwala, P. W. H. Pinkse, and G. Rempe, Phys. Rev. Lett. **92**, 223001 (2004).

[57] S. Deachapunya, P. J. Fagan, A. G. Major, E. Reiger, H. Ritsch, A. Stefanov, H. Ulbricht, and M. Arndt, Eur. Phys. J. D **46**, 307 (2008).

[58] G. Scoles, ed., *Atomic and molecular beam methods*, vol. 1 & 2 (Oxford University Press, New York, NY, USA, 1988 & 1992).

[59] M. S. Elioff, J. J. Valentini, and D. W. Chandler, Science **302**, 1940 (2003).

[60] M. Gupta and D. Herschbach, J. Phys. Chem. A **103**, 10670 (1999).

[61] M. Gupta and D. Herschbach, J. Phys. Chem. A **105**, 1626 (2001).

[62] W. Gerlach and O. Stern, Zeitschrift für Physik **9**, 349 (1922).

[63] E. Wrede, Zeitschrift für Physik A **44**, 261 (1927).

[64] H. Friedburg and W. Paul, Die Naturwissenschaften **38**, 159 (1951).

[65] H. G. Bennewitz and W. Paul, Zeitschrift für Physik **139**, 489 (1954).

[66] H. G. Bennewitz, W. Paul, and C. Schlier, Zeitschrift für Physik **141**, 6 (1955).

[67] J. P. Gordon, H. J. Zeiger, and C. H. Townes, Phys. Rev. **95**, 282 (1954).

[68] J. P. Gordon, H. J. Zeiger, and C. H. Townes, Phys. Rev. **99**, 1264 (1955).

[69] H. L. Bethlem, G. Berden, and G. Meijer, Phys. Rev. Lett. **83**, 1558 (1999).

[70] H. L. Bethlem, G. Berden, A. J. A. van Roij, F. M. H. Crompvoets, and G. Meijer, Phys. Rev. Lett. **84**, 5744 (2000).

[71] H. L. Bethlem, F. M. H. Crompvoets, R. T. Jongma, S. Y. T. van de Meerakker, and G. Meijer, Phys. Rev. A **65**, 053416 (2002).

[72] H. L. Bethlem, G. Berden, F. M. H. Crompvoets, R. T. Jongma, A. J. A. van Roij, and G. Meijer, Nature **406**, 491 (2000).

[73] S. Y. T. van de Meerakker, P. H. M. Smeets, N. Vanhaecke, R. T. Jongma, and G. Meijer, Phys. Rev. Lett. **94**, 023004 (2005).

[74] J. R. Bochinski, E. R. Hudson, H. J. Lewandowski, G. Meijer, and J. Ye, Phys. Rev. Lett. **91**, 243001 (2003).

[75] S. Y. van de Meerakker, I. Labazan, S. Hoekstra, J. Küpper, and G. Meijer, J. Phys. B **39**, S1077 (2006).

[76] E. R. Hudson, C. Ticknor, B. C. Sawyer, C. A. Taatjes, H. J. Lewandowski, J. R. Bochinski, J. L. Bohn, and J. Ye, Phys. Rev. A **73**, 063404 (2006).

[77] S. Jung, E. Tiemann, and C. Lisdat, Phys. Rev. A **74**, 040701 (2006).

[78] J. van Veldhoven, H. L. Bethlem, and G. Meijer, Phys. Rev. Lett. **94**, 083001 (2005).

[79] B. C. Sawyer, B. L. Lev, E. R. Hudson, B. K. Stuhl, M. Lara, J. L. Bohn, and J. Ye, Phys. Rev. Lett. **98**, 253002 (2007).

[80] F. M. H. Crompvoets, H. L. Bethlem, R. T. Jongma, and G. Meijer, Nature **411**, 174 (2001).

[81] F. M. H. Crompvoets, H. L. Bethlem, J. Küpper, A. J. A. van Roij, and G. Meijer, Phys. Rev. A **69**, 063406 (2004).

[82] C. E. Heiner, D. Carty, G. Meijer, and H. L. Bethlem, Nature Phys. **3**, 115 (2007).

[83] S. A. Meek, H. L. Bethlem, H. Conrad, and M. G., Phys. Rev. Lett. **100**, 153003 (2008).

[84] N. Vanhaecke, D. Comparat, and P. Piller, J. Phys. B **38**, S409 (2005).

[85] S. Hogan and F. Merkt, Phys. Rev. Lett. **100**, 043001 (2008).

[86] N. Vanhaecke, U. Meier, M. Andrist, B. H. Meier, and F. Merkt, Phys. Rev. A **75**, 031402(R) (2007).

[87] S. Hogan, D. Sprecher, M. Andrist, N. Vanhaecke, and F. Merkt, Phys. Rev. A **76**, 023412 (2007).

[88] E. Narevicius, A. Libson, C. G. Parthey, I. Chavez, J. Narevicius, U. Even, and M. G. Raizen, Phys. Rev. Lett. **100**, 093003 (2008).

[89] E. Narevicius, A. Libson, C. G. Parthey, I. Chavez, J. Narevicius, U. Even, and M. G. Raizen, arXiv p. 0804.0219 (2008).

[90] G. J. Dong, W. P. Lu, and P. F. Barker, Phys. Rev. A **69**, 013409 (2004).

[91] R. Fulton, A. I. Bishop, M. N. Shneider, and P. F. Barker, Nature Phys. **2**, 465 (2006).

[92] R. Fulton, A. I. Bishop, M. N. Shneider, and P. F. Barker, J. Phys. B **39**, S1097 (2006).

[93] W. H. Wing, Prog. Quant. Electr. **8**, 181 (1984).

[94] W. Ketterle and D. E. Pritchard, Appl. Phys. B **54**, 403 (1992).

[95] E. D. Courant and H. S. Snyder, Ann. Phys. **3**, 1 (1958).

[96] S. Y. Lee, *Accelerator physics* (World Scientific, Singapore, 2004), 2nd ed.

[97] D. Kakati and D. C. Lainé, Phys. Lett. A **24**, 676 (1967).

[98] D. Kakati and D. C. Lainé, Phys. Lett. A **28**, 786 (1969).

[99] D. Kakati and D. C. Lainé, J. Phys. E **4**, 269 (1971).

[100] F. Günther and K. Schügerl, Z. Phys. Chem. **NF80**, 155 (1972).

[101] A. Lübbert, F. Günther, and K. Schügerl, Chem. Phys. Lett. **35**, 210 (1975).

[102] A. Lübbert, G. Rotzoll, and F. Günther, J. Chem. Phys. **69**, 5174 (1978).

[103] H.-R. Noh, K. Shimizu, and F. Shimizu, Phys. Rev. A **61**, 041601(R) (2000).

[104] J. G. Kalnins, J. M. Amini, and H. Gould, Phys. Rev. A **72**, 043406 (2005).

[105] E. E. A. Bromberg, Ph.D. thesis, University of Chicago (1972).

[106] H. L. Bethlem, M. R. Tarbutt, J. Küpper, D. Carty, K. Wohlfart, E. A. Hinds, and G. Meijer, J. Phys. B **39**, R263 (2006).

[107] W. Paul, Rev. Mod. Phys. **62**, 531 (1990).

[108] H. L. Bethlem, J. van Veldhoven, M. Schnell, and G. Meijer, Phys. Rev. A **74**, 063403 (2006).

[109] M. Schnell, P. Lützow, J. van Veldhoven, H. L. Bethlem, J. Küpper, B. Friedrich, M. Schleier-Smith, H. Haak, and G. Meijer, J. Phys. Chem. A **111**, 7411 (2007).

[110] J. Cernicharo, A. M. Heras, A. G. G. M. Tielens, J. R. Pardo, F. Herpin, M. Guélin, and L. B. F. M. Waters, Astrophys. J. **546**, L123 (2001).

[111] P. M. Woods, T. J. Millar, A. A. Zijlstra, and E. Herbst, Astrophys. J. **574**, L167 (2002).

[112] W. Demtröder, *Molekülphysik* (Oldenbourg Wissenschaftsverlag, München, 2003).

[113] W. Gordy and R. L. Cook, *Microwave Molecular Spectra* (John Wiley & Sons, New York, NY, USA, 1984), 3rd ed.

[114] C. H. Townes and A. L. Schawlow, *Microwave Spectroscopy* (Dover Publications, New York, 1975).

[115] K. Wohlfart, M. Schnell, J.-U. Grabow, and J. Küpper, J. Mol. Spec. **247**, 119 (2008).

[116] R. N. Zare, *Angular Momentum* (John Wiley & Sons, New York, NY, USA, 1988).

[117] S. C. Wang, Phys. Rev. **34**, 243 (1929).

[118] P. R. Bunker and P. Jensen, *Molecular Symmetry and Spectroscopy* (NRC Research Press, Ottawa, Ontario, Canada, 1998), 2nd ed.

[119] M. Abd El Rahim, R. Antoine, M. Broyer, D. Rayane, and P. Dugourd, J. Phys. Chem. A **109**, 8507 (2005).

[120] J. Küpper and F. Filsinger, *`libcoldmol`: A particle trajectory calculation framework* (2003–2008), URL: `http://libcoldmol.cold-molecules.info`.

[121] J. K. G. Watson, in *Vibrational Spectra and Structure*, edited by J. R. Durig (Marcel Dekker, 1977), vol. 6, chap. 1.

[122] G. Herzberg, *The Spectra and Structures of Simple Free Radicals* (Dover Publications, New York, NY, USA, 1971).

[123] T. D. Hain, M. A. Weibel, K. M. Backstrand, and T. J. Curtiss, J. Phys. Chem. A **101**, 7674 (1997).

[124] G. H. Dieke and J. Crosswhite, J. Quant. Spectrosc. Radiat. Transf. **2**, 97 (1962).

[125] K. F. Freed, J. Chem. Phys. **45**, 4214 (1966).

[126] P. Andresen and E. Rothe, J. Chem. Phys. **82**, 3634 (1985).

[127] W. L. Meerts and A. Dymanus, Chem. Phys. Lett. **23**, 45 (1973).

[128] S. Y. T. van de Meerakker, Ph. D. thesis, Radboud Universiteit, Nijmegen, The Netherlands (2005).

[129] H. Z. Li, K. J. Franks, R. J. Hanson, and W. Kong, J. Phys. Chem. A **102**, 8084 (1998).

[130] R. W. Fields, S. G. Tilford, and R. A. Howard, J. Mol. Spec. **44**, 347 (1972).

[131] R. T. Jongma, G. von Helden, G. Berden, and G. Meijer, Chem. Phys. Lett. **270**, 304 (1997).

[132] A. L. Kaledin, J. C. Bloch, M. C. McCarthy, and R. W. Field, J. Mol. Spec. **197**, 289 (1999).

[133] W. J. Childs, L. S. Goodman, U. Nielsen, and V. Pfeufer, J. Phys. Chem. **80**, 2283 (1984).

[134] B. E. Sauer, J. Wang, and E. A. Hinds, J. Chem. Phys. **105**, 7412 (1996).

[135] G. Herzberg, *Infrared and Raman Spectra of Polyatomic Molecules*, vol. 2 (Van Nostrand, Princeton, NJ, 1945).

[136] D. A. Baugh, D. Y. Kim, V. A. Cho, L. Pipes, J. Petteway, and C. D. Fuglesang, Chem. Phys. Lett. **219**, 207 (1994).

[137] K. Wohlfart, F. Filsinger, F. Grätz, H. Haak, J. Küpper, and G. Meijer, In preparation (2008).

[138] S. A. Clough, Y. Beers, G. P. Klein, and L. S. Rothman, J. Chem. Phys. **59**, 2254 (1973).

[139] W. S. Benedict, N. Gailar, and E. K. Plyler, J. Chem. Phys. **21**, 1301 (1953).

[140] T. E. Sullivan and L. Frenkel, J. Mol. Spec. **39**, 185 (1971).

[141] D. R. Lide, ed., *CRC Handbook of Chemistry and Physics*, vol. 71 (CRC Press, Boca Raton, 1990).

[142] R. A. Cresswell and G. Winnewisser, J. Mol. Spec. **65**, 420 (1977).

[143] K. Wohlfart, F. Grätz, F. Filsinger, H. Haak, G. Meijer, and J. Küpper, Phys. Rev. A **77**, 031404(R) (2008).

[144] M. Y. Choi and R. E. Miller, J. Am. Chem. Soc. **128**, 7320 (2006).

[145] M. Y. Choi, *private communication* (2008).

[146] H. L. Bethlem, Ph.D. thesis, Katholieke Universiteit Nijmegen, The Netherlands (2002).

[147] S. Earnshaw, Trans. Camb. Phil. Soc. **7**, 97 (1842).

[148] J. G. Kalnins, G. Lambertson, and H. Gould, Rev. Sci. Instrum. **73**, 2557 (2002).

[149] Comsol, *Multiphysics 3.2* (2006), `http://www.comsol.com/products`.

[150] M. R. Tarbutt and E. A. Hinds, arXiv p. 0804.2077 (2008).

[151] M. R. Tarbutt, J. J. Hudson, B. E. Sauer, and E. A. Hinds, *Preparation and manipulation of molecules for fundamental physics tests* (2008), book in preparation, preprint at `http://arxiv.org/abs/0803.0967`.

[152] J. Küpper, H. Haak, K. Wohlfart, and G. Meijer, Rev. Sci. Instrum. **77**, 016106 (2006).

[153] M. T. Berry, M. R. Brustein, and M. I. Lester, Chem. Phys. Lett. **153**, 17 (1988).

[154] R. V. Latham, *High voltage vaccum insulation: basic concepts and technological practice* (Academic Press, London, 1995).

[155] J. Küpper, H. Junkes, and U. Hoppe, *KouDA: A general purpose data acquistion system* (2003–2007), `http://kouda.cold-molecules.info`.

[156] R. W. P. Drever, J. L. Hall, F. V. Kowalski, J. Hough, G. M. Ford, A. J. Munley, and H. Ward, Appl. Phys. B **31**, 97 (1983).

[157] G. Bardizza, Master's thesis, Università degli Studi di Milano, Milano, Italy (2005).

[158] S. Gerstenkorn and P. Luc, *Atlas du Spectre d'Absorption de la Molecule d'Iode entre* (CNRS, Paris, 1985).

[159] D. R. Borst, T. M. Korter, and D. W. Pratt, Chem. Phys. Lett. **350**, 485 (2001).

[160] B. G. Lindsay, K. A. Smith, and F. B. Dunning, Rev. Sci. Instrum. **62**, 1656 (1991).

[161] S. M. Jaffe, M. Rochon, and W. M. Yen, Rev. Sci. Instrum. **64**, 2475 (1993).

[162] D. H. Jaffer and I. W. M. Smith, Faraday Disc. Chem. Soc **76**, 212 (1979).

[163] J. C. D. Brand, J. Mol. Spec. **36**, 328 (1970).

[164] R. M. Helm, H. P. Vogel, and H. J. Neusser, Chem. Phys. Lett. **270**, 285 (1997).

[165] T. Kobayashi and O. Kajimoto, J. Chem. Phys. **86**, 1118 (1987).

[166] K. Sakota, K. Nishi, K. Ohashi, and H. Sekiya, Chem. Phys. Lett. **322**, 407 (2000).

[167] U. Even, J. Jortner, D. Noy, N. Lavie, and N. Cossart-Magos, J. Chem. Phys. **112**, 8068 (2000).

[168] D. R. Lide, J. Chem. Phys. **22**, 1577 (1954).

[169] T. J. Balle and W. H. Flygare, Rev. Sci. Instrum. **52**, 33 (1981).

[170] J.-U. Grabow, W. Stahl, and H. Dreizler, Rev. Sci. Instrum. **67**, 4072 (1996).

[171] M. Schnell, D. Banser, and J.-U. Grabow, Rev. Sci. Instrum. **75**, 2111 (2004).

[172] J.-U. Grabow and W. Stahl, Z. Naturforsch. A **45**, 1043 (1990).

[173] C. Chuang, C. J. Hawley, T. Emilsson, and H. S. Gutowsky, Rev. Sci. Instrum. **61**, 1629 (1990).

[174] U. Andresen, H. Dreizler, J.-U. Grabow, and W. Stahl, Rev. Sci. Instrum. **61**, 3694 (1990).

[175] J.-U. Grabow, Habilitationsschrift, Gottfried-Wilhelm-Leibniz-Universität Hannover, Germany (2004).

[176] E. J. Campbell, W. G. Read, and J. A. Shea, Chem. Phys. Lett. **94**, 69 (1983).

[177] J. M. L. J. Reinartz and A. Dymanus, Chem. Phys. Lett. **24**, 346 (1974).

[178] F. Filsinger, K. Wohlfart, M. Schnell, J.-U. Grabow, and J. Küpper, Phys. Chem. Chem. Phys. **10**, 666 (2008).

[179] E. Fliege, G. Bestmann, R. Schwarz, and H. Dreizler, Z. Naturforsch. A **36**, 1124 (1981).

[180] K. Vormann, U. Andresen, N. Heineking, and H. Dreizler, Z. Naturforsch. A **43**, 283 (1988).

[181] Z. Kisiel, J. Kosarzewski, B. A. Pietrewicz, and L. Pszczółkowski, Chem. Phys. Lett. **325**, 523 (2000).

[182] Z. Kisiel, B. A. Pietrewicz, P. W. Fowler, A. C. Legon, and E. Steiner, J. Phys. Chem. A **104**, 6970 (2000).

[183] G. Wlodarczak, J. Burie, J. Demaison, K. Vormann, and A. G. Császár, J. Mol. Spec. **134**, 297 (1989).

[184] E. Vliegen, H. J. Wörner, T. P. Softley, and F. Merkt, Phys. Rev. Lett. **92**, 033005 (2004).

[185] C. M. Western, *Pgopher, a program for simulating rotational structure*, University of Bristol, Bristol, UK, URL: `http://pgopher.chm.bris.ac.uk`.

[186] S. Y. T. van de Meerakker, N. Vanhaecke, H. L. Bethlem, and G. Meijer, Phys. Rev. A **73**, 023401 (2006).

[187] P. Lützow, S. Schnell, and G. Meijer, submitted to Phys. Rev. A (2008).

[188] R. Alheit, S. Kleineidam, F. Vedel, M. Vedel, and G. Werth, Int. J. Mass Spectrom. **154**, 155 (1996).

[189] S. Y. T. van de Meerakker, N. Vanhaecke, H. L. Bethlem, and G. Meijer, Phys. Rev. A **71**, 053409 (2005).

[190] B. C. Sawyer, B. K. Stuhl, B. L. Lev, E. R. Hudson, and J. Ye, arXiv p. 0705.3442 (2007).

[191] W. L. Meerts, Chem. Phys. Lett. **46**, 24 (1977).

[192] J. J. T. Meulen, W. A. Majewski, W. L. Meerts, and A. Dymanus, Chem. Phys. Lett. **94**, 25 (1983).

[193] D. R. Yarkoni, J. Chem. Phys. **97**, 1838 (1992).

List of publications

- *Alternating gradient focusing and deceleration of polar molecules*
  Hendrick L. Bethlem, Michael R. Tarbutt, Jochen Küpper, David Carty, Kirstin Wohlfart, Ed A. Hinds, and Gerard Meijer
  J. Phys. B **39**, R263 (2006).

- *Compact in-place gate valve for molecular-beam experiments*
  Jochen Küpper, Henrik Haak, Kirstin Wohlfart, and Gerard Meijer
  Rev. Sci. Instrum. **77**, 016106 (2006).

- *Precise dipole moment and quadrupole coupling constants of benzonitrile*
  Kirstin Wohlfart, Melanie Schnell, Jens-Uwe Grabow, and Jochen Küpper
  J. Mol. Spec. **247**, 119 (2008).

- *Precise dipole moments and quadrupole coupling constants of the cis and trans conformers of 3-aminophenol: Determination of the absolute conformation*
  Frank Filsinger, Kirstin Wohlfart, Melanie Schnell, Jens-Uwe Grabow, and Jochen Küpper
  Phys. Chem. Chem. Phys. **10**, 666 (2008).

- *Alternating-gradient focusing and deceleration of large molecules*
  Kirstin Wohlfart, Fabian Grätz, Frank Filsinger, Henrik Haak, Gerard Meijer, and Jochen Küpper
  Phys. Rev. A **77**, 031404(R) (2008).

- *Decoupling of longitudinal and transverse motion in the Stark decelerator using alternating-gradient focusing*
  Kirstin Wohlfart, Frank Filsinger, Fabian Grätz, Henrik Haak, Jochen Küpper, and Gerard Meijer
  In preparation (2008).

Selbständigkeitserklärung

Hiermit erkläre ich, Kirstin Wohlfart, die vorliegende Arbeit selbstständig und nur unter Verwendung der angegebenen Hilfsmittel und Literatur angefertigt zu haben.

Berlin, den 05. Mai 2008

Kirstin Wohlfart

Danksagung

Ohne die Mitarbeit von vielen Personen, denen ich herzlich danken möchte, wäre diese Doktorarbeit nicht möglich gewesen. Zuerst einmal möchte ich Gerard Meijer dafür danken, dass er mich als eine seiner ersten Berliner Doktorandinnen kurz nach dem Umzug seiner Arbeitsgruppe von Holland aufgenommen und mir die Möglichkeit gegeben hat, ein neues Experiment im neuen Labor aufzubauen. Er hat mich während der ganzen Zeit sehr gut betreut, war immer im Labor, wenn es interessante Messungen gab und hat dabei geholfen, sich auf die wesentlichen Probleme zu konzentrieren und diese zu lösen. Meinem direkten Betreuer Jochen Küpper möchte ich zunächst dafür danken, dass ich an diesem spannendem Projekt arbeiten konnte, er mich dabei engagiert betreut und viele meiner Fragen beantwortet hat. Außerdem hat er mir zahlreiche Dinge im Labor, insbesondere am Lasersystem, beigebracht, maßgeblich die Entwicklung der Software für die Trajektorien-Rechnungen und des Messprogramms KouDA vorangebracht und zudem meine Doktorarbeit ausführlich Korrekturgelesen. Vielen Dank! Frank Filsinger hat zu Anfang seiner Doktorarbeit viel beim Aufbau der Laserstabilisierung und den Stark-Effekt Rechnungen geleistet, und die Zusammenarbeit hat mit ihm wegen seiner ruhigen und positiven Art viel Spaß gemacht. Herzlichen Dank. Auch Fabian Grätz, der im letzte Jahr meiner Doktorarbeit, Diplomand an dem Experiment war, möchte ich für die Zusammenarbeit und die Gesellschaft bei langen Messabenden danken. Henrik Haak hat mit seiner langjährigen Erfahrung den AG-Abbremser konstruiert und beim Zusammenbau des ersten Abbremsers mitgeholfen. Danke dafür und für die vielen kleinen Tricks, die ich mir bei Dir abgucken konnte. Hendrick Bethlem und Sebastiaan van de Meerakker möchte ich für hilfreiche Diskussionen und ihr kontinuierliches Interesse an den Messungen danken.

An dieser Stelle möchte ich mich auch bei der feinmechanischen Werkstatt, und insbesondere bei Adrian Kluge, Peter Teski und Horst Schwäricke für die Fertigung der Komponenten des Abbremsers und vieler kleiner Einzelteile, die ich natürlich immer sofort brauchte, bedanken. Zudem haben sie mir netterweise zeitweise einen eigenen Arbeitsplatz in der Werkstatt eingerichtet, um die

einzelnen Module zusammenzubauen und zu justieren. Beim Zusammenbau und Justieren des zweiten und dritten Moduls haben dann auch André van Roij und Fabian Grätz mitgeholfen, danke dafür. Die elektronischen Werkstätten, und hier insbesondere Georg Heine, Victor Platschkowski und Patrick Schlecht, haben die elektronischen Komponenten gefertigt, und unter anderem die Hochspannungsschalter immer wieder umbebaut, bis mysteriöse Erdschleifen-Probleme verschwunden waren. Auch hierfür vielen Dank. Uwe Hoppe und Heinz Junkes möchte ich für ihren Einsatz bei der Messsoftware KouDA und ihr schnelles Reagieren bei auftretenden Problemen danken. Bei Manfred Erdmann möchte ich mich dafür bedanken, dass er viele kleine mechanische Arbeiten übernommen und zudem jedes Jahr am Frauentag einen Süßigkeitenteller für uns bereit gestellt hat.

Bei Jens-Uwe Grabow möchte ich mich dafür bedanken, dass ich zusammen mit Melanie Schnell und Jochen Küpper in Hannover an seinem Mikrowellenspektrometer die Dipolmoment-Messungen an Benzonitril und Aminophenol durchführen und dabei einen Crashkurs in Mikrowellenspektroskopie machen konnte.

Inga von Dölln möchte ich dafür danken, dass sie sich immer um das Wohl der ganzen Abteilung sorgt und gut auf uns alle aufpasst. Christa Hermanni hat das Englisch in meiner Doktorarbeit mit großer Sorgfalt korrigiert und mir dabei noch so einiges beibringen können. Herzlichen Dank für die viele Arbeit! Cyndi und Sophie, mit denen ich eine zeitlang das “Frauenzimmer” geteilt habe, waren wirklich sehr angenehme, lustige und hilfsbereite Zimmergenossinnen. Auch den anderen Frauen in der Abteilung, insbesondere Adela, Undine, Melanie, Frauke, Bea und früher noch Jacqueline, möchte ich für die gute, freundschaftliche Atmosphäre und die netten Kaffeepausen auf dem Balkon danken; ebenso aber auch allen männlichen Diplomanden, Doktoranden, Postdocs und Kollegen.

Nicht zuletzt möchte ich mich bei meinen Eltern und meiner Familie bedanken. Sie haben mir immer die Freiheit gegeben, meine eigenen Ziele zu verfolgen und mich dabei unterstützt. Meinem Freund Stephan danke ich ebenfalls für die langjährige Unterstützung und das gründliche Korrekturlesen der Arbeit.